Adam Mickiewicz University in Poznań

Faculty of Physics and Astronomy

Formation mechanisms of single-particle-thick microstructures and the physical properties of the structures formed.

A dissertation submitted for the degree of Doctor of Philosophy in Physics

by

Yaroslav Harkavyi

Supervised by

Dr hab. Zbigniew Rozynek

Co-supervised by

Dr Konrad Giżyński

Poznań 2025

"The important thing is not to stop questioning. Curiosity has its own reason for existing."

-Albert Einstein

Dedication

This dissertation was completed in the shadow of war, but it was made possible by the light of Ukrainian courage. It is dedicated to the brave men and women defending the sovereignty and future of my nation.

I dedicate this work to the memory of the fallen, to the resilience of the wounded, and to the unyielding spirit of all who stand against tyranny.

With immense pride and gratitude, I dedicate this especially to my father.
While I pursued knowledge, you fought to protect the world
in which that knowledge matters.
This is for you.

Acknowledgments

I am deeply grateful to my supervisors. **Zbigniew**, **Konrad** - thank you for your kind help, guidance, trust, and the genuinely friendly relationship we built. Your open conversations, honest feedback, and sense of humor made this journey not only productive but also enjoyable.

I also thank all **co-authors** and **collaborators** whose ideas, experiments, and careful reviews strengthened this work at every stage.

To my friends **Bassam**, **Khobaib** and **Filip** - you made this PhD an adventure. Our lunch-break debates and shared trips kept me curious and grounded. And to my loved one, **Victoria** - thank you for your steady support and help throughout, especially during the late experiments and endless rewrites.

Finally, to **my family** - thank you for your love, patience, and belief that this project was worth the effort. Your support carried me through.

This research was funded by the National Science Centre, Poland (NCN) under project no. 2019/33/B/STS/00935, “Efficient fabrication of single-particle-thick micropaths, their characterization, and applicability.” Part of this research was supported, both directly and indirectly, by CADENAS, a simple joint-stock company based in Bydgoszcz, Poland.

Table of Contents

List of papers constituting the dissertation

I. **Fabrication of 1D particle structures outside a liquid environment using electric and capillary interactions: From fundamentals to applications**
Rozynek Z., Harkavyi Y., Giżyński K.
Materials & Design, Volume 223, November 2022, 111233
$IF_{2025} = 7.9$ $Ministerial\ points_{2024} = 140$

II. **Single-particle-thick microstructures fabricated through controlled withdrawal of particles from a dispersion meniscus**
Harkavyi Y., Tiwari G. And Rozynek Z.
Materials & Design, Volume 255, July 2025, 114160
$IF_{2025} = 7.9$ $Ministerial\ points_{2024} = 140$

III. **Experimental and FEM simulation study of compressive deformation of solder microballs and particle chains**
Harkavyi Y., Giżyński K. And Rozynek Z.
Soft Matter, 2025, 21, 4393
$IF_{2025} = 2.8$ $Ministerial\ points_{2024} = 100$

IV. **Fabrication of a new type of electrically conductive micro-tracks via mechanical compression of beaded structures**
Rozynek Z., Harkavyi Y., Martinsen Ø.G., Giżyński K.
Materials & Design, Volume 253, May 2025, 113985
$IF_{2025} = 7.9$ $Ministerial\ points_{2024} = 140$

V. **Formation of conductive beaded structures via Joule heating**
Harkavyi Y. , Solovan M., Rozynek Z.
To be submitted, Fall 2025

Abstract

The formation of microscale structures with the thickness of a single particle remains a significant research challenge. Existing methods for producing such beaded structures have at least one limitation, that is, they tend to be inefficient, costly, or require advanced and highly expensive research infrastructure, including cleanroom facilities. Moreover, these methods, mostly academic in nature, are non-commercialized, not yet industrially adopted, and rarely allow for the fabrication the fabrication of structures that are both precisely positioned and readily applicable on substrates.

This dissertation focuses on investigating the physical mechanisms underlying the formation of beaded microstructures and their subsequent processing into robust, highly conductive microtracks. It bridges fundamental aspects, such as interparticle forces, instabilities, and material response, with experimentally observed behaviors and process outcomes.

The dissertation begins by demonstrating that an electric field, assisted by capillary forces, can initiate the extraction of conductive microparticles from a liquid, leading to the formation of freestanding chains with the thickness of a single particle, assembled outside the bulk liquid. Systematic experiments were conducted to identify the conditions under which this process is most effective and to clarify the roles of two types of capillary bridges that are present in the system: the particle–meniscus bridge, which controls the extraction stage, and the particle–particle bridge, responsible for stabilizing the chain after the field is removed. The obtained results establish a broadly applicable and low-cost approach for producing one-dimensional microscopic structures and confirm their potential use as conductive microtracks.

A more scalable variant of the method was then introduced, based on the controlled withdrawal of particles from a dispersion meniscus formed at the tip of a conduit that simultaneously serves as an electrode. Continuous particle supply to the meniscus enables precise control of the chain length and its positioning between the meniscus and the substrate. Electrostatic modeling using the finite element method was used to quantitatively determine the attractive force between the first particle and the substrate and to explain how the substrate material, thickness, and geometry, as well as ambient humidity, influence the initiation and stability of the process.

To transform the produced chains into functional conductors, this work combined experiments with finite element simulations. The analysis of compressive deformation was first carried out on individual solder microspheres to calibrate the model parameters for more complex cases, and then on entire chains. The obtained measurements and simulation results map the force–displacement relationship, contact growth, and plastic flow at relevant scales. This enabled the formulation of design rules for tuning the contact area between microparticles in beaded structures, which directly affects their electrical properties and the evolution of their shape.

Two complementary post-processing routes were investigated: (i) mechanical compression and (ii) resistive-heating-based microwelding. Both approaches were analyzed experimentally and with finite-element (FEA) simulations—mechanical and coupled electro-thermal. Compression converts beaded chains into continuous, low-resistance micro-tracks on diverse substrates, providing an alternative to nanoparticle-ink sintering. Joule joining, achieved by applying a controlled current signal to the system, drives rapid, localized neck growth at particle contacts. Together, these methods transform fragile beaded structures into durable tracks, achieving near-bulk electrical conductivity.

This dissertation is organized as follows. Chapter 1 reviews the formation, properties, and post-processing of beaded structures and introduces material models for compressive deformation. Chapter 2 details experimental techniques for chain pulling, geometrical characterization, rheology, electrical resistance, and electrical sintering. Chapter 3 presents computer simulations: mechanical compression, electrical resistance, Joule heating, and electrostatic attraction, including geometry, physics setups, meshes, and studies. Chapter 4 summarizes the publications that constitute the basis of this dissertation and discusses their thematic interrelations. Chapter 5 presents the main conclusions drawn from the conducted research. Chapter 6 provides a list of the references used. Chapter 7 includes the full versions of the manuscripts, while Chapter 8 includes co-authors' statements outlining their individual contributions.

Streszczenie

Tworzenie struktur mikroskopowych o grubości pojedynczej cząstki stanowi istotne wyzwanie badawcze. Istniejące metody wytwarzania takich struktur koralikowych mają co najmniej jedno ograniczenie – są mało wydajne, kosztowne lub wymagają zaawansowanej i bardzo drogiej infrastruktury badawczej, w tym pomieszczeń o kontrolowanej czystości powietrza (ang. *cleanroom*). Ponadto, metody te – w większości o charakterze akademickim – są nieskomercjalizowane, nieuprzemysłowione i rzadko pozwalają na uzyskanie struktur, które są jednocześnie precyzyjnie pozycjonowane i łatwe do wykorzystania na podłożach.

Niniejsza rozprawa koncentruje się na badaniu mechanizmów fizycznych leżących u podstaw formowania jednowymiarowych mikrostruktur oraz ich dalszej obróbki prowadzącej do powstania trwałych, wysoce przewodzących mikrościeżek. Praca łączy analizę zjawisk fundamentalnych – takich jak oddziaływania siłowe, niestabilności oraz reakcję materiału – z wynikami obserwacji eksperymentalnych i efektami procesowymi.

Praca rozpoczyna się od wykazania, że pole elektryczne, wspomagane przez siły kapilarne, może inicjować ekstrakcję przewodzących mikrocząstek z cieczy, prowadząc do formowania wolnostojących łańcuchów o grubości pojedynczej cząstki, powstających poza fazą ciekłą. Systematyczne eksperymenty pozwoliły określić warunki, w których proces ten przebiega najefektywniej, oraz ujawniły role dwóch rodzajów mostków kapilarnych obecnych w układzie: mostka cząstka-menisk, który kontroluje etap ekstrakcji, oraz mostka cząstka-cząstka, odpowiedzialnego za stabilizację łańcucha po wyłączeniu pola. Uzyskane wyniki wyznaczają uniwersalne i niskokosztowe podejście do wytwarzania jednowymiarowych struktur mikroskopowych oraz potwierdzają możliwość ich zastosowania jako przewodzących mikrościeżek.

Następnie wprowadzono bardziej skalowalny wariant metody, oparty na kontrolowanym wyciąganiu cząstek z menisku dyspersji utworzonego na końcówce przewodu, pełniącego jednocześnie funkcję elektrody. Ciągłe dostarczanie cząstek do menisku umożliwia precyzyjne sterowanie długością formowanego łańcucha oraz jego pozycją pomiędzy meniskiem a podłożem. Modelowanie elektrostatyczne z wykorzystaniem metody elementów skończonych pozwoliło ilościowo określić siłę przyciągania pomiędzy pierwszą cząstką a podłożem oraz wyjaśniło, w jaki sposób materiał, grubość i geometria podłoża, a także wilgotność otoczenia wpływają na inicjację i stabilność procesu.

Aby przekształcić wytworzone łańcuchy w funkcjonalne przewodniki, niniejsza praca łączy eksperymenty z symulacjami metodą elementów skończonych. Analiza deformacji ściskającej została przeprowadzona najpierw na pojedynczych mikrocząstkach lutowia, w celu kalibracji parametrów modelu dla bardziej złożonych przypadków, a następnie na całych łańcuchach. Uzyskane pomiary i wyniki symulacji odwzorowują zależność siła-przemieszczenie, wzrost powierzchni kontaktu oraz przepływ plastyczny w odpowiednich skalach. Pozwoliło to na

sformułowanie zasad projektowych umożliwiających dostrajanie pola kontaktu między mikrocząstkami w strukturze koralikowej, co bezpośrednio wpływa na jej właściwości elektryczne oraz ewolucję kształtu.

Zbadano dwa komplementarne sposoby obróbki łańcuchów: (i) mechaniczne ściskanie oraz (ii) zgrzewanie ciepłem Joule'a przy dostarczaniu ustalonej kontrolowanej mocy. Oba podejścia przeanalizowano eksperymentalnie i z użyciem komputerowych symulacji (Metoda Elementów Skończonych) zarówno mechanicznych, jak i elektrotermicznych. Ściskanie przekształca koralikowe łańcuchy w ciągłe mikrościeżki o niskiej rezystancji na różnych podłożach, stanowiąc alternatywę dla spiekania tuszy z nanocząstek. Z kolei zgrzewanie Joule'a, uzyskane przez przyłożenie określonej mocy do układu, wywołuje szybki, lokalny wzrost szyjek w miejscach kontaktu. W rezultacie obie metody pozwalają przekształcić nietrwałe łańcuchy o grubości pojedynczej cząstki w trwałe ścieżki o przewodności zbliżonej do materiału litego.

Niniejsza rozprawa jest zorganizowana w następujący sposób. Rozdział 1 przedstawia przegląd metod formowania, właściwości oraz sposobów obróbki końcowej struktur koralikowych, a także wprowadza modele materiałowe niezbędne do opisu deformacji ściskającej. Rozdział 2 szczegółowo opisuje techniki eksperymentalne dotyczące wyciągania łańcuchów, charakteryzacji geometrycznej, reologii, rezystancji elektrycznej i spiekania elektrycznego. Rozdział 3 przedstawia symulacje komputerowe obejmujące kompresję mechaniczną, rezystancję elektryczną, nagrzewanie oporowe (Joule'a) oraz przyciąganie elektrostatyczne, w tym geometrię, modele fizyczne, siatki i analizy. Rozdział 4 podsumowuje publikacje stanowiące podstawę niniejszej rozprawy i omawia ich wzajemne powiązania tematyczne. Rozdział 5 przedstawia główne wnioski wynikające z przeprowadzonych badań. Rozdział 6 zawiera zestawienie wykorzystanej literatury. W rozdziale 7 zaprezentowano pełne wersje manuskryptów, natomiast rozdział 8 obejmuje oświadczenia współautorów dotyczące ich wkładu w poszczególne publikacje.

1. Introduction

The controlled assembly of microparticles into well-defined structures holds great promise for applications across electronics, optics, biosensing, and materials science.[1,2] One particularly exciting direction in this field is the fabrication of single-particle-thick micropaths, *i.e.*, chain-like structures composed of particles arranged with single-particle precision. Such assemblies offer unique physical and functional properties, such as high surface-to-volume ratio, long-range periodicity, and mechanical tunability. Yet, despite their potential, the efficient creation of such structures with sufficient control over their geometry, composition, and position on a substrate remains an open challenge.

Over the past decades, numerous techniques have been developed to assemble microparticles. These approaches range from electrohydrodynamic flows and optical tweezers to capillary-assisted assembly and microrobotics.[3–5] However, most of these methods suffer from significant limitations. They are often expensive, require specialized equipment or cleanroom facilities, are time-consuming, or are restricted to a narrow set of particle types, structures, or substrate geometries. In particular, few methods allow for rapid, scalable, and precise deposition of particles to form flexible and complex micropaths on demand.

This dissertation addresses this technological bottleneck by introducing and studying a new electric field-assisted approach to assemble particles into beaded structures directly on substrates. The method relies on a combination of electric and capillary forces to guide and stabilize particle chains outside bulk liquids, enabling precise deposition with single-particle resolution. It is designed to work with a wide range of particle types (*e.g.*, soft, hard, core-shell), sizes (50 µm - 1 mm), and substrates, including uneven or flexible surfaces. The technique offers the potential to form both linear and non-linear micropaths efficiently, even at high throughput.

The goals of this research are threefold:

1. **To better understand the physical mechanisms** behind electric-field-driven particle deposition, including the roles of field parameters, particle geometry, and fluid-substrate interactions.
2. **To understand the underlying principles** that connect the geometry and arrangement of the resulting microstructures with their mechanical and electrical response, including changes introduced by post-processing treatments**.**
3. **To evaluate the feasibility of applying these structures in near real-world conditions,** such as in microelectronics or composite materials.

The work is positioned at the intersection of soft matter physics, materials science, and applied engineering. It combines experimental efforts with theoretical modeling to address key scientific

questions concerning particle interactions, force distributions within beaded structures, and the tunability of their structural properties.

Beyond its scientific contributions, this project aims to establish the foundation for a novel, scalable manufacturing technique that could enable new design strategies for functional microscale systems. By advancing the ability to manipulate particles individually and to guide them into organized structures, this research aspires to bring bottom-up fabrication closer to practical, accessible deployment — much like the transformative impact of inkjet printing on text and image reproduction, but within the realm of microstructured materials.

1.1. Beaded structures

Beaded structures are defined here as single-particle-thick chains formed by aligning individual particles side by side. Geometrically, they can be described as linear strings of touching spheres — much like a microscopic pearl necklace. This arrangement gives them a periodic structure at the mesoscale (with a repeat period equal to the particle diameter) and a relatively large surface-to-volume ratio. These structural features determine many of the distinctive behaviors and potential applications of beaded chains.

Below, an overview is provided of how such structures can be formed (Section 1.1.1), what post-processing methods can be applied to modify them (Section 1.1.2), and several possible applications that exploit their unique geometry (Section 1.1.3).

1.1.1. Theoretical background behind formation of beaded structures

The assembly of particles into single-particle-thick chains is governed by a delicate balance of electrostatic and capillary interactions. When an alternating electric field is applied between a sharp electrode and a counter electrode immersed in a weakly conductive liquid, particles located near the meniscus of the liquid experience strong electric field gradients that polarize them and give rise to dielectrophoretic forces. These forces can lift individual particles out of the liquid and string them into a chain, provided that they overcome the capillary adhesion binding the particles to the meniscus. Back in 2017, my supervisor and collaborators developed a theoretical framework that explained this phenomenon and provided scaling laws for the conditions required to extract and stabilize particles outside the liquid phase.[6] The present work is fundamentally based on their model.

A simplified description of the extraction process begins with the induced charge on a particle of radius a in a liquid of permittivity ε_l, subject to an applied voltage U. The effective induced charge is approximately

$$Q \approx 4\pi\varepsilon_0\varepsilon_l aU,$$

which produces an electric field decaying with distance as $E(r) \sim aU/r^2$. A neighboring particle, separated by distance d, then experiences an attractive dielectrophoretic force of the form

$$F_e \approx \frac{8\pi\varepsilon_0\varepsilon_l k a^5 U^2}{d^5},$$

where k is the Clausius-Mossotti factor, close to unity for conducting particles. In the limit of near contact $d \to 2a$, this simplifies to

$$F_e \approx \frac{\pi}{4}\varepsilon_0\varepsilon_l k U^2,$$

For the particle to be detached from the meniscus, this electrostatic attraction must exceed the capillary adhesion force acting at the three-phase contact line, which can be written as

$$F_{sp} \approx 2\pi\gamma a,$$

where γ is the surface tension. Balancing these two forces gives a characteristic threshold voltage for extraction,

$$U_{min} \approx \sqrt{\frac{8\gamma a}{\varepsilon_0\varepsilon_l k}},$$

demonstrating that larger particles and higher surface tension liquids demand higher voltages, while more polarizable media reduce the requirement.

Although these far-field estimates are useful, they significantly underpredict the actual forces near contact. Rozynek et al. (2017) showed that when two conducting spheres are separated by only a small gap $s = d - 2a \ll a$, the electric field becomes highly localized in the narrow region between them, leading to a much stronger attraction than predicted by conventional dielectrophoretic theory. The near-contact asymptotic behavior follows

$$F_e \propto \frac{1}{s[\ln(s/a]^2}, \qquad s \ll a,$$

which diverges as the gap decreases. This enhancement explains why experimentally observed thresholds for extraction are typically only a few hundred volts for particles of radius 10-30 µm, rather than the kilovolts suggested by the simple scaling. The singular amplification of the near-contact force is therefore the crucial mechanism enabling efficient chain formation at experimentally accessible conditions.

Once particles are lifted out of the liquid, they remain connected by slender liquid bridges that form spontaneously at each contact point. These bridges generate cohesive capillary forces of magnitude $F_{ss} \approx 2\pi\gamma a$, which hold the chain together even after the external field is removed. The condition for a chain of N particles to remain stable is that this cohesive force must exceed the gravitational load,

$$F_g = \frac{4}{3}\pi\rho g a^3 N,$$

with ρ the particle density. From this relation one obtains an estimate for the maximum stable particle size,

$$a_{\max} = \sqrt{\frac{3\gamma}{2\rho g}}.$$

For micron-sized spheres, gravitational effects are negligible compared to capillary cohesion, which explains why extremely long chains of hundreds of particles can remain self-supported once assembled.

Dynamic effects further determine whether the chain grows straight and stable. At too low AC frequencies, particles touching the electrode undergo charge reversal each half-cycle, leading to contact-charge electrophoresis and destabilization of the structure. Using sufficiently high frequencies, typically in the kilohertz range, prevents this effect and allows continuous growth of the chain. Similarly, the withdrawal speed of the electrode governs the liquid volume carried between adjacent particles. Pulling too fast results in overinflated bridges that later cause curling or kinking, while too slow withdrawal produces fragile, overly thin bridges prone to rupture[7]. In practice, there exists an optimal range of speeds where bridges form with balanced volumes, stabilizing the straight chain.

Altogether, the theory developed in 2017 and extended in the present work shows that the successful formation of beaded structures arises from a well-defined interplay of electrostatic extraction, capillary adhesion at the meniscus, cohesive bridges between neighboring spheres, and dynamic stability determined by field frequency and pulling speed. This framework explains the relatively low voltage thresholds, the remarkable stability of chains once detached from the liquid, and the sensitivity of morphology to experimental parameters. It provides the essential physical basis for the controlled fabrication of single-particle-thick chains, enabling systematic exploration of their properties in the subsequent parts of this dissertation.

1.1.2. Beaded structures post-processing

As-fabricated beaded chains typically consist of particles that are merely touching or held together by weak capillary bridges. In this initial state, the contacts between particles are not robust - often just point contacts or thin residue of dried liquid - and thus the structure's mechanical and electrical integrity is limited. In particular, a "fresh" chain of metal microspheres exhibits relatively poor electrical conductivity because the actual contact area between neighboring spheres is very small. If one desires to use the chain as an electrical conductor or a durable structural element, some form of post-processing is required to strengthen the inter-particle connections.

Several post-processing techniques were explored in this work to effectively fuse the particles together in the chain. These techniques involve applying heat or pressure to the chain to promote sintering, melting, or deformation at the contact points.

One straightforward approach is **thermal sintering**. For example, gentle heating of the chain (by placing it on a hot plate or under an IR lamp) can cause adjacent particles to thermally bond if the particle material has a low melting point or a sinterable surface coating. In our case, solder alloy microspheres are used, which melt at relatively low temperatures (~183 °C for $Sn_{63}Pb_{37}$ solder). By heating a chain of such solder balls (either by external heating or by passing current through them as described below), the formation of metallic "necks" between the spheres can be induced, effectively welding them into a continuous conductor.

Laser welding is another option: a focused laser beam can be scanned along the chain to deliver localized heating at each contact point[8]. This method has the advantage of targeting specific areas and minimizing heat exposure to the substrate.

Yet another technique is **electric current-induced fusing**[9], wherein an electrical current is run through the particle chain itself. The resistive (Joule) heating at the tiny junctions between particles can be intense, causing them to melt and merge. This method essentially turns the chain into its own heating element - when done carefully, the current fusing can happen rapidly and yield uniform connections. All of these heat-based post-processes (hotplate, laser, or current) aim to accomplish the same goal: to increase the neck area between particles so that the chain transitions from a series of point contacts to a nearly continuous wire.

For materials that are malleable (soft solids), **mechanical compression** provides an effective alternative to thermal sintering. In this research, a technique was developed for mechanically pressing the particle chain against the substrate to deform the spheres at their contact interfaces. By using a flat plate to gently squash the chain (in a direction perpendicular to the substrate), each microsphere gets flattened slightly where it touches its neighbors. The result is that those contact points are broadened from a tiny spot to a finite area. When the particles are made of a conductive metal (like solder), this increased contact area is translated into a dramatic reduction in electrical resistance along the chain. In **[Scientific paper III]** It was shown that by controlling the amount of compressive strain, the conductivity of the chain can be tuned in a predictable way. Small compressive deformation (a few percent) already improves particle contacts and lowers resistance, while larger compression (tens of percent) can effectively merge the particles into an almost solid continuous track. Notably, this process can be done at room temperature and is highly localized – heating the entire substrate or structure is not required. In one set of experiments, a 1D chain of ∼300µm solder balls was placed on a circuit board and pressed in incremental steps; the resistance of the chain was dropped from on the order of ohms to the milliohm range as the compression was increased from 0% to ∼50%. The compressed chain essentially behaves like a printed metallic wire.

Mechanical post-processing thus enabled the fabrication of electrically conductive micro-tracks out of the assembled particle chains. This was a key step toward applications in electronics. The lines produced by compression of the chains have a distinctive structure: they retain the periodic, beaded morphology (the spherical outlines of particles are still visible along the track), yet they function as continuous conductors. Because the particles in the chains are relatively large (hundreds of microns) compared to nanoparticles, the resultant conductive lines have a much greater cross-sectional thickness (essentially one particle diameter tall). The height-to-width ratio of these 1D tracks is much larger than that of conventional printed conductive lines made from nanoparticles. This can be advantageous for carrying higher currents or for mechanical robustness, as the created conductive line is less prone to cracking under bending than an ultra-thin film. Additionally, using microparticles instead of nanoparticles sidesteps some issues like oxidation of nanosurfaces or the need for solvent evaporation. The cost is also reduced - microparticles are generally cheaper and easier to handle in bulk.

In summary, post-processing transforms the beaded chains from delicate structures into solid, functional entities. Whether by thermal fusing or mechanical pressing, the goal is to create strong

bonds between the particles so that the chain behaves as a unified material. In this dissertation work, both approaches were explored: mechanical compression was used extensively (given the solder particles' suitability for plastic deformation), and studies on electrically induced neck formation (essentially electro-sintering) were also conducted.

The ability to post-process in different ways provides flexibility depending on the application. For instance, mechanical pressing is very effective for malleable solders, whereas laser or electrical fusing might be preferable for brittle substrates, harder particles or when precise selective bonding is needed. With these tools in hand, beaded particle structures can be reliably produced that are not only geometrically well-defined but also physically robust and highly conductive.

1.1.3. Application of beaded structures

Beaded particle lines represent a novel type of microstructured material, and their unique one-dimensional, periodic architecture offers opportunities in various application domains. Unlike conventional micropaths or printed wires made by continuous films or sintered nanoparticles, studied chains consist of discrete repeating units (spheres) which can impart distinctive functional properties. Here are highlighted a few key application areas where such 1D particle assemblies could be used:

Optical Waveguides and Photonic Devices[10–12]: Chains of dielectric or metal-dielectric microparticles can guide light via coupled resonances in the spheres. This phenomenon allows a microsphere chain to function as an optical waveguide that channels light along its length. Studies have shown that microsphere chains can focus light and even guide it around gentle bends, acting as flexible photonic circuits. Thus, printed particle chains could serve in micro-optical interconnects, lasers, or sensors. For example, a line of spherical resonators can be integrated on a chip to route laser signals, with the periodic structure enabling unique filtering or bandgap effects that continuous waveguides lack.

Conductive Tracks in Electronics: A primary motivation for this work is to create highly conductive micro-tracks for electronic circuits. After appropriate post-processing, a beaded chain of metal particles becomes essentially a solid wire with electrical resistivity approaching that of the bulk metal. Such tracks have several advantages over traditional printed electronics lines. As mentioned, they are thicker (higher cross-section), and because they are made from large, high-purity particles, they can exhibit superior conductivity compared to lines made from sintered nanoparticle inks. They also require no binders or matrices (the particles themselves form the structure), potentially improving thermal and electrical conductance. The ability to "write" a single-particle-width conducting line via studied method and then fuse it means that one can directly fabricate circuit traces on a variety of substrates. This could be useful for repairing broken PCB traces, creating custom antenna geometries, or any application where fine, yet highly conductive lines are needed. Additionally, since microparticles are inexpensive relative to nanomaterials, this approach could be cost-effective for large-area electronics

Flexible Electronics and Soft Robotics: The beaded structure, being composed of articulated units (the spheres), inherently allows some flexibility. Whereas a continuous metal filament might crack under strain, a chain of particles joined at discrete points can accommodate deformation more

easily (the contacts can flex or rotate slightly). This makes particle chains attractive as flexible conductors or strain-tolerant wires in wearable electronics or soft robotic devices. For instance, a conductive chain embedded in an elastomer could stretch and relax with less risk of failure, functioning as a stretchable interconnect or sensor. Moreover, the chains can be designed to be responsive: in a soft robotic context, a chain of magnetizable particles could serve as an artificial cilium or flagellum[13,14]. By applying a magnetic or electric field, the chain can be made to bend or oscillate, mimicking the movement of cilia for propulsion or fluid mixing. This concept of field-driven deformation of particle chains has been demonstrated with colloidal magnetic beads in oscillating fields, showing programmable undulation patterns[15,16]. Similarly, chains of “active” Janus particles have been made to beat like flagella under an AC electric field[17]. These examples point to the use of beaded structures in soft actuators and robotic micro-swimmers, where their one-dimensional flexibility and field-addressability become a strength.

Sensors and Tunable Metamaterials: The discrete periodic nature of a beaded chain means that properties can be tuned by external stimuli, a characteristic that is valued for sensing and metamaterials[18]. A clear example is provided by using the chain as a strain sensor. Because the electrical resistance of the chain is highly sensitive to the quality of contacts between particles, the resistance will be changed by any mechanical strain that slightly separates or presses the particles. This can be harnessed as a piezoresistive sensing mechanism. A gentle touch or vibration could be detected as a change in the conductivity of the chain, allowing it to act as a pressure or vibration sensor. Likewise, the electromagnetic response of a metallic particle chain (for radiofrequency or THz waves) is dependent on its periodicity and spacing. By adjusting the spacing (say, via mechanical stretching/compression or by building the chain with alternating particle sizes), a tunable electromagnetic metamaterial line could be created that filters or guides waves in a frequency-selective manner. Additionally, since each junction in the chain can be made to act like a micro-capacitor or nonlinear element (if an oxide or tunneling gap exists), an array of such junctions could be used for sensing changes in the environment (*e.g.*, humidity can be detected if water infiltrates contacts, or chemicals that alter contact resistance can be detected). Finally, the fact that the chain can be reconfigured (by applying fields or by breaking/reforming sections) means that reconfigurable circuits or switchable interconnects could be designed at the microscale. For example, a segment of chain could be "opened" or "closed" by an electrical pulse that fuses or breaks a contact, allowing it to function as a one-time programmable switch or fuse in an electrical network.

In summary, beaded 1D particle structures open up a palette of possibilities in technology - from guiding light in tiny optical networks, through serving as high-performance conductive lines, to enabling flexible electronics components and responsive micro-actuators. Many of these applications leverage the intrinsic periodic structure of the chains, which differentiates them from conventional continuous materials. While practical deployment will require further engineering (and is beyond the immediate scope of this basic research focus), the potential applications underline the significance of studying these structures.

1.2. Particle chain's properties

After establishing how the particle chains can be fabricated, attention is next turned to examining their physical properties. A central aim of the research was to characterize how these one-dimensional particle assemblies behave, in order to assess their viability for various uses and to uncover interesting physics emergent from the "beaded" architecture.

In this section, three key aspects of the chains' properties are discussed: (i) Electromechanical coupling - how mechanical and electrical behaviors are interrelated in the chains, (ii) Mechanical properties - how the chains deform under forces, particularly compressive loads, and (iii) Electrical properties - how well the chains conduct electricity and how this can be modulated. Each of these aspects was investigated through a combination of experiments and complementary simulations, as summarized below.

1.2.1. Electromechanical properties

An intriguing feature of the particle chains is the strong interplay between their mechanical state and electrical performance - in other words, the structures are electromechanically coupled. This means mechanical manipulations (like straining or bending the chain) can drastically change its electrical characteristics, and conversely, electrical inputs (like current or fields) can induce mechanical changes in the chain. This coupling is encountered prominently in the context of tuning the chain's conductivity via compression. As noted in **[Scientific paper III]** and **[Scientific paper IV]**, the area of contact between metal particles is increased when a chain is pressed. Experimentally, it was found that even a small compressive deformation leads to a noticeable drop in the chain's electrical resistance, and dramatic reductions in resistance are caused by larger deformations. Essentially, the chain behaves like a potentiometer (variable resistor) that can be mechanically tuned: applying compressive strain can decrease its resistance by orders of magnitude.

For example, in one test, a chain consisting of 10 solder microspheres initially had a resistance on the order of a few ohms; after ~50% compression the resistance was observed to fall to the tens of milliohm range. This occurs because mechanical compression transforms the point contacts into broad, low-resistance interfaces (as is discussed in Section 1.1.2). The electromechanical effect here is analogous to a piezoresistive sensor, where electrical resistance is lowered by mechanical pressure, except in this case the magnitude of change is very large due to the drastic increase in contact area. This effect can be exploited for fine control of the chain's conductivity: by calibrating force vs. resistance, a specific resistance value could be targeted by applying a corresponding compressive force. In a practical sense, this could be used to tune circuits (*e.g.*, adjusting the resistance of an interconnect by deforming it) or to sense forces.

The coupling also operates in the opposite direction: mechanical and structural changes in the chain are driven by electrical stimuli. In **[Scientific paper V]**, a current-induced fusing process was documented in which resistive (Joule) heating at interparticle contacts locally melts the solder, leading to the formation of metallic necks and a reduction of free surfaces. As these necks develop, contacts become stronger and less resistive, and the chain stiffens; under controlled DC drive the morphology generally remains beaded with welded joints rather than transforming into

a single solid rod. Sustained high-level DC (or constant-power) operation can extend neck growth and push resistance lower, so the electrical drive is limited in practice to avoid over-fusing. Uniform, global heating was found to promote full coalescence and even electrical discontinuities and was therefore avoided.

Beyond these effects, dynamic electromechanical behavior under alternating fields can also be exhibited by beaded chains. Because the particles are polarizable, oscillatory forces can be exerted on them by an AC electric field. This can drive mechanical motion of the chain or its segments. For instance, it has been shown by researchers that a chain of Janus (two-faced) colloidal particles in an AC electric field will spontaneously oscillate in a wave-like fashion, mimicking the beating of a flagellum [38]. In a similar vein, periodic bending deformations have been made to occur in chains of magnetic particles in a time-varying magnetic field [37]. These demonstrations, while in colloidal systems, illustrate the principle that these 1D assemblies can function as micro-actuators powered and controlled by external fields. In this work, the focus was primarily placed on static or low-frequency electromechanical coupling (such as the DC resistance change with compression), but the same chains could potentially be used in an AC field to produce vibrations or wave propagation along the chain. In fact, using an AC electric field to excite a mechanical resonance in the chain could be envisioned—treating it like a string that can be plucked electrically. Although not yet explored in this thesis, this is an interesting direction for future research: the particle chain as a conduit for mechanical wave propagation (soliton-like compression waves are known in macroscopic bead chains) or as an electrically driven resonator. The important takeaway for now is that the beaded structure inherently couples mechanical and electrical domains: the structure's electrical state is affected by its deformation, and the structure can be deformed by applying electrical forces. This duality is a hallmark of the system's physics and underpins some of the applications mentioned (*e.g.*, sensors and actuators).

1.2.2. Mechanical properties

In **[Scientific paper III]** and **[Scientific paper IV]** the mechanical behavior of the particle chains was extensively studied with an emphasis on how they deform under compressive loads. Understanding the mechanical robustness of the chains is crucial if they are to be handled, integrated into devices, or compressed intentionally for tuning conductivity. To obtain quantitative insight, controlled compression experiments were performed on individual particles and on chains of particles, and finite element method (FEM) simulations were also developed to analyze the stress and strain distributions. The particles used in the study (solder microballs) are made of a soft alloy, which means they undergo plastic deformation (permanent shape change) when sufficient force is applied. This makes them an excellent testbed for exploring how a chain of soft particles yields under load.

Single-particle compression was first examined as a baseline. Using a micromechanical loading apparatus (rheometer), individual solder spheres were compressed between two flat plates, and the force-displacement curves were recorded. This was done for particles of various diameters (ranging 200-760µm) to see how size affects mechanical response. The compression speed (strain rate) and, in some cases, the temperature were also varied, to capture rate-dependent and temperature-dependent plasticity.

These tests provided information on yield force (when the particle first starts to plastically deform), the stress-strain relationship, and the particle's behavior at large deformations (up to 50% compression). As expected, a single solder microball flattens out under compression - essentially, it behaves like a tiny soft metal pillowing out under load. The force-strain curves from single particles showed characteristics consistent with known solder material properties, such as a yield point and strain hardening. Importantly, data were gathered that allowed a material model (discussed in Section 1.3) for the solder's plasticity to be calibrated under the experimental conditions.

Next, **compression tests of the particle chains** were performed, and the results were compared to the single-particle case. For these tests, multiple solder balls were aligned in a row (forming a beaded chain on a substrate), and the entire chain was then pressed down using a flat plate, distributing the load across all particles simultaneously. The mechanical response of the chain turned out to be noticeably different from that of a single particle. In particular, it was found that chains require higher compressive forces to achieve the same strain compared to single spheres. In other words, a chain of N particles is mechanically "stiffer" in compression than N isolated particles compressed individually. The primary reason is the lateral constraint imposed by neighboring particles in the chain. When a particle in the middle of a chain is compressed, it cannot freely expand outward in all directions because its sides are confined by adjacent particles. This constrained geometry leads to a higher resistance to compression. The experiments showed that this effect grows with the number of particles in the chain - longer chains (with more particles) exhibit a more pronounced increase in required force for a given global strain, up to a certain length.

To analyze the mechanical behavior more deeply, **FEM simulations** were utilized, and constitutive models were fitted to the data. A Johnson-Cook plasticity model (a common model for metals that includes terms for strain hardening, strain-rate sensitivity, and thermal softening) was used to describe the solder material's response. By inputting the single-particle compression results (including data at different strain rates and temperatures), Johnson-Cook parameters were extracted that accurately reproduced the stress-strain curves observed. Notably, the model confirmed that within the testing range, temperature had a greater influence on the solder's yield stress than strain rate. With a validated material model in hand, the compression of multi-particle chains was simulated. The FEM allowed internal stress distributions and contact pressures that are difficult to measure experimentally to be visualized. These simulations supported the experimental finding that chain compression requires higher forces - they showed how stress builds up at the constrained contacts. Some simulations were extended beyond the range of the experiments (*e.g.*, to higher strains or more particles) to predict behavior in regimes that could not be directly tested. The agreement between simulation and experiment was good, lending confidence that the understanding of the mechanics is sound.

From a practical perspective, these mechanical insights are valued for anyone attempting to use or process the particle chains. For instance, if a chain is wanted to be compressed to a certain strain to achieve a target conductivity, the data can indicate how much force is required, and how that might be changed if the chain has, say, 5 particles versus 50 particles. Knowing the force

needed also informs the design of equipment for large-scale fabrication. It ensures the applied pressures stay within safe limits to avoid crushing particles excessively or damaging the substrate.

In summary, the mechanical characterization revealed that beaded chains of solder particles behave as strain-hardened, confined media. They are harder to compress than single particles due to neighbor interactions, and their yield behavior can be modeled well with standard metallurgical models. Quantitative measures (force-displacement curves, material parameters) are now possessed that describe their deformation. These results are not only fundamentally interesting (showing how adding periodic constraints alters the mechanics of a soft material), but also directly inform how the chains are to be processed (*e.g.*, how to press them to get good electrical contacts without overshooting).

1.2.3. Electrical properties

One of the most interesting and promising application fields of the studied structure is the possibility of its usage in electronics. Therefore, the electrical properties of the particle chains are central to the functionality that is afforded to them as conductive paths or electronic components.

When assembled, a chain of conductive microparticles is essentially a series of tiny junctions between particles, which can be thought of as resistive or even tunneling contacts. If the particles are being touched with minimal contact area, the overall resistance of the chain is relatively high, as a significant resistance is contributed by each contact, or the contact even behaves like an insulating gap if the particles are not firmly in contact.

Indeed, in **[Scientific paper I]** and **[Scientific paper IV]** poor conductivity was initially shown by as-fabricated chains. in many cases, the chain was observed to behave almost like an open circuit until a small force was applied to press the particles together, indicating very small initial contact points. This is expected because when two spherical metal particles touch, contact is typically made at only a microscopic spot (a point or a very small patch), and a large electrical resistance (as well as a large thermal contact resistance) is thereby produced. Furthermore, electron flow at these junctions can be further impeded by any slight oxide layer or contamination.

After post-processing, however, the situation is changed dramatically. When the chains were fused or compressed as described in Section 1.1.2, the electrical conductance was increased by orders of magnitude. In the best cases, when the neighboring particles in the chain became fully connected, the chain's resistivity was observed to drop to essentially that of the bulk metal making up the particles. For instance, a chain of Sn-Pb solder spheres that has been properly compressed or melted at the contacts will conduct electricity almost as well as a solid Sn-Pb alloy wire of the same dimensions. Extremely low resistance values (milliohm range) were measured for compressed chains, approaching the theoretical minimum based on the bulk resistivity of solder and the cross-sectional area of one sphere. This is a remarkable result - it means that single-particle-thick wires are made feasible, with performance on par with conventional metal traces. The initial low conductivity is no longer a limitation once the chain is treated to form good contacts.

To give a concrete example, before compression, a 10 mm long chain of 300 µm solder balls might register a resistance too high to be measured with a standard multimeter (effectively $>10^6$ Ω, due to insulating gaps or oxide). After gently pressing the chain to ~3% strain, the resistance is typically seen to drop into the kilohm or hundred-ohm range (indicating that stable conduction path formation has been achieved, but contacts are still small). By ~6% strain, resistance in the few-ohms range was often observed, and by ~22% it would be well below 1 Ω. At ~50% compressive strain, as noted earlier, the resistance can reach $\sim 10^{-2}$ Ω or even lower. This progression shows how contact area growth and particle deformation lead to improved electrical coupling.

It is also noted that the conduction of the chain becomes more stable (less sensitive to small perturbations) after such processing. Initially, a slight vibration could break the weak contacts and spike the resistance, whereas a fused or compressed chain has fixed connections that are robust to vibrations.

The current-voltage behavior of the chains was characterized and was found to be ohmic after fusing - meaning a linear I-V curve, as is expected for a metal conductor. Before fusing, some chains showed non-linear I-V, possibly due to tunneling or oxide barriers at contacts. Once fused, the chains could carry substantial currents. In one test, over 1 A of current was carried by a compressed chain without failure, which is impressive for a microscale conductor. This is attributable to the relatively large cross-section of a 300 µm diameter chain compared to, say, thin printed silver lines. It was found that if too high a current is pushed through an insufficiently fused chain, it will self-heat and fuse itself (the current-induced welding mentioned in **[Scientific paper V]**). This usually lowers the resistance further, essentially self-improving the conductivity up to a point, but if excessive, it can also cause sections of the chain to overheat and melt apart. Therefore, careful control of current is needed in applications, but at the same time, the self-fusing effect could be used deliberately as a way to create conductive connections by simply zapping a chain with current.

Another aspect of electrical properties is the AC or high-frequency behavior. While AC impedance was not explicitly studied in detail, it is expected that an unfused chain might exhibit capacitive characteristics between particles (since tiny gaps or oxide layers can act as capacitors). Additionally, the periodical structure of studied chains could lead to unexpected behaviours in a high-frequency range. This could be relevant if the chains are being used for high-frequency signal transmission or antenna structures. A fully fused chain, on the other hand, would behave like a continuous conductor up to high frequencies (limited mainly by the inductance of a line of spheres, which could be an interesting frequency-dependent effect in its own right).

1.3. Material models for compressive deformation of solder microspheres and particle chains

Stress-strain relations are fundamental in materials science and mechanics, as they quantify how solids carry load and how deformation proceeds under that load. This section introduces the constitutive descriptions used to simulate the compression of individual solder microspheres and particle chains, and then connects them to the finite-element models employed later in the

thesis. *For clarity,* ***stress*** *is the internal force per unit area:* $\sigma = F/A$. ***Strain*** *is the relative change in length:* $\varepsilon = \Delta L/L_0$.

In materials science and mechanics, material model links stress and strain (and, when needed, strain rate and temperature). A practical hierarchy of increasing model complexity was adopted and is summarized here from the simplest to the most expressive level relevant to this work.

Linear elastic material. This is the simplest model, in which stress is proportional to strain through Hooke's law with Young's modulus (E) and Poisson's ratio (ν). I this case - deformation is fully recoverable upon unloading. For soft solder this elastic regime spans only a fraction of a percent strain, yet it remains essential because all plasticity models embed an elastic sub-law that governs unloading and small perturbations.[19]

Elastic–perfectly plastic material. This model adds the simplest extension beyond linear elasticity by introducing an initial yield stress (σ_{ys0}). Below σ_{ys0} the response is elastic; once yielding begins the stress remains constant at this level, so the current yield (flow) stress is simply

$$\sigma_{ys} = \sigma_{ys0}.$$

This simple idealisation provides only a lower-bound envelope for force-displacement curves in compression, and it does not capture the gradual strengthening that is typically observed in experiments as the contact areas between the surfaces enlarge.[20,21]

Linear isotropic hardening. After yielding, the flow stress is assumed to rise linearly with the amount of plastic strain, according to

$$\sigma_{ys} = \sigma_{ys0} + E_{iso} \cdot \varepsilon_{pe}.$$

Here, E_{iso} is the isotropic hardening modulus, and ε_{pe} the equivalent plastic strain. This bilinear model is straightforward to calibrate from a single reference test and often provides a better match than perfect plasticity over a certain strain range. At higher compressions, however, the real material response shows a smoother, curved increase in force due to geometry changes and evolving contacts, which this simple linear assumption cannot capture.[20,21]

Ludwik (nonlinear isotropic hardening). A more flexible baseline is obtained with

$$\sigma_{ys} = \sigma_{ys0} + K \cdot {\varepsilon_{pe}}^{n},$$

where K is the strength coefficient and n is a hardening exponent. Identification at a fixed temperature and strain rate allows the simulated force-strain curve to reproduce the observed curvature over a broad range of compressive strains.[22,23]

Johnson–Cook (rate and temperature sensitivity). To account for rate and temperature effects, the Ludwik-type backbone is extended multiplicatively by a logarithmic rate term and a thermal-softening term, typically written as

$$\sigma_{ys} = \left(\sigma_{ys0} + K \cdot {\varepsilon_{pe}}^{n}\right)\left[1 + C \cdot \ln\left(\frac{\dot{\varepsilon}_{pe}}{\dot{\varepsilon}_{pe,\mathrm{ref}}}\right)\right][1 - (T^*)^m],$$

where C is the rate sensitivity coefficient, m is the thermal-softening exponent, $\dot{\varepsilon}_{pe}$ is the equivalent plastic strain rate, $\dot{\varepsilon}_{pe,\mathrm{ref}}$ is reference rate, and $T^{*} = (T - T_{\mathrm{ref}})/(T_{\mathrm{melt}} - T_{\mathrm{ref}})$ describes the homologous temperature. When the thermal factor is retained ($m > 0$), the pronounced softening of solder material at elevated temperatures is captured; for strictly isothermal comparisons the temperature factor may be set to unity. Within the present scope this level of complexity is sufficient to translate a reference calibration across the ranges of platen speed and temperature used in the experiments.[24,25]

It should be noted that more elaborated frameworks exist, but they are beyond the scope of this work. Kinematic hardening models (*e.g.*, the Armstrong-Frederick model[26] and extensions by Chaboche[27]) capture Bauschinger effects in load reversals. Viscoplastic and creep laws (such as Perzyna's overstress model[28] and Norton's power-law creep[29]) describe time-dependent inelastic flow. The Anand model[30] is a unified viscoplastic formulation widely used for solder alloys under long dwell times or thermal cycling. Crystal plasticity theories[31] incorporate crystallographic slip to add microstructural fidelity, and ductile-damage models (*e.g.*, the Gurson porous metal plasticity model[32] with later Tvergaard–Needleman modifications[33]) account for void nucleation and growth leading to failure.

2. Experimental techniques

This section outlines the experimental methods employed throughout this research. A combination of physical characterization techniques, computer simulations and custom-built experimental setups were used to investigate the properties and behavior of the studied systems. Each method was chosen to address specific aspects of the research. The techniques presented below include both standard laboratory tools and specialized instruments designed or adapted for this work. More detailed description of experimental setups is presented in **[Scientific paper I]** - **[Scientific paper V]**

2.1. Experimental setup for chain pulling

The starting point of this work was the approach first described in 2017 by dr. hab. Zbigniew Rozynek and colleagues in Nature[6]. In that paper, was demonstrated a simple yet groundbreaking method to assemble and extract flexible conductive particle chains from a liquid using electric fields and capillary forces. These chains could then be deposited onto surfaces as functional electronic patterns. The method required no special particle treatment or continuous energy input, while also showing promise for scalable manufacturing of basic electronic circuits.

The theoretical background of this phenomenon has already been discussed in the introduction. Here, the focus is placed on the practical aspect: it was found that there are two distinct methods of chain pulling. Both approaches are described in detail in the next sections.

2.1.1. Pulling particle chain out of bulk liquid (needle-immersion)

First, the easier and most straightforward method of chain pulling method from which all started back in 2017[6]. The experiments were performed using a custom-built setup designed to assemble one-dimensional particle structures outside a liquid environment. The system consisted of a signal generator connected to a high-voltage bipolar amplifier, which supplied an alternating electric field to a vertically mounted needle-shaped metallic electrode held in an electrically nonconductive mount. The electrode was attached to a motorized translation stage capable of precise vertical motion at controlled speeds in the range of 0.2 to 1 mm/s. The sample was placed on an XYZ translation stage to allow fine positioning relative to the electrode. The experiments were monitored in real time using a digital microscope.

The particle suspensions were prepared by dispersing electrically conductive microparticles such as Ag-coated hollow silica spheres, stainless steel grains, or solder alloy particles in nonpolar, weakly conductive liquids including silicone oil, castor oil, UV-curable epoxy, or liquid soldering flux. The viscosity of the dispersing media ranged from 50 to 2500 cSt, with surface tensions of ~20-30 mN/m. Depending on the ratio of particle density to liquid density, the particles either floated at the air–liquid interface or sedimented to the bottom of the container. In each case, a small amount of suspension was placed as a thin layer on a substrate or in a small glass vessel.

The sequence of chain assembly is illustrated in Figure 1. First, the electrode was lowered toward the liquid until it contacted the interface (Figure 1a). Next, an AC voltage of 0.5 kV at 1 kHz was applied, polarizing the particles and attracting them to the electrode tip by dielectrophoretic forces (Figure 1b). Once the meniscus-supported particle bridge was formed, the electrode was lifted at a constant speed (100 µm/s in this case), drawing particles into a single-file chain extending above the liquid surface (Figures 1c–d). The role of the liquid meniscus in bridging and stabilizing the chain has been extensively discussed[7].

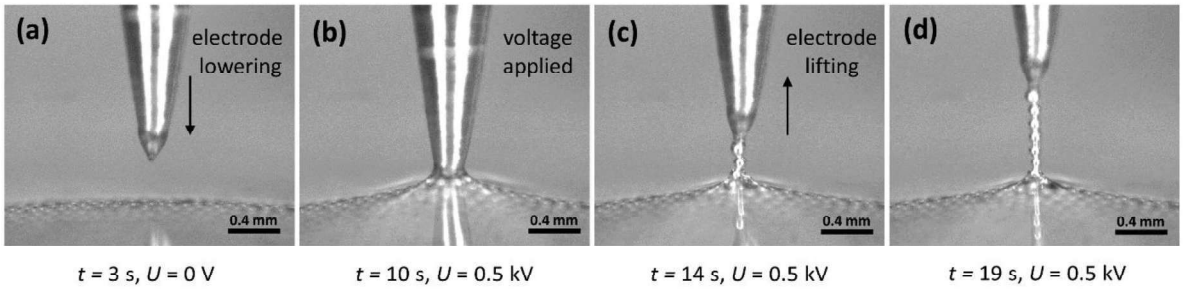

Figure 1. Sequence of electric-field-assisted chain pulling. (a) The needle-shaped electrode is lowered toward the liquid interface. (b) Upon applying an AC voltage (0.5 kV, 1 kHz), particles polarize and accumulate at the electrode tip. (c) Lifting the electrode initiates the formation of a particle chain supported by the liquid meniscus. (d) A stable single-particle-thick chain extends above the liquid surface.

Under optimal conditions, chains composed of hundreds of particles were assembled within seconds and remained intact outside the liquid environment after the electric field was switched off. For microparticles with radii of 20-100 µm, gravitational effects were negligible, and chains several centimeters long could be reliably produced. Pulling speeds that were too high, however, could destabilize the structure before the capillary connections fully formed.

To investigate the electrical properties of the assembled structures and prepare them for subsequent post-processing, the particle chains were transferred onto various substrates immediately after their formation. Once a chain of the desired length was pulled from the liquid, the electrode holding it was lowered until the chain made gentle contact with the target surface. Depending on the intended application, the substrates included glass slides, polymer films, and metallic foils. With the chain tip/end anchored on the surface, the XYZ translation stage holding the substrate was moved in a controlled manner, allowing the deposition of the chain in predefined geometries such as straight lines, arcs, or more complex patterns. This approach enabled precise positioning of the conductive paths and pattern customization without disturbing the structural integrity of the chain.

2.1.2. Pulling particle chain from meniscus (inverted system)

The inverted meniscus system for particle chain fabrication was developed as a more practical and scalable alternative to the previously described needle-immersion method. In this configuration, the particle chain is pulled directly from a dispersion meniscus formed at the outlet of a conductive conduit, which also serves as the active electrode - refer to Figure 2. The conduit is supplied with a controlled flow of particle dispersion using a precision syringe pump, ensuring

a steady and reproducible meniscus shape. This design allows a continuous feed of microparticles to the forming region, eliminating the need for repeated immersion cycles and enabling extended, uninterrupted chain production.

The experimental arrangement consisted of a microfluidic polymer tube, 1 mm in diameter, delivering the particle suspension into the dispersion conduit. The conduit was fixed in an electrically insulating holder and mounted on a motorized stage, providing accurate vertical translation. The substrate was positioned beneath the conduit on an XY translation stage, enabling fine alignment and movement in the plane perpendicular to the pulling direction. A high-voltage bipolar amplifier, driven by a signal generator, supplied an alternating voltage to the conduit, with root mean square values typically in the hundreds of volts, and a square waveform in the kilohertz range. In the most common configuration, the conduit acted as the live electrode while the substrate was grounded, though the polarity could be reversed for specific tests.

To initiate the process, the conduit was lowered toward the substrate until the emerging meniscus became visible in the field of view of the monitoring microscopes (Figure 2(a)). The dispersion flow (0.01 µL/s in this case) was adjusted to form a stable, symmetric meniscus at the outlet, containing a sufficient concentration of suspended microparticles (Figure 2(b)). Once this geometry was established, the syringe pump was stopped, and a short high-voltage AC pulse (1.25 kV at 1 kHz) was applied, bridging the gap between the meniscus and the substrate through a chain of particles (Figure 2(c)). Then the lower AC voltage was applied (0.5 kV here), and the conduit was lifted using a motorized stage at a controlled speed (100 µm/s in this case), drawing particles from the meniscus to form a single-particle-thick chain extending toward the substrate (Figure 2(d)).

It should be noted that the optimal parameters - voltage, pulling speed, and flow rate - vary depending on multiple factors, including particle size and conductivity, ambient humidity and temperature, liquid properties (viscosity and conductivity), capillary geometry and distance from the substrate, as well as the type, shape, and condition of the substrate and meniscus. These dependencies were analyzed in detail in **[Scientific paper I]** and **[Scientific paper II]**.

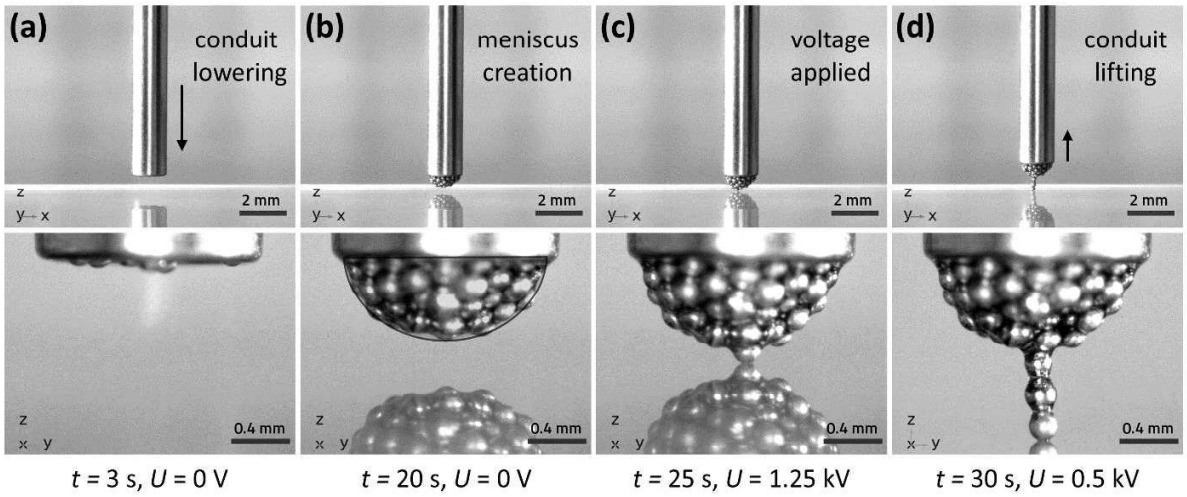

Figure 2. Step-by-step procedure used to initiate the particle chain assembly from meniscus. (a) The capillary conduit is first brought close to the substrate surface. (b) A small meniscus containing suspended microparticles (here stainless steel 200 µm) is produced at the outlet by dispensing the dispersion at a controlled rate (0.01 µL/s). Its contour takes the form of a truncated semicircle, as highlighted by the overlay. (c) A short high-voltage pulse (1.25 kV in this case) is applied, establishing contact between the meniscus and the substrate and extracting a single particle to start the deposition. (d) Afterward, the voltage is reduced to the working value (0.5 kV) and the conduit is lifted, initiating the growth of a linear particle chain.

The system was also tested in an inverted orientation, with the substrate positioned above the conduit, allowing the chain to grow upward against gravity. This configuration enabled the study of gravitational effects on chain stability, as well as the exploration of deposition on non-horizontal or curved surfaces. The method proved versatile, allowing chains to be formed between the meniscus and a wide variety of substrates, including glass, polymers, and metals. By translating the substrate in the XY plane during the pulling process, it was possible to "write" conductive paths in predefined patterns, opening opportunities for direct fabrication of functional microstructures without the need for subsequent transfer steps.

Compared to the earlier immersion-based approach, the meniscus-driven method offered superior repeatability and throughput. The continuous supply of particles ensured consistent chain formation, while the precise control over meniscus geometry and electrical parameters allowed fine tuning of chain properties. This configuration also reduced material waste and made it possible to produce extended, complex patterns with minimal interruption, demonstrating a clear advantage for both laboratory studies and potential industrial scaling.

2.2. Experimental shape change estimation

From the outset, it was clear that final properties of studied structure (electrical resistance, adhesion, and effective stiffness) will depend on its shape. Compression of particles, growth of contact areas, and chain alignment all redirect how current and load travel through the path. Measuring how shape evolves under compression therefore became a core task. The following sections outline several experimental approaches to quantify shape change across relevant scales.

2.2.1. Mechanical Compression of Macroscale Plasticine Spheres

To investigate the basic deformation mechanisms, a macroscopic analogue of the particle chain was constructed using plasticine spheres (Figure 3). In the real system, the particles have diameters up to 760 µm, which makes direct observation and manipulation impractical. Scaling up the system was therefore necessary. Large solder spheres were not a viable option, as they are difficult to obtain and would require proportionally higher compression forces.

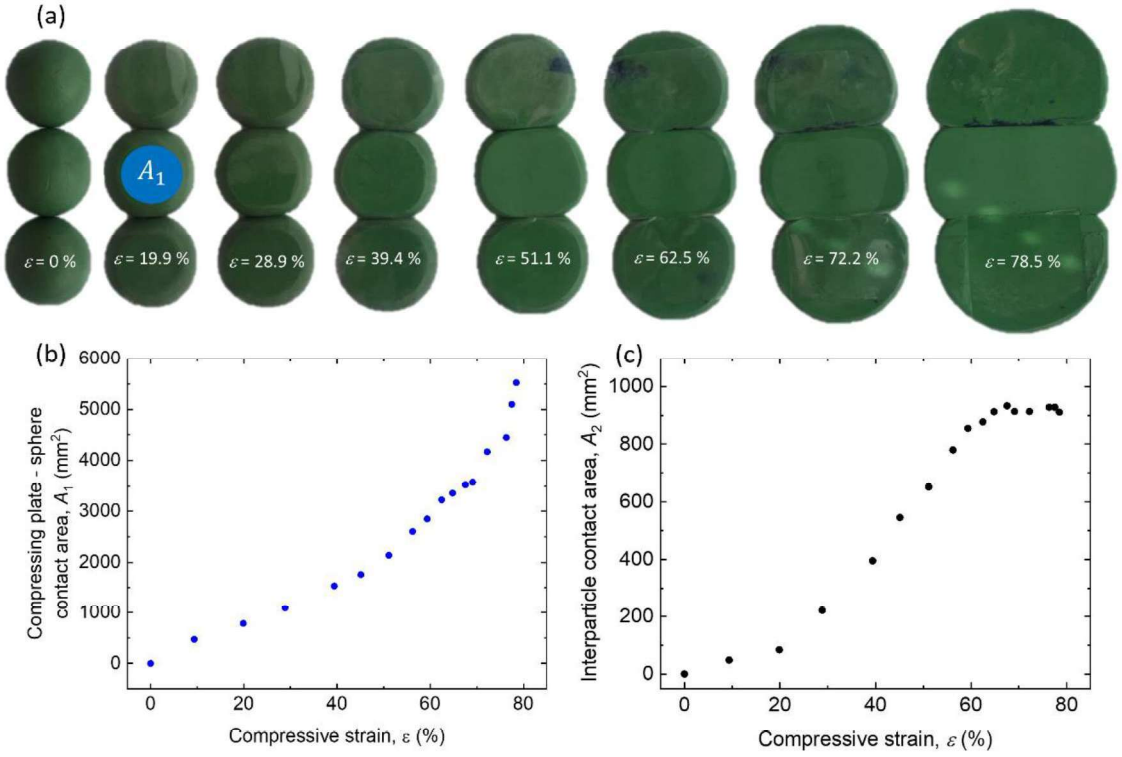

Figure 3. Compression of plasticine spheres used as a macroscopic model system. (a) Top-view of sequential images showing the evolution of deformation and contact formation at different compressive strains, ε. (b) Contact area between the compression plate and the middle sphere (also denoted on fig 1(a) as a blue circle), A_1, as a function of compressive strain. (c) Interparticle contact area, A_2, as a function of compressive strain.

Plasticine was selected as a substitute material because its plastic deformation closely resembles that of solder, while being easier to process. The scaled model allowed us to reproduce compression experiments with comparable mechanical behavior, but under conditions where manipulation, observation, and quantitative measurement were straightforward.

In the experiment, three identical plasticine spheres (diameter 51.2 mm) were placed side by side to mimic alignment of beads within a microparticle chain. Compression was applied through a transparent glass plate by body weight. The evolution of the system under increasing strain is shown in Figure 3(a). The contact area between the glass plate and the middle sphere (A_1) was quantified from digital images using pixel-based analysis, and its dependence on compressive strain is plotted in Figure 3(b). Measuring the interparticle contact area (A_2) required a different

approach: after each compression step, the central sphere was separated and its flattened surface was used to make an imprint on paper. These imprints were scanned and analyzed to extract A_2, which is reported as a function of strain in Figure 3(c). To avoid merging of the spheres or adhesion to the plate, a thin plastic foil was placed at each interface.

2.2.2. Compression of a single restricted solder sphere

As a continuation of the study, an additional experiment was designed to enable real-time observation of interparticle contact evolution during compression. The concept was to confine a single solder sphere between transparent boundaries that would serve as substitutes for neighboring particles.

For this purpose, two polished metallic plates, each 600 µm thick, were fixed to independent translational stages, allowing precise control of the gap between them. The plates were aligned in parallel with an initial separation of 600 µm, into which a solder particle of the same diameter was placed. To enable direct visualization, the entire assembly was enclosed from both sides with thick transparent glass slabs. This arrangement was intended to allow simultaneous observation of the contact area by digital microscope and measurement of the overall compression through the relative displacement of the metallic plates. A schematic of the setup and representative images obtained during the attempt are shown in Figure 4.

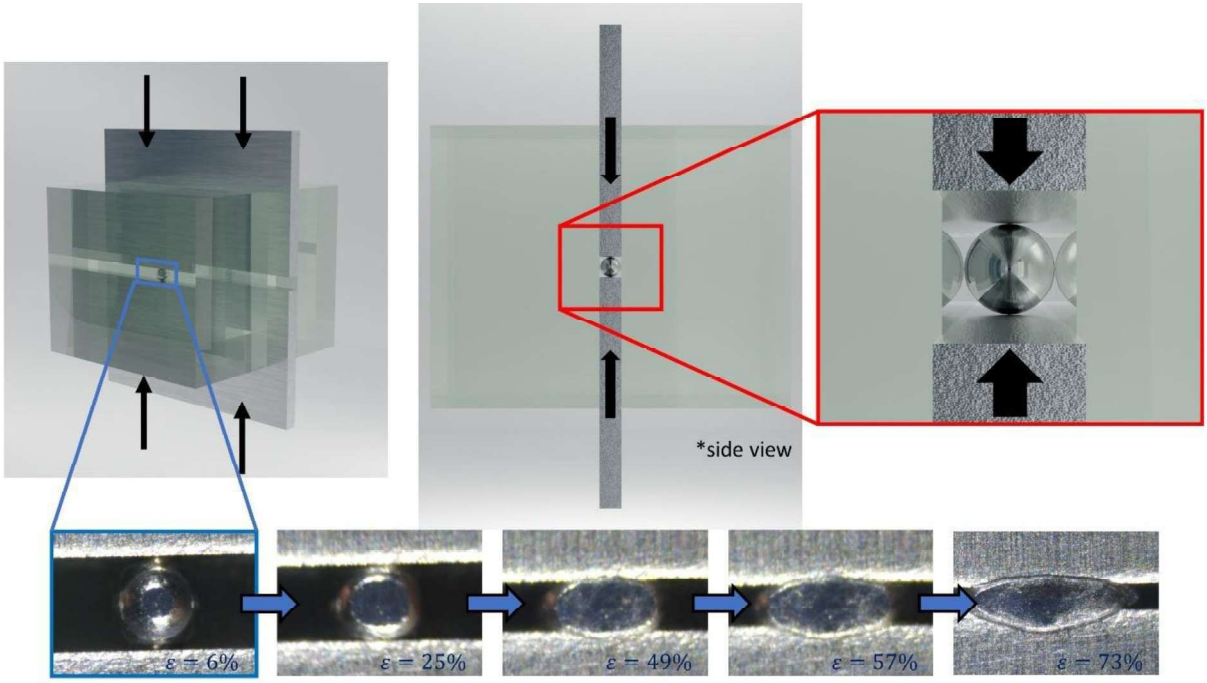

Figure 4. Compression of a single solder sphere restricted between two parallel glass plates. The schematic illustrations (top) show the experimental configuration in perspective and side views, with the black arrows indicating the direction of applied compressive force. The inset highlights the confined particle between the plates. Optical images (bottom) present the evolution of sphere deformation at increasing compressive strains, $\varepsilon \approx 6\%, 25\%, 49\%, 57\%,$ and 73%.

Despite careful preparation, this approach was ultimately unsuccessful. Two main issues prevented reliable measurements:

(i) **Insufficient sealing between glass and metal surfaces.** Even when pressed firmly together, microscopic gaps remained at the interfaces. During compression, solder material leaked into these gaps (as could be seen from the bottom right images at Figure 4), leading to uncontrolled deformation and making the observed contact areas impossible to interpret.

(ii) **Mechanical failure under load.** When the system was pressed more tightly to minimize leakage, the glass slabs began to crack and the metallic plates deformed due to the high frictional forces present.

These limitations demonstrated that, at such small scales, even sub-micrometer misalignments and interface imperfections play a critical role. Consequently, this approach was abandoned in favor of alternative methods.

2.2.3. Compression of solder particle chain

The two preliminary approaches described above (section 2.2.1 and 2.2.2) provided useful insights but were limited by scaling issues, interface imperfections, and experimental constraints. To address these shortcomings, a more direct method was developed: *compression of actual solder particle chains*, followed by microscopic analysis of individual particles. This approach was inspired by the scaled-up plasticine experiments but implemented at the microscale using the same solder particles employed in the main study.

The principle was straightforward: a chain of solder microspheres was compressed, then selected particles were detached and examined under a microscope to determine their shape changes and contact areas. In practice, however, the method required significant experimental effort. Once detached, particles could not be returned to their exact positions in the chain, making it necessary to prepare a new chain for each degree of compression. Reliable statistics also demanded that each compression level be repeated several times. Additional complications arose from the facts that (i) the solder spheres were not perfectly monodisperse and (ii) the difficulty of ensuring perfect chain alignment which increased the variability of the data. Even small misalignments during deposition or compression could have a strong influence on the results.

The experimental setup is shown schematically in Figure 5(a). A glass slab, 5 mm thick, was mounted on two parallel translational stages and positioned above the sample. A digital camera was mounted above the system to observe and record the deformation of the particle chain throughout the compression process.

Chains consisting of approximately ten solder spheres (maximum available diameter 760 µm) were deposited on a glass substrate using the method described in Section 2.1.2. The chain was then compressed to a defined deformation level, typically in increments of ~5%. After each compression, the loading slab was removed, and three to four particles from the central region of the chain were carefully detached. This was done with minimal force to avoid introducing additional deformation that could affect subsequent measurements. The detached particles were imaged under a microscope at consistent magnification, with photographs taken from multiple

perspectives (Figure 5c). These images were analyzed to determine interparticle contact areas (A_2), the contact areas between the particles and the compression slab (A_1), and the overall degree of deformation (ε). Each particle contributed multiple measurements, which were averaged, and the procedure was repeated in triplicate for every compression level to improve statistical reliability. The degree of compression was then incrementally increased, and the process repeated until the full deformation range was covered. The results obtained from this method are presented in Figure 5(b). Those results were later used to validate computer simulations discribed in chapter 3.1.

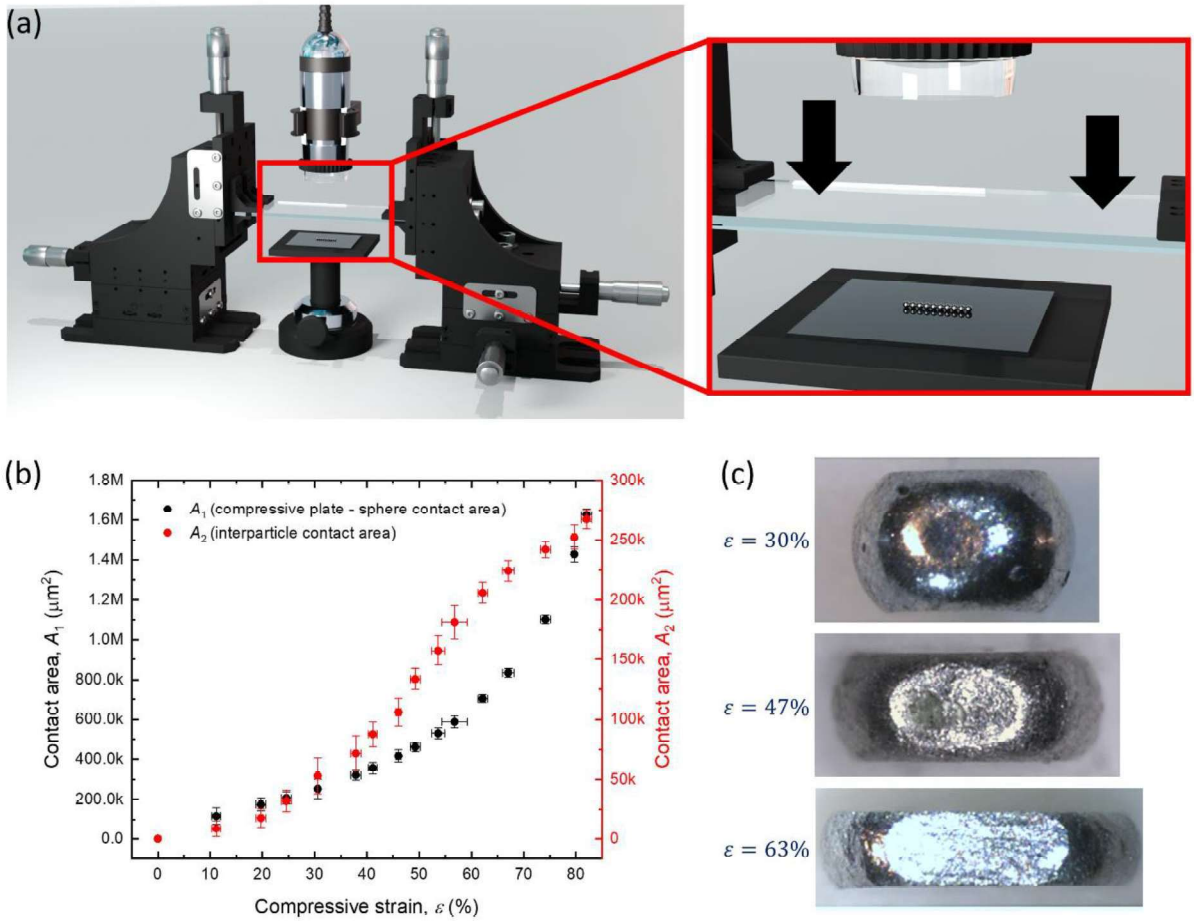

Figure 5. Compression of solder particle chains. (a) Rendered image of the experimental setup showing the glass slab mounted on a motorized translational stage above the particle chain, with a camera positioned for real-time observation of deformation. (b) Summary of the data obtained from the compression experiments, showing interparticle contact areas and contact areas between the particles and the compression slab at different degrees of compression. (c) Representative microscope images of interparticle contact for a detached particle at various compression levels.

2.3. Rheological measurements

In compression studies and potential future applications, it is essential to determine the magnitude of compression force required for reliable particle deformation. As discussed in Section 1.2.3, the applied force depends on several parameters, including the number of particles in the chain, their relative positions, compression speed, material properties of the particles, and

the temperature of the system. Understanding these dependencies is critical for both experimental design and theoretical modeling.

The need for quantitative force measurements became evident during the preliminary experiments. Initial attempts at rapid, near-instantaneous compression frequently resulted in damage to the substrates or fracture of the compression slab, highlighting the necessity of defining appropriate force limits for the system. Furthermore, to support experimental findings with theoretical simulations, accurate material parameters were required. Solder exhibits viscoplastic behavior, which complicates the determination of its constitutive constants. Reliable rheological data are therefore necessary for calibrating the material models used in subsequent simulations.

Beyond these motivations, rheological characterization also enables comparison of different experimental conditions. For example, it allows evaluation of the influence of temperature on compressive strength, which is particularly relevant for solder materials near their melting point. It also provides insight into the repeatability of deformation processes, which is necessary when establishing protocols for reproducible particle chain assembly. Finally, knowledge of rheological behavior is valuable for scaling: it offers a framework for predicting how results obtained on small particle chains may translate to larger assemblies or alternative materials.

The rheological properties of the solder spheres were measured using an Anton Paar MCR302e rheometer configured in a plate-plate geometry, as illustrated (using computer graphics) in Figure 6. This instrument allows precise control and measurement of normal force, compressive strain, and compression velocity. The system is capable of applying a maximum normal force (F_N) of 50 N with a maximum compression velocity of 1 mm s^{-1}. For consistency, individual solder spheres were always placed at the center of the measuring shaft.

When testing linear chains of particles, a minimal quantity of ethanol was applied to the sample to promote alignment and physical contact between neighboring spheres. The ethanol induced attractive capillary forces through the formation of liquid bridges between adjacent particles. Once the solvent had fully evaporated, the compression tests were initiated.

Temperature control during the experiments was achieved using a Peltier device with active heating capabilities, which allowed precise adjustment of the temperature in the range from -25 °C to 220 °C. To minimize heat loss from the measuring shaft, thermal foam insulation was applied (see Figure 6). Prior to each experiment, the position along the compression axis was calibrated by lowering the shaft until it contacted the heated base plate, establishing the zero position. The normal force was then zeroed by monitoring any increase in force during the heating phase, which occurred due to the thermal expansion of the metal shaft. Once the normal force stabilized, both the “zero gap” between the measuring shaft and the base and the normal force itself were reset to ensure accurate measurements. Subsequently, the shaft was raised, and the solder microparticles were swiftly placed on the lower base of the rheometer. The shaft was then lowered to a height corresponding to the particle diameter, after which a waiting period of

approximately one minute was allowed to ensure thermal equilibration of the particles and their surroundings before initiating the measurement program.

All data from these experiments are presented and broadly discussed in **[Scientific paper III].**

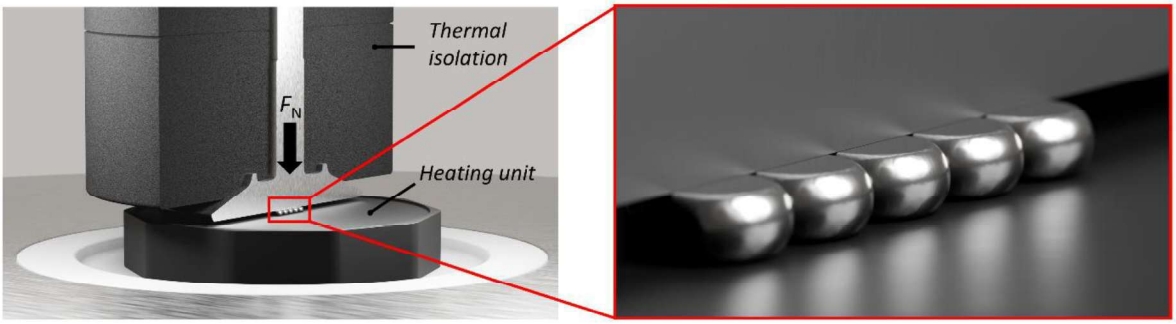

Figure 6. Schematic of the rheometer setup used for particle compression experiments. Left: plate-plate geometry of the Anton Paar MCR302e rheometer equipped with a heating unit and thermal isolation. The thermal insulation and compressing shaft are presented in cross-section to enhance the clarity and comprehensibility of the setup. A normal force F_N is applied through the upper plate while temperature is controlled by the integrated heating system. Right: magnified view of a chain of solder spheres positioned on the heated base plate, aligned for compression testing.

2.4. Surface characterization

In studies of the electrical conductivity of particle chains (described later in section 1.2.3), one of the major factors influencing resistance is the surface roughness of the solder spheres. This effect is particularly relevant at low compression levels, when the first interparticle contacts are established and the real electrical contact area is still limited. In numerical simulations, surface roughness can be included as a fixed parameter, expressed through average roughness or root-mean-square roughness. To obtain representative values for studied system, surface roughness was characterized using two complementary approaches:

(i) **scanning electron microscopy (SEM)** was employed to provide an initial estimate. Figure 7(a) shows an SEM image of a 760-µm solder sphere taken from a selected viewpoint. The inset displays the full particle, with the magnified region marked. From these images, characteristic roughness was identified and measured.

(ii) **mechanical profilometry** was carried out to obtain quantitative surface roughness values. A Bruker DektakXT profilometer, mounted on a pneumatic vibration-isolation table was used for these measurements. Four solder spheres (Sn63Pb37, 760 µm in diameter) were examined, and three independent line scans were performed on each particle. To avoid repeatedly scanning the same surface feature, the stylus was displaced by several tens of micrometers between successive measurements. The measurement conditions were kept constant: a stylus force of 3 mg, a scan length of 400 µm, a scan time of 120 s, and a stylus tip diameter of 2.5 µm. In Figure 7(b), two representative scans are presented for illustration, while all collected data were included in the roughness analysis.

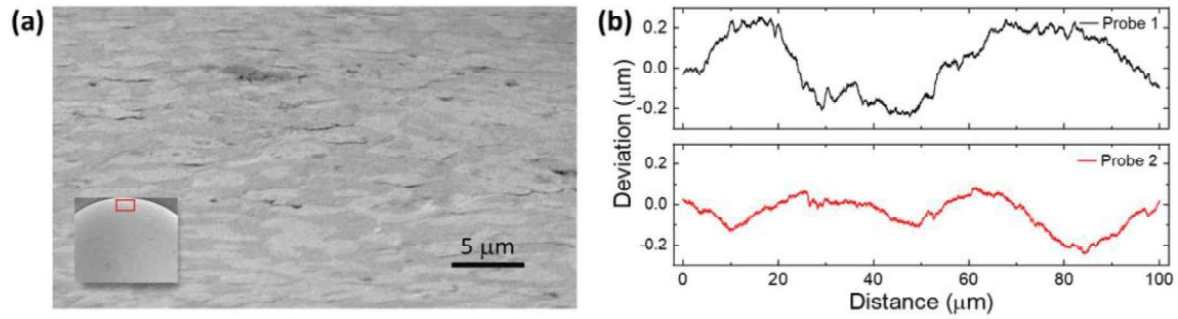

Figure 7. Figure S10. (a) SEM image of a 760-um solder microball captured from a specific perspective. The inset presents a wider view of the microball, with a highlighted area indicating the section that is magnified in the main SEM image. (b) Profilometry results from the experiment conducted with a 2.5 um diameter stylus under a force of 3 mg.

Combining the SEM observations and profilometry measurements, the average surface roughness was found to be approximately 200 nm, with peak height variations on the order of 0.5 µm. These values were subsequently used as input parameters for the simulations described in section 3.2 and in [**Scientific paper IV**].

During SEM imaging of Sn63Pb37 microspheres at higher magnifications, unusual surface patterns with variations in shading were observed – also visible on Figure 7(a). To clarify this effect, energy-dispersive X-ray spectroscopy (EDS) was performed. The analysis revealed that the surface consists of domains corresponding to different phases of the Sn–Pb eutectic alloy. Specifically, tin- and lead-rich regions formed distinct colonies within the microball surface. In addition, scattered gray patches were detected, which are likely residues of oil from the production process. These contaminants suggest that the microspheres are not perfectly clean and may contribute to variations in contact resistance, potentially influencing the overall conductivity of the assembled particle chains.

2.5. Experimental setup for resistance measurements

As discussed in section 1.2.3, the resistance of the studied structure decreases with increasing compression due to the enlargement of the interparticle contact area. In earlier chapters it has been shown experimentally how studied particle chains change their shapes under compression. These investigations were important in predicting the conductivity of the final structure. In this section, the experimental approach used to measure the resistance of the chains as a function of compression is described.

Because the structures are composed of relatively high conductive solder particles at a very small scale, their resistance is extremely low and cannot be reliably captured with simple instruments such as a multimeter. Even the resistance of the wires leading to the measuring device becomes comparable to the values of interest, significantly distorting the results. To overcome this limitation, the four-point probe method was employed, a well-established technique for measuring low resistances.

Inspired by the precision of commercially available universal probe systems, which use kinematic guidance to minimize lateral play and ensure consistent needle positioning, a custom four-probe

system was designed and constructed for resistance measurements of compressed chains. Several factors limited accuracy, such as the quality of materials available, the mechanical stability of the setup, and the time constraints under which the system was developed. Despite these challenges, the setup enabled approximate resistance measurements. However, three main limitations remained:

(i) each time the chain was compressed and a resistance measurement taken, the compression slab had to be raised. Since the chains were not permanently attached to the substrate, even micro movements during this procedure could cause particles to shift, altering the resistance.

(ii) the measurement procedure was time-consuming, requiring repeated cycles of compression, slab elevation, probes positioning, resistance measurement, probes removal, and further compression. A continuous in-situ measurement during compression would have been far more efficient.

(iii) the periodic structure of the chain was suspected to exhibit interesting behavior at higher frequencies, such as changes in impedance, capacitance, or inductance, but current four-probe setup was not capable of such measurements.

For these reasons, a more advanced approach using an impedance analyzer was adopted. This instrument not only allowed precise resistance measurements but also resolved the three key issues encountered. Measurements could be performed in-situ without disturbing the particle chain, the process was significantly faster, and the device enabled high-frequency analysis of the structures (those high frequency measurements are still to be done in the future).

The electrical response of the particle chains under compression was characterized using a precision impedance analyzer (Zurich Instruments, MFIA, 5 MHz) coupled with the manufacturer's impedance test fixture (MFITF). To minimize parasitic contributions from wiring and contact leads, a low-capacitance, low-loss two-terminal (2T) PCB carrier specifically designed for surface-mounted device testing was employed. The carrier consisted of two copper pads (1.5 × 1.5 mm, ~30 µm thick) separated by a gap of approximately 1.4 mm (Figure 8), across which the particle chain was deposited. This configuration allowed for stable, low-noise measurements, particularly at impedance values approaching the instrument's sensitivity limit (~0.1 mΩ). Prior to experiments, the system was calibrated using both open- and short-circuit tests.

Compression of the particle chains was performed in situ using a 5 mm thick glass slab mounted on a translational stage (Figure 8). The same compression setup used in this study has been previously used and described in section 2.2.3. The stage enabled precise control of position while simultaneously permitting optical monitoring of chain deformation through a camera mounted above the system.

Electrical measurements were carried out at a frequency of 100 Hz with an applied voltage amplitude of 0.3 V. These parameters were deliberately chosen to minimize current-induced local welding at particle contacts while suppressing capacitive and dielectric contributions that could affect higher-frequency measurements. In this configuration, the real part of the impedance corresponds directly to the effective resistance of the particle chain.

By this method, electrical resistance was conveniently monitored in the time domain through computer acquisition. However, correlating these measurements with the actual degree of compression (ε) presented a significant challenge. The motorized stage provided sufficient precision only up to approximately $40-50\%$ compression, beyond which the applied force became large enough to induce slight deformation of the entire setup. In particular, bending of the compression slab resulted in a lower effective compression degree than that indicated by the motorized stage position. In addition, as discussed in Section 8, the material under study exhibited creep behavior, meaning that even after the lowering of the slab was halted, the structure continued to deform for a certain period of time.

To address these limitations, the compression degree was instead determined from the top-view live camera feed. The contact area between the compression slab and individual spheres, denoted as A_1, was clearly visible and served as a reliable parameter for estimating compression. With experimental data validated against simulations reported in **[Scientific paper III]**, the measured contact area A_1 was used to extrapolate the precise compression degree (ε).

Figure 8. Experimental setup for electrical characterization of compressed particle chains. The impedance was measured using a precision impedance analyzer (Zurich Instruments, MFIA, 5 MHz) connected to the manufacturer's impedance test fixture (MFITF). A custom-designed two-terminal PCB carrier with low capacitance and minimal parasitic losses was used to hold the sample. The carrier consisted of two copper pads (1.5 × 1.5 mm, ~30 µm thick) separated by a ~1.4 mm gap, across which the particle chain was deposited (right). Compression was applied in situ using a 5 mm thick glass slab mounted on a translation stage (left), which allowed for precise displacement control and simultaneous optical monitoring of chain deformation by the camera positioned above the compression slab.

2.6. Experimental setup for electrical sintering

As discussed in the previous sections, mechanical compression is a reliable post-processing technique aimed at improving conductivity in particle chain structures. However, this approach presents significant challenges. It often requires substrates capable of withstanding extreme conditions, including high pressure and elevated temperatures. Moreover, to ensure uniform compression across the structure, the sample surface must be exceptionally flat and free of irregularities. In practical electronic applications, such ideal conditions are rarely achievable. Real devices typically include components such as resistors, capacitors, and integrated circuits distributed across the substrate. Applying localized mechanical pressure with the required precision would demand complex and expensive actuation systems, which introduces additional limitations in terms of scalability, reliability, and cost.

Due to these constraints, mechanical compression is not always considered a viable or efficient post-processing method. Also, from the simulation results presented in section 3.2, it is known that most heat is generated at interparticle contacts due to the small cross-section. Inspired by this, an alternative technique - **electrical sintering** - was considered to avoid the need for external pressure or high-temperature environments.

The core idea is based on the principle that if neighboring particles within a deposited path have even minimal initial electrical contact, it becomes possible to apply a controlled electrical current through the structure. Because electrical resistance is highest at the inter-particle junctions, these regions become localized hot spots under current flow due to Joule heating. The resulting temperature rise can induce localized melting, forming permanent, conductive joints between particles.

To investigate the underlying physics and validate this concept experimentally, a simplified model system - a two-particle junction - has been studied. This simplified approach allows for controlled experimentation and detailed analysis of the electrical and thermal behavior during sintering at the microscale.

2.6.1. Sample preparation

At this scale, factors that are typically negligible in macroscale systems become critical and can drastically affect the results. To accurately study the behavior of the interparticle contact, all other electrical connections in the system must be as ideal and consistent as possible. This includes the way power is delivered to the test system, which requires reliable electrical contact between the solder particles and the power supply leads. Establishing such contact, however, is not straightforward. Moreover, to obtain statistically meaningful results, the process must also be repeatable.

Initial attempts included soldering the wires directly to the particles, but this proved impractical due to the small scale. High-conductivity silver paste, which is often used for such applications, was also tested. However, to achieve a low-resistance bond with silver paste, the system must typically be heated to 700 °C, a temperature exceeding the melting point of solder particles. Additionally, any increase in temperature accelerates oxide formation on the solder surface, which significantly increases the initial contact resistance.

To overcome these challenges, a simple and repeatable method has been developed to create reliable electrical contacts by mechanically embedding fine drill bits into the solder spheres.

The main challenge again lay in the scale. The largest solder particles used were only 760 µm in diameter, while the drill bit diameter was 100 µm. Manual drilling was not feasible with the required accuracy and reproducibility. To solve this, used a desktop 3D printer Snapmaker 2.0 equipped with a CNC toolhead. This setup provided the necessary accuracy, saved preparation time, and ensured repeatability across multiple samples. The process is illustrated in Figure 9.

Commercially available micro drill bits with an effective cutting diameter of 100 µm was used. Individual solder spheres were placed on a vertically fixed support tube with a diameter smaller than the particles (600 µm), serving as a particle holder. The drill bit was installed into the milling

head and moved to its initial (home) position directly above the sphere (Figure 9a-b). The spindle was then activated at a speed of 3000 rpm, and the drill bit was lowered at a constant rate of 30 mm/min until it reached the midpoint of the sphere ΔL (Figure 9c). The milling head was then retracted, and the bit was carefully detached from the milling head (Figure 9d). This procedure was repeated identically for each sample.

Importantly, the feed rate and rotational speed were carefully chosen to **match the pitch of the drill bit flutes**, effectively allowing the bit to be screwed into the sphere rather than drilled. This approach avoids the removal of material as sawdust, thereby maximizing the mechanical and electrical contact area between the drill bit and the particle. In essence, the bit is embedded into the solder sphere like a threaded insert, rather than cutting through it, which greatly improves both the stability and conductivity of the contact.

All drilling operations were fully automated and executed using G-code commands controlled directly from a computer. This approach significantly simplified the process and ensured high repeatability, as each sample underwent the same predefined sequence of movements and parameters. By minimizing manual intervention, variability was reduced, and it was guaranteed that every prepared particle was treated in a consistent manner. The complete program used in the setup is provided in **Appendix A: G-code for Sample Preparation**.

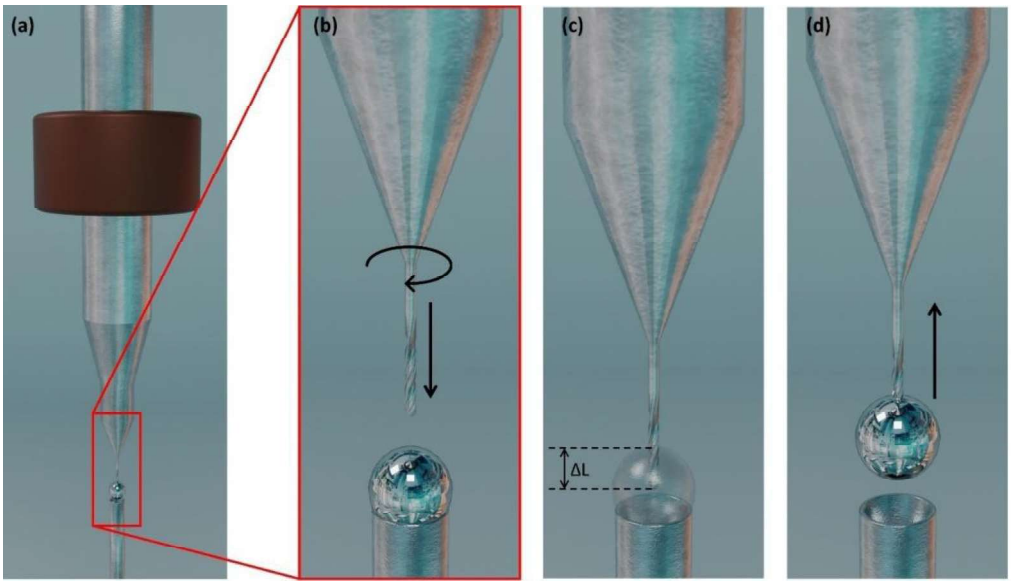

Figure 9. Step-by-step procedure for preparing electrical contacts in solder spheres using a modified 3D printer with a CNC milling head: (a,b) positioning of the drill bit above the solder sphere held on a support tube; (c) embedding the drill bit halfway into the sphere (ΔL) under controlled spindle speed and feed rate; (d) retraction of the milling head and detachment of the drill bit.

2.6.2. Experimental setup for two-particle sintering

Each experiment required a pair of prepared samples, which are described in the previous section. The aim was to establish a similar initial electrical contact for every trial to ensure consistency in results. One of the primary challenges was applying the same mechanical force between the two solder spheres. To achieve this in a simple and reproducible way, a setup was designed in which the gravitational force itself provided the applied load.

The system was inspired by the principle of a pendulum. A single-arm pendulum was constructed. It was mounted on a low-friction bearing at its pivot point to allow nearly free rotation and minimize mechanical resistance. The pendulum arm consisted of a 15 cm long fully threaded M4 rod, with a metal alligator clip attached at its free end. This clip enabled quick mounting and detachment of the solder-particle samples, while also maintaining reliable electrical contact. A second alligator clip was mounted on a three-axis translation stage, positioned so that when both clips held a drill bit with solder sphere, the two spheres faced one another directly (see Figure 10). By adjusting the translation stage, the position of the fixed clip could be aligned so that the pendulum arm, when displaced by a controlled angle, pressed the two spheres into contact.

The applied force was controlled by tilting the pendulum arm to a specific deflection angle. When the arm was displaced by ~5°, the horizontal component of the gravitational force acting on the pendulum ensured a consistent contact force between the two spheres across all experiments. This method provided a simple yet effective way to standardize mechanical loading without requiring complex actuators.

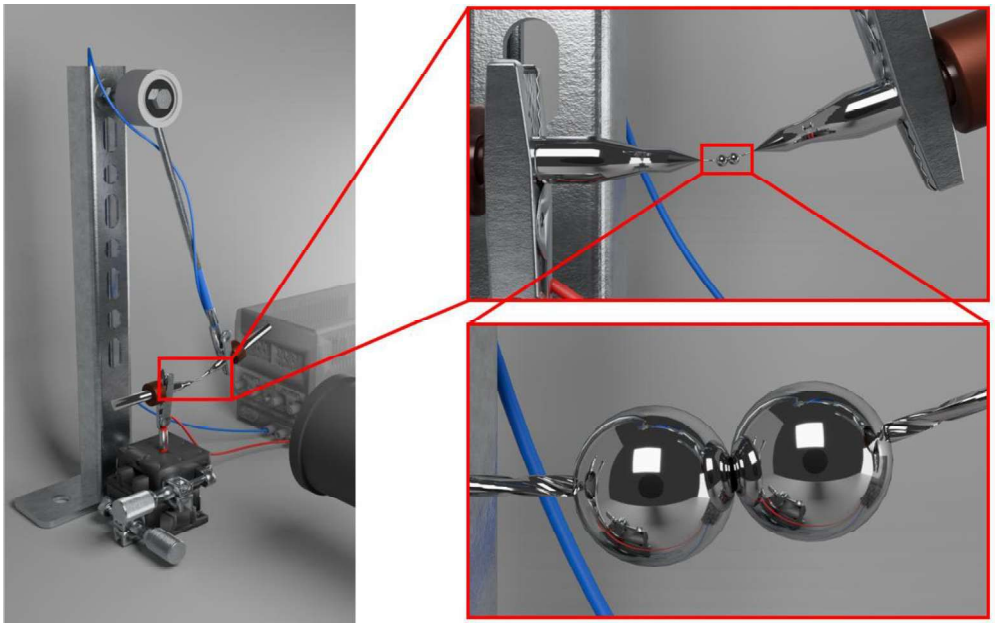

Figure 10. Pendulum-based sintering setup for solder particle contact experiments. A single-arm pendulum was constructed from a 15 cm long threaded M4 rod, mounted on a low-friction bearing to allow nearly free rotation. An alligator clip attached at the free end of the pendulum enabled fast mounting of solder-particle samples while ensuring electrical connection. A second clip, fixed to a three-axis translation stage, held the opposing particle. This arrangement allowed precise alignment so that, upon controlled displacement of the pendulum arm, two solder spheres were brought into contact (right, magnified views).

Electrical power (voltage or current, depending on the experiment) was supplied through the alligator clips to the solder spheres. During testing, an ultrafast camera (Chronos 2.1-HD, Kron Technologies Inc., Canada) was used to capture the temporal evolution of the interparticle contact region. As discussed in sections 1.2.1 and 1.2.3, when current flows through the system, localized Joule heating occurs at the interparticle junction, leading to melting of the solder material and formation of a permanent bond. The high-speed imaging enabled us to directly

observe how quickly these microstructural changes developed under controlled electrical and mechanical conditions.

3. Computer simulations

Computer simulations have become an essential tool in modern research because many physical processes are too complex to capture with analytical formulas or too small-scale to be fully resolved by experiments. They allow researchers to reproduce real systems under controlled, repeatable conditions, test the influence of individual parameters in isolation, and access quantities that cannot be measured directly. In materials science, and especially in studies of contact mechanics and transport phenomena, simulations provide a way to connect macroscopic observations, such as force-strain curves or electrical resistance with the microscopic mechanisms that control them.

In this work, simulations were introduced for exactly these reasons. The experimental studies of microparticle compression and conduction revealed clear trends but left unresolved questions about local contact growth, pressure distribution, and heat generation at interparticle junctions. Direct observation of these effects is impractical: the length scales are microscopic, the fields evolve rapidly during loading, and many parameters (*e.g.*, oxide layer rupture or sub-contact stress) cannot be probed without disturbing the system. Numerical modeling provides a route to overcome these challenges by combining realistic constitutive laws, nonlinear geometry, and multiphysics coupling within a consistent framework.

All simulations were carried out in **COMSOL Multiphysics 6.1** using a combination of specialized modules. The Structural Mechanics Module and Nonlinear Structural Materials Module captured plastic deformation, frictional constraints, and large-strain contact mechanics. The AC/DC Module was used to model current constriction through interparticle contacts and the electrostatic forces responsible for particle-substrate attraction. The Heat Transfer Module was coupled with electrical currents to quantify Joule heating and thermal feedback. For cases involving melting and geometry changes, the Microfluidics Module provided a way to represent partially molten domains with moving meshes. Together, these modules enabled simulations that span mechanics, transport, and thermal effects in a unified way.

The modeling followed a progressive strategy. It started from the simplest case - a single particle compressed between two rigid plates - allowing calibration against experimental force–strain data. From there, it was extended to multi-particle systems, electrical resistance under compression, Joule heating and melting at contacts, and electrostatic attraction near substrates. Each stage added complexity while remaining directly linked to the experiments.

The remainder of this chapter describes these steps in detail: the construction of geometries and symmetry reductions, the applied physics and boundary conditions, meshing and solver settings, and the outcomes of compression, resistance, heating, and electrostatics simulations. Together, they show how computer simulations complement experiments by revealing hidden fields, testing physical models, and establishing the microscopic mechanisms behind the behavior of particle-based conductive structures.

3.1. Mechanical compression

The path to estimating the resistance of a compressed beaded structure begins with the parameter that most intuitively “sets the scale” of conduction between neighbors: the inter-particle contact area. At first glance, one might expect this area to be obtained from simple analysis of deformed geometry - for example, by assuming volume constancy during compression, symmetry about the loading axis, and a smooth, monotonic growth of the contact patch. With ideal conditions - perfect plastic flow, frictionless interfaces, fixed temperature - a direct analytical relation between strain and contact size would be expected. In practice, none of these shortcuts hold robustly for solder microparticles under the loading conditions of interest. Due to geometric (large deflection), material (beyond elastic limit) and contact (frictional) nonlinearity it prevents a reliable, general closed-form estimator for contact area.

(i) First, while plastic flow of metals is approximately isochoric, volume constancy alone is not predictive of local shape change: the deformation is strongly heterogeneous, with barreling near the plates and comparatively mild strains in the equator.

(ii) Second, the contact problem is path-dependent once elastoplasticity, kinematic constraints, and evolving contact conditions are present; the instantaneous contact area depends not only on the current strain but also on how that strain was reached (loading rate, hold periods, partial unloads).

(iii) Third, interface friction modifies the velocity field and increases the effective constraint beneath the plates, rendering frictionless indentation formulas inapplicable.

(iv) Fourth, material behavior is rate- and temperature-sensitive: the effective flow stress of the solder changes with strain rate and with temperature, and so the pressure distribution that supports the contact patch is governed by the imposed loading conditions, including strain rate, temperature, and dwell periods.

(v) Finally, surface and microstructural realities (native oxide films, asperity-scale roughness, phase morphology, and grain size) shift the onset of yield and the way plasticity localizes under the plates.

The implications reach beyond geometry. From classical electrical contact theory, the resistance of a necked contact is governed not only by its geometric cross-section but also by the pressure-dependent constriction of current lines, real vs. apparent area (asperity-supported contact), and the state of the interface (oxide rupture, cleanliness, intermetallic growth). Under operating conditions, Joule heating can further modify local temperature, altering flow stress and, thereby, the mechanical contact itself. Consequently, the final structural resistance depends on (at least) the evolving contact area, the contact pressure and its distribution, the surface state (roughness, oxide thickness, contamination), and the loading pathway (rate, holds, partial unloads). Structure-level features matter as well: shape and periodicity set the number and arrangement of necks; polydispersity, misalignment, and defects modulate load sharing; and creep/relaxation at low rates can change contact geometry even at fixed global strain. These considerations mean that a purely analytical route would require a cascade of simplifying assumptions that are not acceptable in this case.

Since a general analytical relation for the contact area could not be established, the next step was to investigate the problem numerically using Finite Element Analysis (FEA) simulations. First, the simplest non-trivial unit: a single spherical particle compressed between rigid plates was simulated - refer to Figure 11(a). The single-particle model includes the main physical features relevant to chains: curved surfaces, contact growth, frictional constraint, and plastic strain gradients. At the same time, it is simple enough to allow calibration and verification. It mirrors the single-sphere rheological measurements (Section 2.3), allowing direct fitting of force-strain curves over controlled sweeps of diameter, strain rates, and temperature. Starting from this calibrated unit problem, fields that are inaccessible experimentally (local von Mises stress, plastic strain-rate, contact pressure) can be resolved. Plasticity models can also be tested systematically (perfect plasticity, Ludwik hardening, Johnson–Cook with rate/temperature sensitivity), and how friction and thermal conditions steer contact growth and, ultimately, electrical resistance can be quantified.

In the next sections, every aspect of the performed FEA will be described.

3.1.1. Geometry

To reduce computational time, symmetries in the system were identified and used to minimize the size of the simulation domain. Two main geometries were studied.

Single-sphere compression: For the simplest case of one sphere compressed between two rigid plates, the system can be reduced to a 2D axisymmetric model. Only one quarter of the cross section of the sphere is simulated (see Figure 11(a)). The compression plate moves downwards at a constant prescribed speed, $v/2$, while the opposite symmetry plane is placed at the mid-plane of the sphere, parallel to the compression plate. Because of the applied symmetry, the actual loading velocity must be divided by two, since the system represents compression from both sides.

Infinite chain of spheres: For this configuration, 3D models were used since a simple 2D axisymmetric reduction is no longer possible. Symmetry was still applied by simulating only one-eighth of a sphere. Instead of modeling a neighboring sphere, a rigid plane perpendicular to the compression plate is placed at the contact, acting as the mirror boundary. This configuration is illustrated in Figure 11(b). As in the single-sphere case, the applied plate velocity is divided by two to account for symmetric compression.

Other symmetric reductions: Depending on the type of simulations to be performed in later chapters - such as *polydispersity*, *misalignment*, or compression of a *finite number of spheres* (*e.g.* two, three, four, or five) - further symmetry can be exploited to reduce simulation cost. Examples of such reduced simulation units are presented in Figure 11(c-e). These reductions allow more

efficient exploration of parameter space while keeping the essential deformation mechanisms intact.

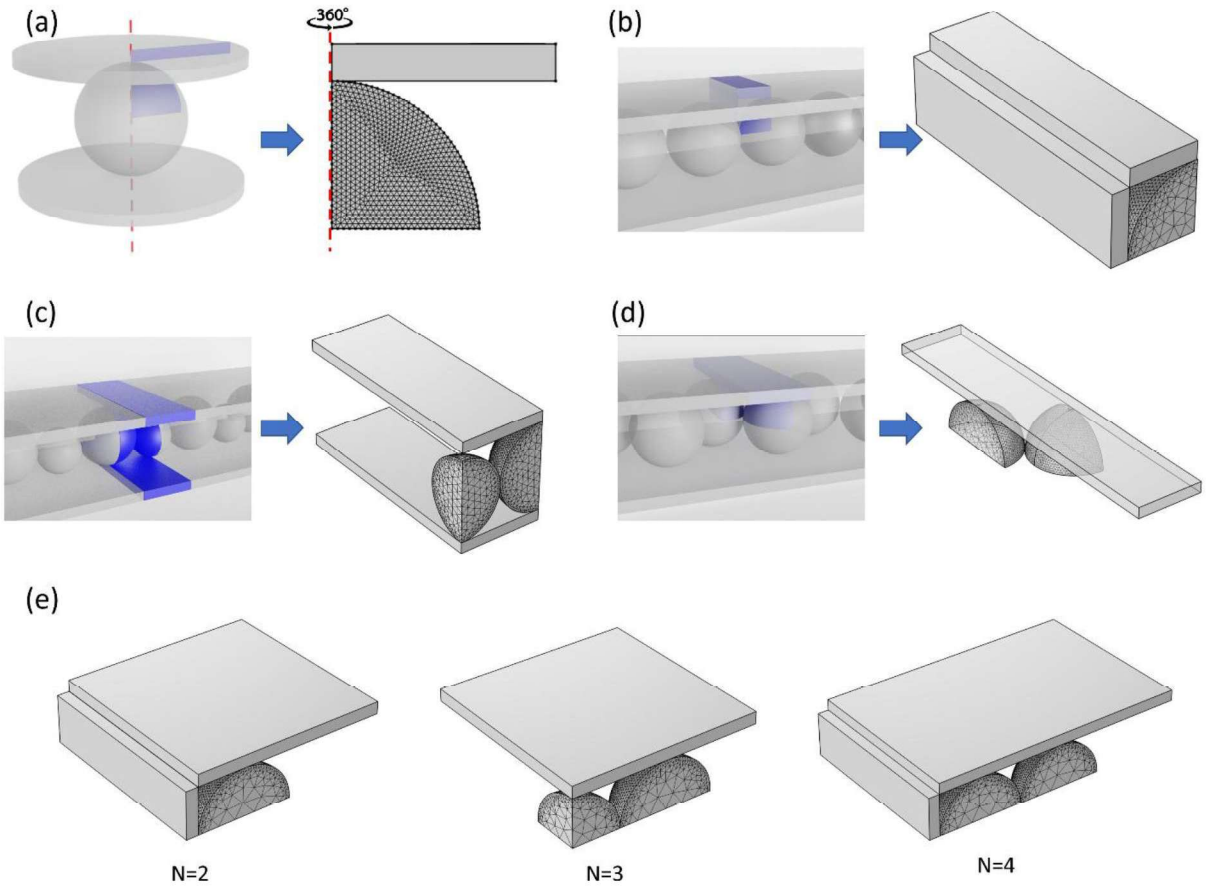

Figure 11. Geometrical reductions and meshing strategies used in the compression simulations. (a) Single-sphere compression simplified to a 2D axisymmetric model, where only one quarter of the sphere cross section is meshed and revolved. (b Infinite chain of spheres reduced to a 3D one-eighth sphere segment with mirror boundary conditions. The neighboring sphere was substituted by a rigid symmetry plate, which mimics the presence of adjacent particles and allows proper simulation of interparticle contact. Additional symmetric reductions applied for configurations involving (c) polydispersity and (d) misalignment of infinity chains, allowing efficient computation while retaining the relevant deformation mechanisms. (e) Examples of finite chain reductions for finite particle quantity: N = 2, 3, and 4 spheres compressed between rigid plates.

3.1.2. Physics setup

Solid mechanics. The solder particles were modeled as **plastic solids** using the Johnson–Cook (J–C) constitutive law with isotropic hardening. This formulation was chosen because it captures the combined effects of strain hardening, strain-rate sensitivity, and thermal softening, which are all relevant for $Sn_{63}Pb_{37}$ solder. The model parameters were calibrated against single-sphere compression experiments, as described in rheological measurements (chapter 2.3), and the final optimized set of parameters was consistently applied in all subsequent simulations.

Contact interactions between the particles and the compression plates were defined using the Augmented Lagrangian contact method. This approach offers higher robustness than pure

penalty methods by combining penalty enforcement with a Lagrange multiplier correction. The algorithm was set up in a fully coupled manner to ensure stable convergence under large strains. To improve numerical stability, the penalty factor was manually tuned, and the Lagrange multiplier update was scaled with a factor of 0.9. Tangential behaviour at the contact was described by Coulomb friction, with a coefficient of friction of 0.15. No additional cohesion was included (cohesion sliding resistance $= 0$), and the maximum tangential traction was set to infinity, so that the interface response was controlled entirely by the friction coefficient.

The **compression plates** were modelled as rigid bodies. The lower plate was fixed in space. The upper plate was defined by a prescribed displacement at its centre of rotation, with all rotational degrees of freedom constrained. This setup is equivalent to prescribing a vertical displacement, but it ensures that the rigid plate remains stable and numerically well-conditioned in the contact algorithm. The displacement boundary condition was expressed as $U_z = -v/2 \cdot t$, where v is the defined loading velocity. This approach enforced a constant engineering strain rate while maintaining the rigid-body character of the plate throughout the simulation.

Symmetry conditions were applied along the boundaries identified in Section 3.1.1. For single-sphere simulations, a 2D axisymmetric reduction was used, with the symmetry axis aligned to the loading direction and an additional plane of symmetry defined through the equator of the sphere where 3D model was involved. For chain simulations and other multi-particle cases, the symmetry conditions were adjusted accordingly (1/8-sphere reductions, or more complex partitions depending on polydispersity or misalignment), which significantly reduced computational cost without compromising accuracy.

3.1.3. Meshing & study settings

The compression plates were meshed with a mapped mesh consisting of a single element. Since the plates were modeled as rigid bodies, this minimal discretization was sufficient to provide stable contact interactions without introducing unnecessary degrees of freedom.

The solder spheres were discretized using a free tetrahedral mesh. On the particle surface, a size distribution control was applied with a maximum element size of 5 µm. This ensured accurate resolution of the steep stress and strain gradients that develop beneath the contact patches during compression, while keeping the overall element count manageable. The mesh was globally calibrated for general physics, with the predefined “normal” setting as a starting point, and locally refined in contact regions where stress concentrations were expected.

All simulations were carried out using a **time-dependent study**. The output was recorded at evenly spaced intervals defined by $t = range(0, total\ time/100, total\ time)$, providing 100 output steps for each compression run. A user-controlled relative tolerance of 0.001 was imposed to ensure numerical accuracy.

The time-dependent solver was modified from COMSOL’s default settings to improve stability during large-strain contact problems:

- **Time stepping**: implicit solver, BDF method; steps were restricted to be strictly controlled by the solver.

- **Algebraic variable settings**: consistent initialization by Backward Euler, with the fraction of the initial step set to 0.001 and the safety factor set to 20. Error estimation was modified to exclude algebraic variables.
- **Fully coupled solver**: a direct linear solver was employed. The nonlinear method was set to constant Newton iterations, with a damping factor of 0.9 and a maximum of 64 iterations per step.

These adjustments were critical for achieving convergence in highly nonlinear regimes where large deformations, contact sliding, and strain-rate dependent material behavior all interact. In particular, the combination of strict time stepping and Backward Euler initialization improved robustness at the onset of contact, while the damping factor and iteration cap-controlled stability during rapid plastic flow at higher strains.

3.2. Electrical resistance

Electrical resistance is one of the key parameters that determines the functional performance of particle-based conductive structures. While mechanical compression defines the quality of interparticle contact, predicting the corresponding resistance is not straightforward. The first attempts of simulations (where only shape was taken into account and contact was union) showed results that were far from the experimental values. This discrepancy highlighted several unsuspected challenges: the necessity to account for surface roughness, the presence of oxide layers, and the strong dependence on contact pressure. Another major source of error was the estimation of the actual interparticle contact area. Increasing the mesh density for compression simulations improved this estimation but also significantly extended computation times.

Furthermore, resistance is inherently coupled with thermal effects. The passage of current generates Joule heat, which dissipates through the material and surrounding air. To capture these effects, a multiphysics framework was implemented. **Electrical currents** and **heat transfer in solids** were connected by the electromagnetic heating interface. This coupling enabled simultaneous evaluation of both the electrical resistance and the resulting temperature distribution, providing results that could be directly compared to experiments.

3.2.1. Geometry

For the resistance simulations, particle shapes deformed under different compression levels were taken directly from the mechanical studies described in Section 3.1. Each imported geometry represented only one-eighth of a sphere, corresponding to the simulation domain used in the mechanical compression step. To obtain the full two-sphere configuration, these reduced geometries were mirrored along the symmetry planes, which resulted in the block-like appearance of the final structures. Figure 12 shows the final meshed geometries after this reconstruction for compression strains of 10% and 50%. This approach ensured that the particle shapes and contact regions reflected realistic compression states, while keeping the computational cost manageable.

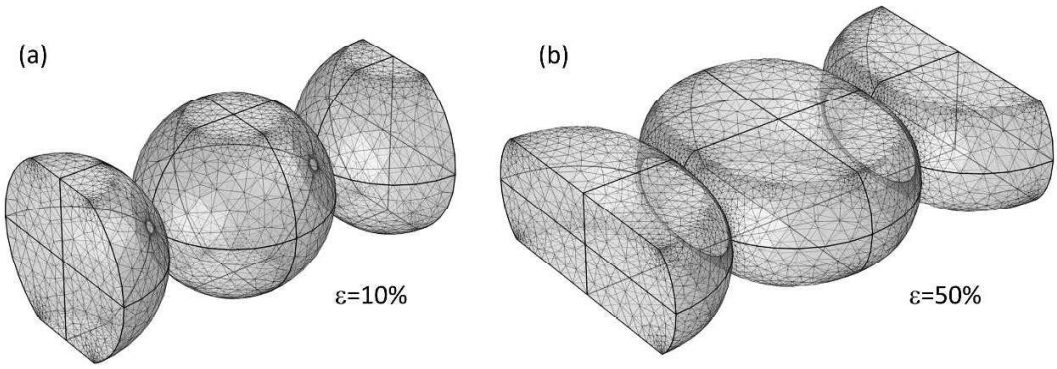

Figure 12. Deformed sphere's configurations imported from mechanical compression results and used in electrical simulations. The meshes correspond to compressive strains of (a) ε = 10% and (b) ε = 50%. The particle shapes and contact areas were directly taken from prior mechanical models to ensure realistic geometry input.

3.2.2. Physics setup

Electrical currents. A current of $100\ mA$ was applied at the cross-section of one sphere, while the opposite cross-section of the neighboring sphere was set as ground. This configuration simulated the current flowing through a single interparticle connection. The contact properties were modeled using the pair electrical contact condition with surface roughness parameters measured experimentally by surface characterization described in Section 2.4 (asperity average height and slope). The contact pressure (different for each compression degree, compression speed and size of the particle), previously obtained from the mechanical compression study, was directly imported into the electrical model, allowing consistent coupling between the two simulations. The hardness of the material was set to the microhardness value of $3\ GPa$, taken as an average from the literature and is described in **[Scientific paper III]**. Boundary conditions on the symmetry planes were identical to those defined in the geometry.

Heat transfer in solids. The initial temperature of the system was set to room temperature. Thermal continuity was applied across the contacts to allow heat transfer between spheres. Convective heat flux was imposed on all external surfaces, corresponding to natural convection in air. Symmetry planes followed the same definition as in the electrical model.

3.2.3. Mesh & study settings

The mesh was identical to that used in the mechanical compression simulations, ensuring consistency in contact surface representation. A time-dependent study was performed to capture both the heat generation from current flow and the subsequent dissipation into the environment.

To cover the full range of compression states, electrical simulations were performed for approximately 80 compression degrees obtained in Section 3.1. Because this process was computationally intensive, it was automated through a custom script written in the Application Builder. The script executed the following steps:

1. Applied the corresponding geometry and contact pressure (from previous mechanical study) to the electrical model.
2. Ran the electrical–thermal simulation.

3. Saved the calculated results (resistance, temperature).
4. Moved to the next compression state and repeated the cycle.

The automated framework greatly reduced manual intervention and ensured systematic evaluation across the entire compression spectrum. The script is provided in **Appendix B: Automated electro-thermal simulations in COMSOL**.

3.3. Joule heating and melting

The heat transfer simulations presented in the previous section indicated that the highest current densities occur in the interparticle contact regions, where the effective cross-section of the structure is smallest. As a result, these regions are subjected to the most intense Joule heating. This effect is especially pronounced at low compression degrees, where the contact area between particles remains minimal.

Rather than treating this localized heating as a limitation, it can be exploited as a functional advantage. If sufficient power is applied, the generated heat may reach the melting point of the solder material ($Sn_{63}Pb_{37}$) from which the particles are made. Melting at the contacts would allow permanent metallurgical bonding between adjacent particles, thereby reducing the influence of factors such as surface oxides, surface roughness, applied pressure, and microhardness on electrical conductivity.

To evaluate the feasibility of this process, simulations were performed to determine the power conditions (current or voltage, duration of application) required to induce melting. The model also accounted for convection, phase transitions (melting and solidification), and geometry changes induced by local fluidization of the solder.

3.3.1. Geometry

Direct simulation of a particle chain with an arbitrary number of spheres is computationally impractical. To reduce complexity, geometric symmetries were introduced. The chain was assumed to be perfectly linear and composed of monodisperse spheres. This allowed the model to be reduced to a 2D axisymmetric representation with two additional symmetry planes through the center of a spheres (Figure 13).

The interparticle contact area was rounded and assigned a nominal diameter/neck's height (h) of 20 µm for 760 µm spheres (contact arc percentage ~0.84%). Attempts to further decrease this size resulted in convergence issues and required prohibitively fine meshing. Thus, 20 µm was chosen as a practical compromise between physical accuracy and computational efficiency.

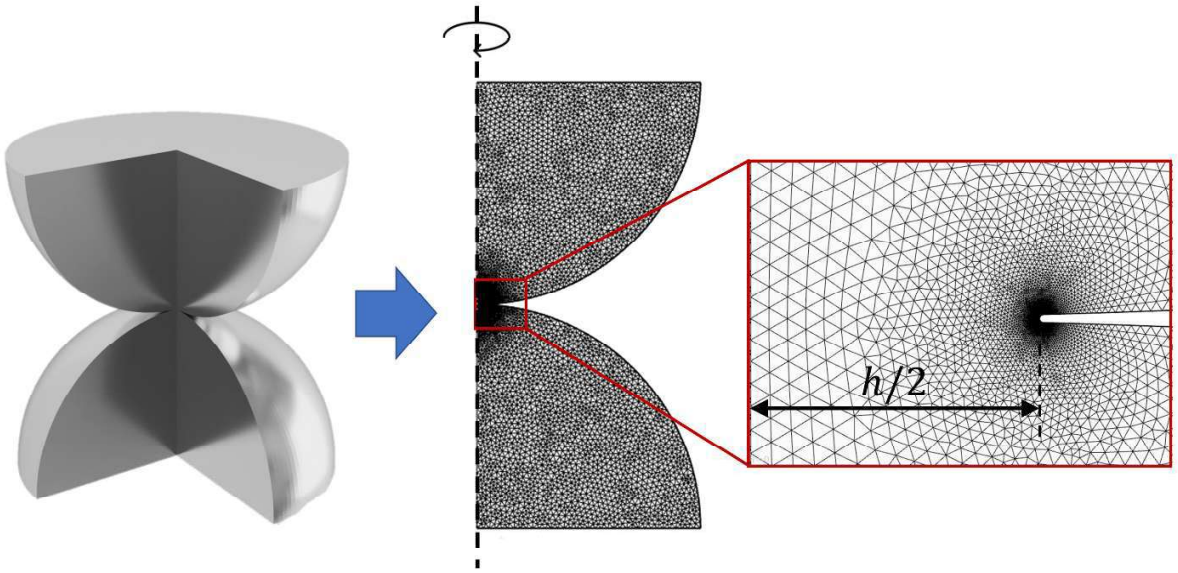

Figure 13. Geometry reduction and meshing strategy for chain-of-spheres model. Left: the 3D chain is idealized as perfectly linear and monodisperse; Center: axisymmetric cross-section with graded mesh; the dashed line is the axis of revolution. Right: zoom at the interparticle contact where the contact is rounded and assigned neck's height h. For 760-µm spheres, $h = 20\ \mu m$ was used. The arrow indicates $h/2$ from the symmetry axis to the contact edge.

3.3.2. Physics setup

Several multiphysics interfaces were coupled to capture the relevant phenomena:

Moving Mesh. Shape evolution during melting was handled using a moving mesh approach with symmetric boundaries. Deforming Domain was prescribed to a whole simulated domain.

Electric Currents. A terminal with applied current (I) was set on the cross-section at the sphere's center, while ground was defined at the interparticle contact boundary. This setup enabled simulation of current flow through a single contact.

Incompressible Laminar Flow. No-slip conditions were applied to the same boundaries where current and ground were defined. A free surface with a surface tension coefficient of $0.034\ N/m$ was assigned at the particle-air interface (the air domain was not explicitly modeled). The entire domain was treated as a liquid, but very high viscosity values were assigned to regions representing the solid phase to prevent deformation. Shape changes were only allowed in molten regions, with dynamic viscosity defined as a temperature-dependent function:

$$\mu(T) = \theta_1\mu_1 + \theta_2\mu_2$$

where θ_1 and θ_2 – indicators of solid and liquid phases, μ_1 and μ_2 dynamic viscosities of solid and liquid phases respectively.

Heat Transfer in Fluids. Phase change was modeled using a Heaviside transition function. The melting temperature was set to $456.13\ K$ ($Sn_{63}Pb_{37}$ melting point), with a phase transition interval of $10\ K$ (smaller values required significantly more computational resources). The latent heat of fusion was set to $47\ J/kg$. Material properties of the solid and liquid phases were defined

according to reference data and are presented in **[Scientific paper V]** (Table 2). Convective heat flux was imposed at the particle surface, assuming air at rest (velocity $= 0\ m/s$).

All physics were coupled through the Electromagnetic Heating and Nonisothermal Flow multiphysics interfaces, ensuring feedback between current flow, heat generation, melting, and geometry changes.

3.3.3. Mesh and study settings

The particle domain was meshed with a free triangular grid calibrated for fluid dynamics (predefined "normal"). Edge distributions were refined along the particle surface, with additional density near the interparticle contact to improve accuracy.

A time-dependent study was employed with relative tolerance set to 0.05. Time steps were adjusted depending on the applied power conditions to ensure stability and convergence.

3.4. Electrostatic attractive force

Electrostatic attraction plays a decisive role in initiating the assembly of conductive microparticle chains. When an external voltage is applied, a particle located near the substrate experiences an electric field gradient that generates a vertical force pulling it toward the surface. This effect competes with the capillary force that normally keeps the particle at the meniscus interface. The balance between these two forces determines the threshold voltage for particle detachment and chain formation.

Numerical simulations were performed to quantify the magnitude of the electrostatic force under different experimental conditions. In particular, the dielectric properties and thickness of the substrate were examined, since these parameters significantly influence the strength of the attractive interaction.

3.4.1. Geometry

The simulation geometry closely mimicked the experimental configuration. A conductive spherical microparticle was placed at a distance H above a planar substrate, positioned partially inside a hemispherical cavity. This cavity served as a simplified approximation of the liquid meniscus at the capillary tip. The upper region represented air (dielectric constant $\varepsilon_1 = 1$), while the lower region was a dielectric slab of thickness d, corresponding to the glass substrate used in experiments ($\varepsilon_2 = 4$). The thickness d was varied from 30 mm to 0 mm: the former approximates an ungrounded insulating substrate, while the latter represents the limiting case of a grounded conductive substrate. A 2D axisymmetric representation was used to model the full 360° device. The full axisymmetric domain and the definitions of H and d are shown in Figure 14.

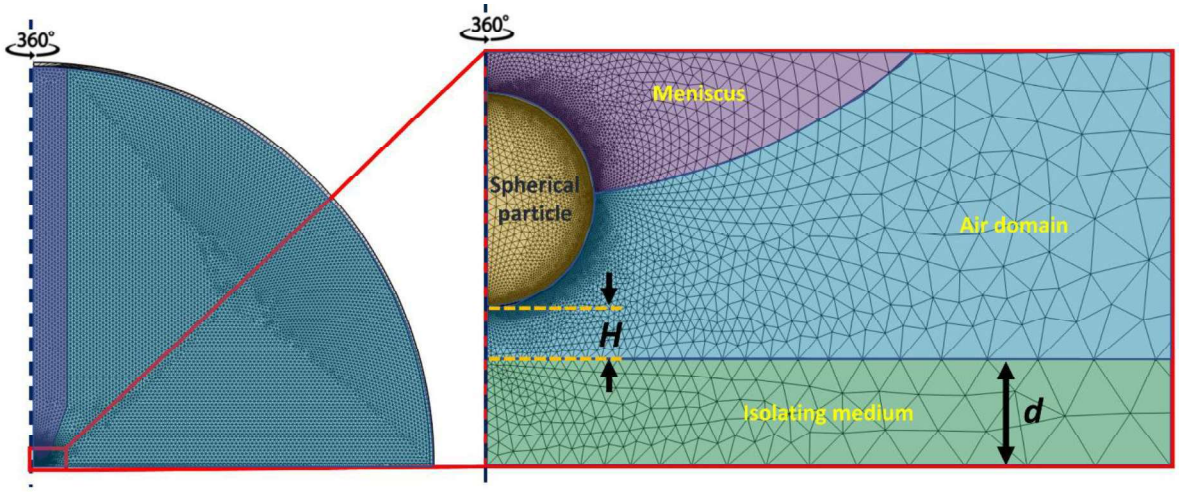

Figure 14. Axisymmetric electrostatic model and mesh. Left: full 2D axisymmetric computational domain (360° by revolution) with graded triangular mesh. Right: zoom of the particle–meniscus–substrate region showing the air domain (blue), meniscus cavity (purple), and dielectric substrate (green) of thickness d. The particle–substrate gap H is indicated by dashed guides. The particle, conduit, and meniscus are set to potential U; the bottom boundary is grounded. The mesh is refined around the sphere's edge and in the gap to resolve strong field gradients.

3.4.2. Physics setup

The electrostatic field was modeled by first determining the potential distribution through the solution of Laplace's equation. Several boundary conditions were then applied to the model.

For simplicity, a fixed potential (U) was assigned to the electrodes, which included the conduit, meniscus, and particle. The bottom boundary of the domain was grounded. The dielectric slab, serving as the substrate model, was maintained as electrically neutral. To represent the exterior, an Infinite Element Domain was set as a thin layer surrounding the air domain.

Following the calculation of the potential distribution, the spatial distribution of the electric field was extracted. Subsequently, the vertical component of the electrostatic force (F_e) acting on the particle was determined as a function of the normalized particle-substrate distance H.

3.4.3. Mesh and study settings

Figure 14 (right) also shows the graded mesh with strong refinement in the gap H. The computational domain was discretized using a free triangular mesh in 2D axisymmetric representation. The mesh was refined in the gap between the particle and the substrate, where the strongest field gradients occur. Away from this region, the element size was gradually increased to reduce computational cost.

The study was performed in stationary mode with the applied potential U as a parameter. For each voltage, the particle-substrate distance H was varied systematically, and the corresponding electrostatic force was computed.

4. Overview of the publications constituting the dissertation

This chapter links the five papers that make up the thesis **[Scientific Papers I–V]**. The aim is to understand how single-particle-thick structures can be formed, how they deform, and how their electrical contacts emerge. **Papers I–II** establish the formation step: particles are extracted from a liquid meniscus under an electric field and placed as one-bead-thick lines. These two papers define the operating window and show which parameter govern initiation, stability, and length.

With stable lines available, **Paper III** examines their mechanical response. It measures and models compression of individual beads and full chains to quantify contact growth and the roles of temperature and strain rate. **Paper IV** then connects this mechanics to charge transport by measuring resistance in real time during compression and relating it to interparticle contact. Finally, **Paper V** explores an alternative post-processing route: electrical excitation is used to form conductive necks between neighboring beads when macro-compression is impractical.

[Scientific paper I]: "Fabrication of 1D particle structures outside a liquid environment using electric and capillary interactions: From fundamentals to applications"

This paper presents an uncomplicated, efficient, and easy-to-implement method for fabricating one-dimensional (1D), single-particle-thick structures outside of a bulk liquid environment. The technique addresses the significant challenge that conventional methods are often expensive, time-consuming, or require access to advanced laboratory facilities, which has hindered the development and application of these materials.

The developed method utilizes a combination of electric and capillary interactions to assemble microparticles into long, chain-like structures. The process involves dispersing electrically conductive particles in a nonpolar, weakly conductive liquid. An electrode under an applied AC voltage is used to attract the particles and pull them out of the liquid phase. As the electrode is lifted, particles are successively added to the chain, which is stabilized by both electrostatic forces and capillary bridges formed by the dispersing liquid. This assembly process is rapid, capable of forming long chains in seconds.

A detailed investigation was conducted to understand the fundamental physics and optimize the fabrication process. The key findings are as follows:

1. **Method versatility:** The technique is robust and functions with a wide variety of materials. It has been successfully demonstrated with different types of microparticles, including solid (stainless steel, solder), core-shell (Ag-coated silica), and soft (conductive hydrogel)

particles, as well as non-spherical shapes like discs. The process is effective regardless of whether the particle density is greater or less than the liquid density.

2. **Role of capillary forces:** Capillary interactions were found to be crucial for the formation of high-quality structures. Two types of capillary bridges were identified:
    - **Type I** (particle-planar liquid surface): This bridge forms as a particle is pulled from the liquid interface. While it creates a downward force that must be overcome by the electric field, it plays a vital role in aligning particles vertically and preventing the formation of irregular agglomerates, ensuring a single-particle-thick structure.
    - **Type II** (particle-particle): These bridges form between adjacent particles in the chain after they leave the bulk liquid. They provide strong attractive interactions that ensure the chain's stability even after the electric field is turned off.
3. **Influence of liquid properties:** The choice of dispersing liquid significantly impacts the process. The study found that liquids with high viscosity and low ionic conductivity are preferred. This is because at low frequencies of the applied voltage, mobile ions in the liquid can cause electrostatic screening, weakening the electric force. Higher viscosity liquids reduce ionic diffusivity, shifting this screening effect to lower frequencies. The threshold frequency (f_{th}) was found to scale inversely with viscosity (η), following the relationship $f_{th} \propto \eta^{-1}$.
4. **Process parameters:** The pulling rate was identified as a key parameter for controlling the volume of liquid in the Type II capillary bridges and, consequently, the stability of the final structure. A rough guideline for the maximum pulling speed was established as $v \cdot \eta / R < 1\ Pa$, where v is the velocity, η is the viscosity, and R is the particle radius.

Finally, the potential applications of these 1D structures were explored. The method enables the fabrication of freestanding chains whose mechanical properties, such as bending stiffness, can be tuned by the applied electric voltage. Furthermore, the study demonstrates the deposition of these particle chains onto a substrate to create electrically conductive micropaths. A post-processing step, such as mechanical compression, significantly increases the contact area between particles, reducing the electrical resistance by several orders of magnitude and creating highly conductive pathways. This work unlocked the potential of 1D particle structures for fundamental research which are studied deeply in the next papers.

[Scientific paper II]: "Single-particle-thick microstructures fabricated through controlled withdrawal of particles from a dispersion meniscus"

This research significantly advances the fabrication of single-particle-thick microstructures by introducing a novel, continuous, and scalable method that overcomes the limitations of the previous batch-based approach. Drawing an analogy to the evolution from a quill pen requiring repeated dipping to a ballpoint pen with a continuous ink supply, this work transitions from using

a simple needle electrode to a conduit that provides a constant feed of particles to a dispersion meniscus. Microparticles are electrically extracted from this meniscus to form a chain, a process whose governing physical mechanisms and instabilities are distinctly different from the prior method and are investigated in detail here.

The results of this in-depth study can be summarized as follows:

1. **Force balance and process initiation:** The initiation of chain formation is governed by a balance between the downward electrostatic force (F_e) pulling a particle from the meniscus and the upward restoring capillary force (F_{sp}) holding it at the liquid-air interface. Numerical simulations and experiments confirmed that the strength of the electric force is highly dependent on the substrate's electrical properties; conductive substrates generate a much stronger attraction than insulating ones, significantly lowering the voltage required to begin the process.
2. **Identification of key instabilities:** The maximum achievable chain length (L_{max}) is limited by two primary, voltage-dependent failure modes:
    - **Electric-force-limited breakage:** At low applied voltages, the cohesive electric force is insufficient to support the chain's weight against capillary and gravitational forces, causing the chain to break, typically near the meniscus.
    - **Substrate-induced instability:** At high applied voltages, a strong electrostatic attraction between the particle chain and a non-conductive substrate causes the chain to bend and "unravel" onto the surface in an uncontrolled manner. This phenomenon becomes the dominant factor limiting chain length at higher voltages.
3. **Strategies for mitigating instability:** Based on the understanding of these instabilities, the research demonstrates effective strategies to suppress them and form longer chains. Substrate-induced instability can be completely eliminated by using a conductive substrate, as the chain and the substrate are at the same electrical potential, negating the attractive force. Alternatively, modifying the geometry of a non-conductive substrate from flat to a narrow cylinder significantly weakens the interaction, allowing for the formation of longer chains at higher voltages.
4. **Influence of gravity and particle properties:** On conductive substrates where instability is suppressed, the maximum chain length is ultimately limited by the chain's own mass. The chain grows until its gravitational force (F_g) overcomes the capillary anchoring force (F_{sp}) at the meniscus, causing the chain to self-sag and accumulate on the substrate rather than growing longer. This leads to a clear scaling relationship where the number of particles in the chain (N) is inversely proportional to the square of the particle radius (r), or $N \propto r^2$. This confirms that smaller, lighter particles can form significantly longer suspended structures.

5. **Demonstration of advanced applications:** The fundamental knowledge gained enabled several novel application-driven demonstrations, including:
    - Continuous 3D Fabrication: Winding a particle chain into a continuous helical structure around a rotating optical fiber.
    - Freestanding Electrical Interconnects: Forming suspended particle chains to bridge copper terminals on separate printed circuit boards, creating structures analogous to wire bonds.
    - Mechanically Resilient Microstructures: Showing that a suspended particle chain can withstand hundreds of axial compression-relaxation cycles without failure, outperforming solid solder and copper wires by more than an order of magnitude.
    - Voltage-Controlled Actuation: Demonstrating the ability to reversibly extend and retract a suspended chain simply by modulating the applied voltage, creating an "electrostatically controlled tendon" without any moving parts.

[Scientific paper III]: "Experimental and FEM simulation study of compressive deformation of solder microballs and particle chains"

This publication investigates the fundamental mechanics of post-processing beaded microstructures via mechanical compression, a critical step for transforming them into functional, conductive micropaths. The research systematically examines the compressive response of malleable solder microballs, first by establishing a baseline understanding of unconstrained, individual particles and then by comparing this to the more complex behavior of particles arranged in a linear, side-by-side chain. The study combines extensive experimental work with Finite Element Method (FEM) simulations to provide a comprehensive analysis of the deformation process.

The results presented in the paper can be summarized as follows:

1. **Empirical scaling law for single particle compression:** A comprehensive experimental study on individual solder balls established a clear empirical relationship for the required compressive force(F_N). The force scales quadratically with the particle diameter $(F_N \propto d^2)$, exhibits a very weak power-law dependence on the engineering strain rate $(F_N \propto \dot{\varepsilon}^{0.12})$, and shows a strong dependence on temperature, following the thermal softening factor $F_N \propto [1 - T^{*0.7}]$.
2. **Dominant effect of temperature over strain rate:** The results demonstrate that temperature has a significantly more pronounced effect on the material's mechanical strength than the strain rate. While increasing temperature leads to substantial material softening and a large reduction in the required compressive force, the influence of strain rate is weak. This finding has important implications for optimizing industrial processes

like calendering, as it allows for faster processing speeds without a major increase in applied force.

3. **Accuracy of the Johnson-Cook (J-C) model:** FEM simulations successfully replicated the experimental findings. The Johnson-Cook (J-C) plasticity model proved to be a robust and accurate predictor of the solder microballs' compressive behavior across the wide range of strains, strain rates, and temperatures investigated. After parameterization based on the experimental data, the model allowed for the analysis to be extended beyond the physical limitations of the equipment.
4. **Increased compression force in particle chains:** The central hypothesis of the study was confirmed: linearly arranged particle chains exhibit greater resistance to deformation than an equivalent number of unconstrained, separated particles. This is due to lateral constraints imposed by neighboring particles, which limit the freedom of each microball to deform, thus requiring a higher compressive force to achieve the same level of strain.
5. **Quantification of the constraint effect:** The difference in the required compressive force between the "in-line" and "separated" configurations was shown to increase with both the compressive strain and the number of particles in the chain. This difference becomes significant at strains above 20% and grows as the chain lengthens, asymptotically approaching a theoretical limit predicted for an infinite chain once the chain consists of approximately 10 or more balls.
6. **Analysis of contact pressure distributions:** The simulations provided an in-depth view of contact pressures, which are difficult to measure experimentally. It was found that both the plate-particle and inter-particle contact pressures are higher in the chain configuration compared to unconstrained particles. This is attributed to the geometric constraints concentrating the load at the contact points and is critical for understanding the mechanisms of solid-state bonding and the formation of robust electrical pathways in these structures.

[Scientific paper IV]: "Fabrication of a new type of electrically conductive micro-tracks via mechanical compression of beaded structures"

This research presents a complete framework for fabricating functional, electrically conductive micro-tracks from beaded particle structures, positioning them as a viable and sustainable alternative to conventional silver nanoparticle-based pastes. This study focuses on the critical post-processing step: uniaxial mechanical compression. The work establishes a quantitative relationship between the mechanical deformation of a particle chain and its resulting electrical conductivity. Through a combination of comprehensive experiments and validated Finite Element Method (FEM) simulations, the study explores how compressive strain, particle arrangement, and material properties govern the final electrical performance of these micro-tracks.

The results presented in the paper can be summarized as follows:

1. **Quantitative Strain-Resistance Relationship:** The study successfully established a direct and repeatable relationship between the compressive strain (ε) and the electrical resistance (R) of a particle chain. The resistance was shown to decrease by several orders of magnitude, from an initial open-circuit state ($> 10^8$ Ω) to milliohm levels at high compression, achieving conductivity comparable to micro-tracks made from silver nanoparticle pastes and approaching that of a solid wire of the same material.
2. **Validated Electromechanical Model:** A comprehensive FEM simulation was developed to model the entire electromechanical process. The model accurately predicted the physical deformation of particles, the growth of both the plate-particle contact area (A_1) and the crucial inter-particle contact area (A_2), and the resulting electrical resistance as a function of strain. The model's accuracy was validated by the close agreement between simulated and experimentally observed particle shapes.
3. **Impact of Surface Roughness on Conduction:** Simulations revealed that the initial sharp drop in resistance is dominated by constriction resistance. A simple model assuming perfectly smooth contacts ('union' model) failed to capture the behavior of solder particles at low strains. However, by incorporating a declining surface roughness parameter that diminishes to zero within the first 5% of strain, the simulation achieved excellent agreement with experimental data, underscoring the critical role of asperity flattening in establishing initial conductive pathways.
4. **Scaling of Resistance with Particle Size:** At high levels of compression ($\varepsilon \approx 70\%$), the minimum achievable resistance (R_{min}) was found to scale inversely with the square of the particle radius ($R_{min} \propto \mathrm{r}^{-2}$). This experimental finding aligns with the theoretical resistance of a solid conductor whose cross-sectional area is equivalent to the inter-particle contact area (A_2) of the compressed chain.
5. **Effects of Non-Ideal Configurations:** The study investigated more realistic scenarios, including polydispersity and misalignment:
    - Polydispersity: Counter-intuitively, chains with moderate particle size polydispersity exhibited a faster initial decrease in resistance at low strains compared to monodisperse chains. This is attributed to plastic indentation mechanisms between different-sized particles, which more rapidly increase the contact area in the early stages of compression.
    - Misalignment: Chains with a zigzag arrangement were shown to have higher resistance than perfectly linear chains, with the difference increasing as the deviation angle becomes larger.
6. **Practical Application on Delicate Substrates:** A key practical challenge - applying high compressive forces to fragile substrates - was addressed. The research demonstrated that by elevating the process temperature (*e.g.*, to $130\ ^\circ C$), the force required for compression is reduced by over an order of magnitude. This allows for the successful formation of a

flattened, conductive micro-track on a delicate silicon wafer without causing damage, proving the method's feasibility for real-world electronic applications like solar cells.

[Scientific paper V]: "Formation of conductive beaded structures via Joule heating"

In practice, pressing beaded chains may be often not an option for some applications. The substrate must be rigid enough to withstand an applied force and elevated temperature; populated substrates with electronic components cannot be pressed at all; and thin films or membranes are intolerant to pressure gradients. Instead, the method to sidestep these limitations has been found - electrical sintering. This process is described here: a controlled electrical excitation forms metallic necks directly between neighboring solder microspheres, turning fragile point contacts into continuous, low-resistance joints without external pressing.

The results presented in the paper can be summarized as follows:

1. **Necks form fast and scale predictably with voltage.** When two solder spheres touch under a set DC voltage, a metallic neck appears within about a millisecond. Across many repeats, the final neck height follows a robust power law with voltage (approximately $h \propto U^{0.7}$). This gives a simple design handle: choose the voltage to target a neck size (and thus an electrical/mechanical performance level) without changing the fixture or materials.
2. **Brief current overshoots trigger local melting and start the join.** Low-cost supplies do not clamp current instantly; the first microseconds deliver a short overshoot that can reach tens of amperes. That spike concentrates Joule heating at the tiny constriction, pushes the contact above the melting point, and initiates neck growth. Time-dependent simulations driven by the measured pulses explain why joining can succeed with set voltages.
3. **The initial contact size sets the thermal trajectory** (and a practical preload limit). A very small initial contact focuses current and heat, producing higher peak temperatures and faster neck growth for the same waveform. If the beads are pre-pressed too hard, the contact spreads, current density drops, and the junction may never reach melting - electrical sintering then fails. This maps a clear upper bound on preload/contact diameter for reliable joining.
4. **Waveform choice controls outcome**. Using the same starting contact, constant-current and especially constant-power excitation keep the junction hot longer, drive larger necks, and yield a smoother, deeper drop in resistance than the natural, quickly decaying spike from a budget supply. This points to practical drive modes when a specific neck size or target resistance must be reached.
5. **Multiple junctions in a chain can be fused in one step, and growth self-stabilizes**. In five-bead lines (even with mixed bead sizes) several contacts fuse within a single pulse,

producing continuous conductive paths. As each neck widens, its local resistance and heating fall, so growth naturally stops without runaway coalescence. This self-limiting behavior makes the process gentle on substrates and repeatable at scale.

5. Conclusions

This Ph.D. dissertation contributes to the fundamental understanding of how microparticles can be assembled into one-particle-thick chains and micropaths under the combined action of electric fields and capillary forces. The work identifies the essential physical mechanisms of chain formation, including field-driven alignment, capillary stabilization, and interparticle contact formation, and shows how these processes determine the initial geometry and properties of the structures.

Beyond assembly, the research emphasizes post-processing as a key step in defining the final behavior of the micropaths. Mechanical compression was shown to enlarge the contact regions between particles, reducing electrical resistance and improving mechanical stability. Joule heating, in turn, was identified as a complementary post-processing method, where localized heating at small contacts can drive controlled melting and reflow, creating permanent and highly conductive junctions. Together, these techniques highlight how particle assemblies can evolve from fragile, field-driven chains into robust structures with tunable properties.

A central element of this dissertation has also been the use of computer simulations. Multiphysics models combining electrical currents, heat transfer, and mechanics were developed to capture the coupled processes governing conductivity and structural change. These simulations provided insights into the influence of contact roughness, oxide layers, and compression, while also explaining discrepancies between early simplified models and experimental results. Although not yet fully predictive, the models establish a framework for future studies of particle assemblies as coupled electro-thermal-mechanical systems.

Taken together, this work advances the basic physics of particle-based micropaths. It demonstrates how assembly, post-processing, and simulation can be combined to uncover the governing mechanisms of stability, conductivity, and structural evolution. The results provide a foundation for continued fundamental research into one-particle-thick assemblies and their behavior at the intersection of soft matter, condensed matter, and field-driven systems.

6. References

1. Bharti, B., Findenegg, G. H. & Velev, O. D. Co-Assembly of Oppositely Charged Particles into Linear Clusters and Chains of Controllable Length. *Sci Rep* **2**, 1004 (2012).

2. Bharti, B., Findenegg, G. H. & Velev, O. D. Analysis of the Field-Assisted Permanent Assembly of Oppositely Charged Particles. *Langmuir* **30**, 6577–6587 (2014).

3. Shabaniverki, S. & Juárez, J. J. Directed Assembly of Particles for Additive Manufacturing of Particle-Polymer Composites. *Micromachines (Basel)* **12**, 935 (2021).

4. Chai, Z., Childress, A. & Busnaina, A. A. Directed Assembly of Nanomaterials for Making Nanoscale Devices and Structures: Mechanisms and Applications. *ACS Nano* **16**, 17641–17686 (2022).

5. He, Y., Liu, J., Yang, X., Yang, J. & Jiao, F. Recent progress in field-directed assembly of colloids in an evaporating droplet. *Mater Today Bio* **33**, 102072 (2025).

6. Rozynek, Z. *et al.* Formation of printable granular and colloidal chains through capillary effects and dielectrophoresis. *Nat Commun* **8**, (2017).

7. Dutka, F., Rozynek, Z. & Napiórkowski, M. Continuous and discontinuous transitions between two types of capillary bridges on a beaded chain pulled out from a liquid. *Soft Matter* **13**, 4698–4708 (2017).

8. Klocke, F., Wagner, C. & Klocke, F. Coalescence Behaviour of Two Metallic Particles as Base Mechanism of Selective Laser Sintering. *CIRP Annals* **52**, 177–180 (2003).

9. Suetsugu, N. & Iwase, E. Conduction Conditions for Self-Healing of Metal Interconnect Using Copper Microparticles Dispersed with Silicone Oil. *Micromachines (Basel)* **14**, 475 (2023).

10. Allen, K. W. *et al.* Microsphere-chain waveguides: Focusing and transport properties. *Appl Phys Lett* **105**, (2014).

11. Mitsui, T. *et al.* Influence of micro-joints formed between spheres in coupled-resonator optical waveguide. *Opt Express* **19**, 22258 (2011).

12. Ahn, W., Zhao, X., Hong, Y. & Reinhard, B. M. Low-Power Light Guiding and Localization in Optoplasmonic Chains Obtained by Directed Self-Assembly. *Sci Rep* **6**, 22621 (2016).

13. Breidenich, J. L. *et al.* Controlling length and areal density of artificial cilia through the dipolar assembly of ferromagnetic nanoparticles. *Soft Matter* **8**, 5334 (2012).

14. Hill, L. J. & Pyun, J. Colloidal Polymers via Dipolar Assembly of Magnetic Nanoparticle Monomers. *ACS Appl Mater Interfaces* **6**, 6022–6032 (2014).

15. Jiang, X. *et al.* Bioinspired 1D Superparamagnetic Magnetite Arrays with Magnetic Field Perception. *Advanced Materials* **28**, 6952–6958 (2016).

16. Spatafora-Salazar, A., Cunha, L. H. P. & Biswal, S. L. Periodic deformation of semiflexible colloidal chains in eccentric time-varying magnetic fields. *Journal of Physics: Condensed Matter* **34**, 184005 (2022).

17. Nishiguchi, D., Iwasawa, J., Jiang, H.-R. & Sano, M. Flagellar dynamics of chains of active Janus particles fueled by an AC electric field. *New J Phys* **20**, 015002 (2018).

18. Vutukuri, H. R. *et al.* Colloidal Analogues of Charged and Uncharged Polymer Chains with Tunable Stiffness. *Angewandte Chemie International Edition* **51**, 11249–11253 (2012).

19. Ma, H. & Suhling, J. C. A review of mechanical properties of lead-free solders for electronic packaging. *J Mater Sci* **44**, 1141–1158 (2009).

20. Lubliner, Jacob. *Plasticity Theory*. (Macmillan ; Collier Macmillan, 1990).

21. Chen, W. F. & Han, D. J. *Plasticity for Structural Engineers*. (Springer New York, New York, NY, 1988). doi:10.1007/978-1-4612-3864-5.

22. Jenq, S.-T., Chiu, Y.-S., Lin, R.-J. & Lai, Y.-S. The stress-strain relationship of Sn63Pb37 and SAC305 solder materials at elevated temperature condition. in *2010 5th International Microsystems Packaging Assembly and Circuits Technology Conference* 1–4 (IEEE, 2010). doi:10.1109/IMPACT.2010.5699529.

23. Plumbridge, W. J. & Gagg, C. R. Effects of strain rate and temperature on the stress–strain response of solder alloys. *Journal of Materials Science: Materials in Electronics* **10**, 461–468 (1999).

24. Qin, F., An, T. & Chen, N. Strain Rate Effects and Rate-Dependent Constitutive Models of Lead-Based and Lead-Free Solders. *J Appl Mech* **77**, (2010).

25. Harkavyi, Y., Giżyński, K. & Rozynek, Z. Experimental and FEM simulation study of compressive deformation of solder microballs and particle chains. *Soft Matter* **21**, 4393–4406 (2025).

26. Frederick, C. O. & Armstrong, P. J. A mathematical representation of the multiaxial Bauschinger effect. *Materials at High Temperatures* **24**, 1–26 (2007).

27. Chaboche, J. L. Constitutive equations for cyclic plasticity and cyclic viscoplasticity. *Int J Plast* **5**, 247–302 (1989).

28. Perzyna, P. Fundamental Problems in Viscoplasticity. in 243–377 (1966). doi:10.1016/S0065-2156(08)70009-7.

29. Norton, F. H. The creep of steel at high temperatures. *McGraw-Hill Book Company, Incorporated* **35**, (1929).

30. Miehe, C. A theory of large-strain isotropic thermoplasticity based on metric transformation tensors. *Archive of Applied Mechanics* **66**, 45–64 (1995).

31. R. J. Asaro and A. Needleman. Texture Development and Strain Hardening in Rate Dependent Polycrystals. *Acta Metallurgica* **33**, 923–953 (1985).

32. Gurson, A. L. Continuum Theory of Ductile Rupture by Void Nucleation and Growth: Part 1—Yield Criteria and Flow Rules for Porous Ductile Media. *J Eng Mater Technol* **99**, 2–15 (1977).

33. Needleman, A., Tvergaard, V. & Hutchinson, J. W. Void Growth in Plastic Solids. in *Topics in Fracture and Fatigue* 145–178 (Springer New York, New York, NY, 1992). doi:10.1007/978-1-4612-2934-6_4.

7. A series of manuscripts constituting dissertation

This section presents a series of manuscripts that together form a coherent body of research. Each manuscript represents a stage in the research process, where solving one problem led to new research questions, guiding the next phases of the study. The works are thematically and methodologically connected, enabling a comprehensive understanding of the entire research effort.

——Scientific Paper I——

Fabrication of 1D particle structures outside a liquid environment using electric and capillary interactions: From fundamentals to applications

Rozynek Z., Harkavyi Y., Giżyński K.

Materials & Design, Volume 223, November 2022, 111233

Materials & Design 223 (2022) 111233

Contents lists available at ScienceDirect

Materials & Design

journal homepage: www.elsevier.com/locate/matdes

Fabrication of 1D particle structures outside a liquid environment using electric and capillary interactions: From fundamentals to applications

Z. Rozynek [a,b,*], Y. Harkavyi [a], K. Giżyński [c]

[a] Faculty of Physics, Adam Mickiewicz University, Uniwersytetu Poznańskiego 2, 61-614 Poznań, Poland
[b] Department of Battery Technology, Institute for Energy Technology (IFE), Instituttveien 18, NO-2007 Kjeller, Norway
[c] Institute of Physical Chemistry, Polish Academy of Sciences, Kasprzaka 44/52, 01-224 Warsaw, Poland

HIGHLIGHTS

- We demonstrate an uncomplicated and easy to implement method for fabricating 1D microparticle structures outside liquid.
- Different types of microparticles can be assembled in seconds into long chains using an electrical field supported by capillary action.
- Capillary forces were found to help aligning particles and creating one particle–thick structures.
- A comparative study demonstrates that the process functions best in dispersing liquids with high viscosity and low ionic conductivity.
- The 1D structures produced with the new method can be used to create electrically conductive micropaths on a substrate.

GRAPHICAL ABSTRACT

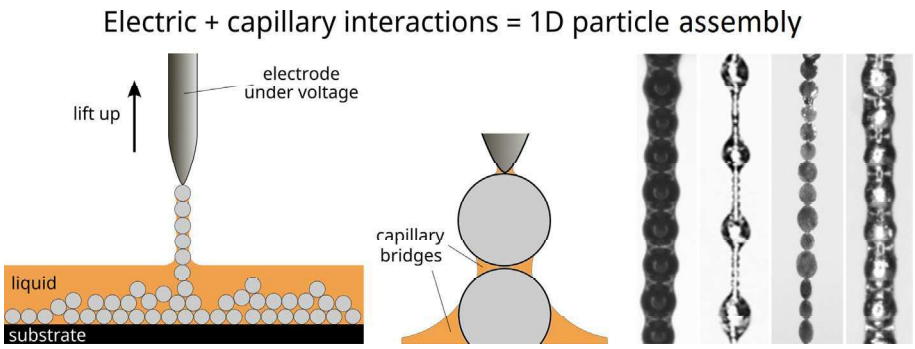

ARTICLE INFO

Article history:
Received 21 April 2022
Revised 3 October 2022
Accepted 4 October 2022
Available online 5 October 2022

Keywords:
1D structures
Particle chain
Beaded structure
Assembly
Capillary bridge
Electric tension
Conductive paths

ABSTRACT

Assembling microparticles into one-dimensional (1D) particle structures formed outside a liquid environment is challenging. This greatly hinders possible applications of such structures and the development of new materials. Herein, we demonstrate a simple, efficient, and easy-to-implement method for fabricating one particle–thick chain-like structures. Electrically conductive particles, initially dispersed in a nonpolar and weakly conductive liquid, are pulled out of the liquid using an electric field supported by capillary action. We study in detail how capillary and electric interactions, viscosity and ionic conductivity of the dispersing phase, particle shape, size and density, and pulling rate affect the general performance of our method. Our experimental results reveal that different types of microparticles can be assembled within seconds to form long chains. We found that capillary forces help aligning particles and creating single particle–resolution structures. The results show that dispersing liquids with large viscosity and low ionic conductivity are preferred as they reduce the negative effect of ionic screening. In the second part of our research, we investigate the physical properties of the produced beaded structures that we deem intriguing for both fundamental and applied research. We finally demonstrate that 1D particle structures can be used to design electrically conductive micropaths.

* Corresponding author at: Faculty of Physics, Adam Mickiewicz University, Uniwersytetu Poznańskiego 2, 61-614 Poznań, Poland.
E-mail address: zbiroz@amu.edu.pl (Z. Rozynek).

https://doi.org/10.1016/j.matdes.2022.111233
0264-1275/

1. Introduction

1D particle structures—their characterization, application, and assembly methods—have been extensively studied over the past few decades. Current research on particle assembly is thriving and largely attracting funding and industry attention worldwide. Low-dimensional particle structures are often considered superior to 2D and 3D assemblies in terms of the added value of the materials after their assembly [1]. The useful properties of 1D particle structures, such as high surface-to-volume ratio, long-range ordering, or periodicity at the mesoscale, can be utilized in a variety of applications, including optical [2–4], biosensing [5], and electronic applications [6–9]. However, the fabrication of 1D particle structures is typically more difficult than the formation of structures with higher dimensionality. There are several approaches for creating 1D particle structures on a substrate. These include magnetic [10,11] or electric field–assisted assembly [12–17], self-assembly on lithographically patterned substrates [18–24], capillary flow–assisted assembly [25,26], self-assembly in pipe-like flows [27], dip coating techniques [28], and acoustic field–controlled patterning [29]. However, it is much more challenging and laborious to create one particle–thick freestanding structures or particle strings formed in air. The limited number of methods available for this type of assembly include transfer printing [30,31], direct writing using liquid metals [32], mechanical manipulation with the use of microrobots, tapered fibers, microneedles connected with hydraulic micromanipulators [33–36], and optical tweezers [37]. These approaches are either expensive, time consuming, or inefficient (*e.g.*, only a limited number of particles can be manipulated in a single step and relatively short particle units can be built when using micromanipulators or optical tweezers). They may also require access to advanced tools and laboratories (*e.g.*, cleanrooms for producing templates or patterned substrates using electron beam lithography or photolithography). This hugely hinders the possible applicability of 1D particle microstructures and development of new materials and devices based on them.

In this study, we demonstrate a simple, efficient, and easy to implement method for fabricating single particle–thick chain-like structures outside a bulk liquid. The experiment can be set up by a nonspecialist in a few hours at a low cost (the budget version of the setup may cost less than a thousand dollars). As briefly communicated in our previous work, the method relies on electric and capillary interactions [38]. The concept of simultaneous usage of electric fields and surface tension is not new. It has been used to guide and concentrate DNA molecules [39], bundled carbon nanotubes [40–44], and silicon [45] or silicon carbide nanowires [46] onto electrode tips to form fibril structures for different applications. In these examples, the electric field was used to dielectrophoretically gather particles at a tip of an electrode, from which the particle structure started to grow, whereas capillary interactions ensured the fibrils had a small diameter. Despite researchers' efforts, a long one particle–thick structure could not be produced in any of the aforementioned works. In this study, we show how this can be achieved. We also provide new essential features of the electric approach for bottom-up assembly (communicated in ref. [38]), which greatly expand the state-of-the-art knowledge in this field. Various aspects of the presented fabricating route, including the role of particle size and shape, physicochemical parameters of the dispersion liquid (*e.g.*, viscosity and ionic conductivity), electric parameters (voltage, frequency), and the role of capillary interactions are here thoroughly studied.

Beaded particle structures have several characteristics that render them unique and useful in many applications. 1D micro and nanostructures that are flexible to a certain extent could find use in crack-free, inorganic coatings, wherein flexible particle wires can form self-assembled coatings that do not crack because of shrinkage in materials for soft robots and responsive matter [47], or in other mechanical applications, such as flexible artificial flagella or cilia [48–50]. Because the physical properties (*e.g.*, mechanical or electrical properties) of the produced beaded structures are intriguing for both fundamental research and applied research, we also design experiments for studying them. In the second part of the work, we present the study results on the macroscopic mechanical properties of freestanding particle chains and electrical properties of 1D particle assemblies deposited on a substrate. The latter can be used as a new type of conductive micropath in electronic applications.

The main outcome of the research is the development and description of uncomplicated and easy-to-implement electric method for fabricating one particle–thick chain-like structures. The results of this research will make the fabrication of 1D materials more efficient and accessible and will unlock the potential of the single particle–thick structures and their unique properties.

2. Methods

2.1. System configurations and experimental setup

The method for fabricating a long 1D particle structure presented here is robust, meaning that it works for various types of particles independently of their size, shape, and electrical properties. It enables formation of 1D structures regardless of the particle density (ρ_p) in relation to that of the surrounding liquid (ρ_l); see Fig. 1a,b.

The experimental setup used for the fabrication of 1D microstructures consisted of a signal generator (SDG1025, Siglent), high-voltage bipolar amplifier (10HVA24-BP1, HVP), digital microscope (AM7115, Dino-Lite), light source (KL 300 LED, Schott), PC for collecting images, and motorized stage (MT1-Z8, Thorlabs) for translating vertically (with a controlled speed) an electrode attached to it through an electrically nonconductive holder. A sample (a thin layer of particle dispersion) was dispensed on a substrate attached to an XY translation stage (LT3, Thorlabs). The stage was used to ease the sample positioning relative to the signal electrode. A schematic figure illustrating the experimental setup is shown Fig. 1c.

2.2. Materials and sample preparation.

Silicone oils (Rhodorsil Oils 47; with different viscosities in the range of 50–1000 cSt at 25 °C, density 0.96–0.97 g·cm^{-3} at 25 °C, electrical conductivity of 5–10 pS·m^{-1}, and relative permittivity ~ 2.8), castor oil (MA-220–1, Mareo, Poland; density of ~ 0.96 g·cm^{-3} at 25 °C, electrical conductivity of ~ 50–100 pS·m^{-1}, relative permittivity ~ 4.7, and kinematic viscosity of ~ 750 cSt at 25 °C), UV-curable epoxy (Formlabs, FLGPCL04; electrical conductivity ~ 100 pS·m^{-1}, relative permittivity ~ 2.7, density ~ 1.1 g·cm^{-3}, and viscosity ~ 2500 cSt, all measured at 25 °C), and liquid flux (TK83, ThermoPasty, Poland; with density 0.85 g·cm^{-3} at 25 °C) were used to form different dispersions with microparticles. We used several types of microparticles: conductive Ag-coated silica microspheres (from Cospheric LCC, USA; M-60-0.17, 55–63 μm; M-60-AG-0.20, 125–150 μm; and M-40-0.67, 10–20 μm, with specific density 0.17, 0.21, and 0.67 g·cm^{-3}, respectively); Ni-plated silica microspheres (from Cospheric LCC, USA; M-18-Ni-0.69, 5–30 μm, with density 0.69 g·cm^{-3}); Cu particles (provided by Prof. Piotr Garstecki from the Polish Academy of Sciences, Warsaw; 40–50 μm, with specific density 8.96 g·cm^{-3});

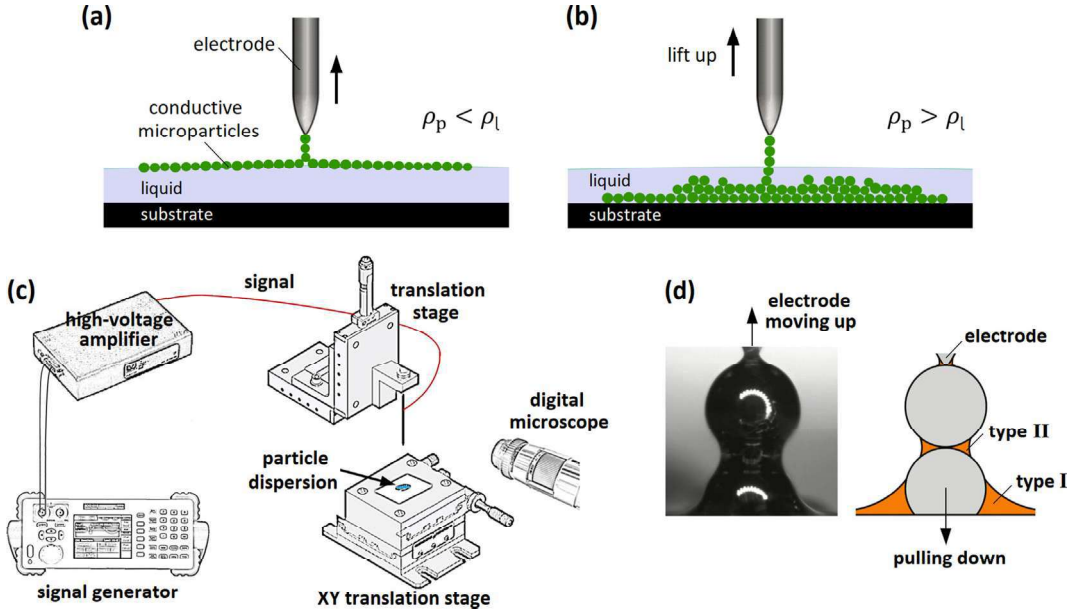

Fig. 1. (a) Lightweight particles float on the surface, and a particle chain is formed at the air–liquid interface. (b) Heavyweight particles sediment at the bottom of the liquid, and a particle chain is formed in the liquid phase. (c) Schematic figure illustrating part of the experimental setup. A high-voltage signal (red line) was provided to the needle-shaped electrode. (d) The image of two conductive particles aligned vertically along the direction of electrode lifting. The lower particle is being pulled out from the liquid. The upper particle is outside the bulk liquid and is in contact with the signal electrode. Two types of capillary liquid bridges are formed, which are well resolved in the image and depicted in the schematic drawing. The force stemming from the particle–planar liquid surface capillary bridge (type I) opposes the electric force by trying to pull the particle down to the bulk liquid (as indicated by the arrow). The particle–particle capillary bridges (type II) aid in stabilizing the chain and influence its mechanical properties. (For interpretation of the references to colour in this figure legend, the reader is referred to the web version of this article.)

solder particles (from IPS, France; $Sn_{96.5}Ag_3Cu_{0.5}$, 45–75 μm); weakly conductive polystyrene particles (from Microbeads AS, Norway; ~140 μm, with specific density of ~ 1.05 g·cm^{-3}, sulfonated for 32 min to increase their electrical conductivity from 10^{-10} to 10^{-7} S·m^{-1} measured at 1 kHz, as described in ref. [50]); stainless steel particles (from Cospheric LCC, USA; 23–28, 41–48, 95–105, and 190–220 μm, with specific density 7.8 g·cm^{-3}). Disc-shaped particles were made by mechanically compressing the solder particles. Hydrogel particles were made of agar powder (~5 wt%, 88588, Sigma-Aldrich) doped with iron nanoparticles (~5 wt%, 637106, Sigma-Aldrich).

3. Results and discussion

3.1. Fabrication of 1D particle structures

A schematic representation of a method for fabricating 1D particle structures is presented in Fig. 1a,b. A signal electrode (here a needle or a thin wire) is first brought close to the interface of a liquid or is dipped into the liquid. An electric voltage (U), applied through the signal electrode, polarizes the particles and attracts them toward the tip of the electrode. As the electrode rises, the particles are successively pulled out from the air–liquid interface on the condition that the strength of the electric force acting on the particle being pulled out from the interface is stronger than that of the force stemming from the capillary bridge (which tries to pull the particle back to the liquid). As the electrode is lifted higher, this particle–planar liquid surface capillary bridge (annotated as type I in Fig. 1d) extends and eventually undergoes a transition into the particle–particle liquid bridge (annotated as type II in Fig. 1d). Meanwhile, a new particle–planar liquid surface capillary bridge is formed at the particle below (see also Movie S1). Once the particle structure of the desired length is formed outside the bulk liquid, the electric tension can be turned off. The newly formed particle chain will remain stable owing to the capillary liquid bridges (type II) that provide attractive interactions between the neighboring particles. In the next section, we will discuss in greater detail the roles of each type of capillary liquid bridges in the 1D particle structure formation, stability, and mechanical properties.

In Fig. 2, we show experimental realizations of the electric route for fabricating 1D particle structures composed of light (floating) and heavy (sedimented) particles. The structures presented in Fig. 2a–e were assembled using a mixture of Ag-coated hollow silica microspheres (with diameter ~ 60 μm) in silicone oil (with viscosity ~ 100 mPa·s). Using a regular mechanical pipette, a few droplets of the mixture were deposited onto the substrate. Because the particle density was much lower than that of the silicone oil, the particles quickly moved upwards, forming a particle layer on the air–silicone oil interface. To initiate the formation of the 1D particle structure, we first lowered the signal electrode to approach the interface (Fig. 2a). Then, we applied an alternating current (AC) electric voltage (U = 500 V, f = 10 kHz, square wave). As a result, the microparticles were attracted to the electrode (Fig. 2b). As the electrode was elevated (with a rate of 0.2 mm·s^{-1}), particles—one after another—were successfully pulled out of the interface forming a structure resembling a beaded necklace (Fig. 2c–e). The particles were held via electrostatic forces and the capillary particle–particle liquid bridges formed by the silicone oil. The whole process is presented in Movie S2.

In the next experiment, we used stainless steel particles (with diameter ~ 100 μm) suspended in the same silicone oil. The suspension was poured into a small glass container. The heavyweight particles sedimented on the bottom of the container. To form 1D particle structures, we used the same electric conditions and similar pulling speeds as those in the first experiment. The particle chain was initiated in a liquid phase (Fig. 2g,h). After lifting the electrode, the particle chain grew as the sedimented particles kept being attracted to the chain's bottom end. Eventually, the structure transited through the air–liquid interface (Fig. 2i) and continued

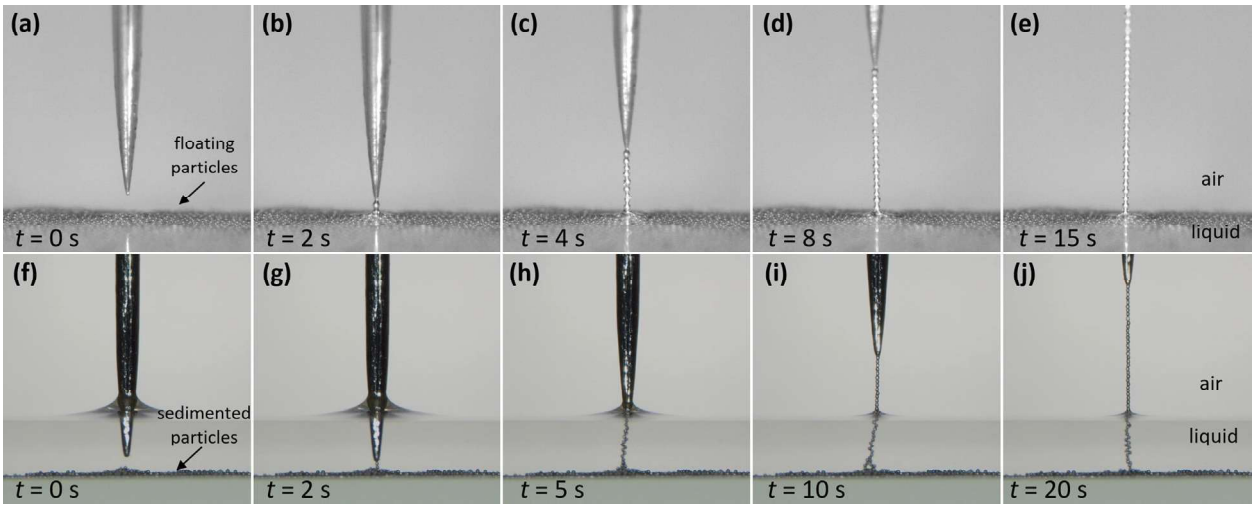

Fig. 2. Fabricating 1D particle structures outside bulk liquid—examples of experimental realization. Images from experiments on (a–e) Ag-coated hollow silica microspheres (size ~ 60 μm), and (f–j) stainless steel particles (size ~ 100 μm) being pulled out of the bulk liquid. In both cases, an AC electric voltage (U = 500 V, f = 10 kHz) was provided to the signal electrode. See also corresponding Movie S2 and Movie S3.

growing to form a 1D particle structure outside the bulk liquid (Fig. 2i,j). See also the corresponding Movie S3.

Fig. 3 summarizes the experimental observations of the 1D particle structure assembly. The electric route presented here enables the formation of long structures comprising hundreds of particles. In Fig. 3a, we show a nearly 3-cm long chain composed of around 600 Ag-coated silica microspheres (size ~ 60 μm) stabilized by silicone oil (viscosity ~ 500 mPa·s). Furthermore, the beaded chains can be made of different particle materials, for example, 100-μm stainless steel particles (Fig. 3b), ~55-μm solder particles (Fig. 3c), and other kinds of electrically conductive materials, such as solid particles of nickel, silver, and gold; or core–shell particles with a conductive shell. Interestingly, these particles can be dispersed in different nonpolar and weakly conductive liquids, such as natural or synthetic oils, liquid paraffin, UV-light curable epoxy (Fig. 3b), or liquid flux (Fig. 3c). We noted that the size polydispersity of particles practically does not affect the structure formation. In fact, we found that the method can be used for creating binary microstructures using a dispersion of two types of particles, *e.g.*, stainless steel particles measuring 45 and 200 μm (Fig. 3d). The particles should be conductive to make a long chain. However, short 1D structures (composed of several particles) can be formed using particles with electrical conductivities several orders of magnitude smaller than those of typical conductors. In Fig. 3e, we present a nearly 2-mm long structure formed outside bulk liquid. It comprises several 140-μm polystyrene particles with electrical conductivity of ~ 10^{-7} S/m (measured at 1 kHz). Apart from solid particles and microspheres, it is also possible to use conductive hydrogel microparticles. In Fig. 3f, we present a chain made of soft spheres composed of agar gel and iron nanoparticles. It is worth mentioning that the method also works for nonspherical particles, such as discs (Fig. 3g) or rods. However, these shapes

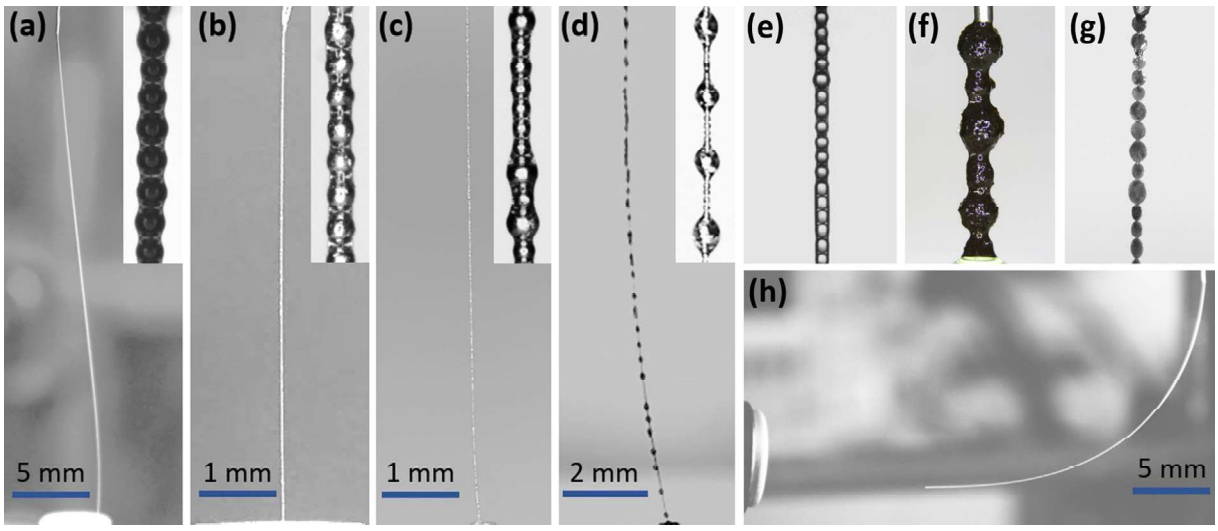

Fig. 3. Viability of the method. The electric method enables the fabrication of single-particle resolution structures made of different types of particles: (a) 60-μm Ag-coated silica, (b) 100-μm stainless steel, (c) $Sn_{96.5}Ag_3Cu_{0.5}$ solder with size 45–75 μm, (d) 45 and 200-μm stainless steel, (e) 140-μm polystyrene with increased electrical conductivity, (f) conductive hydrogel balls with sizes 300–600 μm, and (g) disc-shaped particles with an average diameter of 200 μm. Different liquids were used as dispersing phase, including (a,e,h) silicone oil, (b) UV-curable epoxy, (c) liquid flux, and (d,f,g) castor oil. All the presented structures were stable after turning off the electric tension. The beaded structures were flexible and could bend, as in the example shown in panel (h). See also corresponding Movie S4.

are not favorable because the electric interaction between such nonspherical particles objects is weak and only short structures composed of several particles can be created.

Finally, we observed that all the presented structures were stable after turning off the electric tension, *i.e.*, the particles remained in the chain held by the particle–particle capillary bridges. Interestingly, even small wind drafts in our laboratory did not damage the structures that fluttered and bent, as shown in Movie S4. Their flexibility is also revealed in Fig. 3h, where a long chain (still under the electric tension) bends toward the camera lens seeking the nearest electrical grounding.

3.2. Physics behind the method and its performance

The method relies on the interplay between electric force, gravitational force, and the force stemming from capillary interactions. Additionally, its performance depends on several parameters, such as the electric properties of particles and dispersing liquid, particle wettability, liquid viscosity, particle density, and pulling rate. We will first discuss the role of capillary bridges and the influence of the gravitational force.

3.2.1. Type I capillary bridge

As already noted, there are two types of liquid bridges in the system. The type I capillary bridge emerges upon pulling a particle out from the air–liquid interface, which creates a downward force (F_{sp}) that is the sum of capillary force, buoyancy force, and gravitational terms (hydrostatic pressure and particle weight). The magnitude of this force depends on the shape of the capillary bridge (defined by the particle position (h) in respect to the planar liquid interface; see schematic drawing in Fig. 4a), and its precise estimation is nontrivial and requires numerical calculations (see ref. [51]). Generally, when taking into account a spherical geometry of a particle and assuming that the dispersing liquid is perfectly wetting (justified for nonpolar liquids and various kinds of particles used in this study), the magnitude of F_{sp} scales as $\propto 2\pi R\gamma$ for $R \to 0$ and $\propto R^3$ for $R \to \infty$. Based on our previous theoretical work (ref. [51]), we estimated F_{sp} for two types of particles (light and heavy) with radii (R) between 1 μm and 4 mm, for a given liquid–gas surface tension ($\gamma = 20$ mN·m^{-1}). In Fig. 4a, we plot F_{sp} as a function of particle radius for two different particle densities (0.17 and 7.85 g·cm^{-3}).

From the plot in Fig. 4a, we learn that the gravitational terms are insignificant for a particle with a diameter below ~1 mm. Therefore, the particle density does not play a role for particles in the micrometer scale, *i.e.*, the magnitude of electric force (F_e) needed to pull out a particle (of radius R) from the air–liquid interface is the same independent of the particle density. For a microparticle with a radius ranging between 5 and 500 μm (typically used in this study), the electric force acting on the particle at the air–liquid interface needs to be in a range 10^{-3}–10^{-5}N.

The type I capillary bridge may be deemed an unfavorable physical phenomenon. However, this capillary liquid bridge plays an important role: it aids particle aligning and prevents particle grouping. As shown in Fig. 4b, conductive Ag-coated silica microparticles (sprinkled on a dry substrate) assemble irregularly and form agglomerates when the signal electrode is lifted (see also Fig. S1 and Movie S5). These unwanted features are greatly reduced by the action of the surface tension force. In the bottom panel of Fig. 4b, we demonstrate the formation of a straight, one particle–thick chain, made of the same Ag-coated silica microparticles, pulled out from silicone oil. Note that a chain formed originally with defects can be straightened when pulled through the interface due to the surface tension force (see Movie S6).

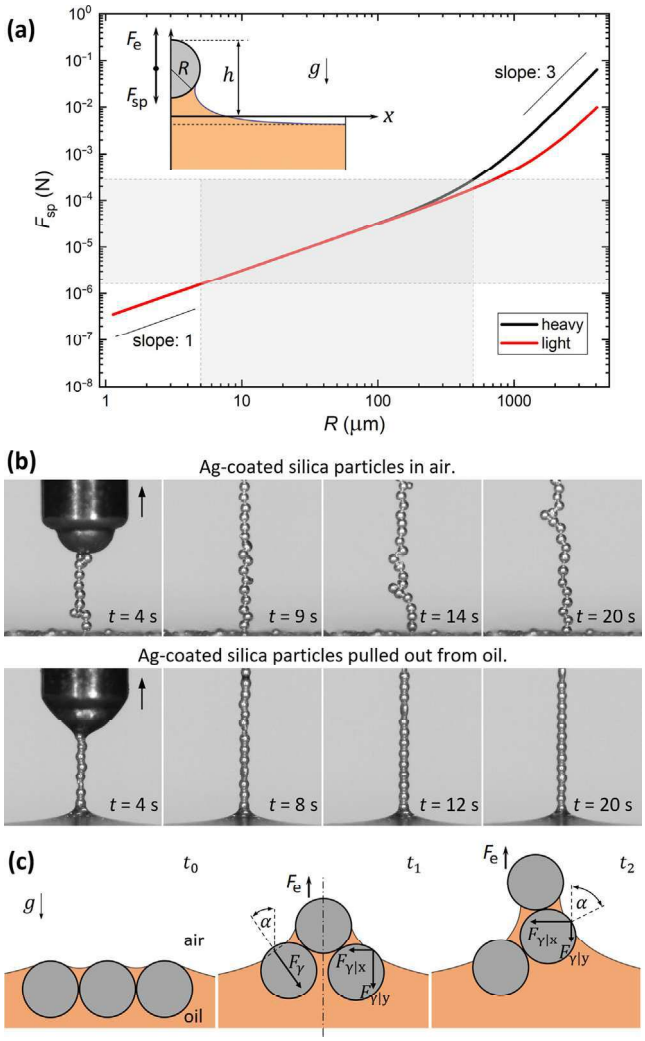

Fig. 4. (a) A log–log plot of F_{sp} as a function of the particle radius R calculated for two different particle densities (0.17 and 7.85 g·cm^{-3}) assuming $\gamma = 20$ mN·m^{-1}. The inset image is a schematic showing the shape of a sphere–planar liquid surface bridge, the direction of force stemming from that bridge (F_{sp}), and the direction of the electric force (F_e). The magnitude of F_{sp} is determined by this shape (assumed as cylindrically symmetric), which largely depends on the relative position h of the particle in respect to the planar–liquid interface. (b) Comparison of chain formation in the air (top row) and pulled out of the liquid (bottom row). Type I capillary bridges are visible at the bottom of the images for the latter case. The electrode was moved upward, as indicated by the arrows. (c) Surface tension helps aligning particles during the formation of a 1D particle structure. At t_0, the particles float at the air–oil interface. Once the middle particle is lifted (by the action of the electric force), the conformation of particles changes and so does the shape of the interface affecting the values of α. This, in turn, influences the magnitude of the components of capillary force, promoting particle alignment in a vertical direction.

As illustrated in Fig. 4c (showing simplified two-dimensional sketch), the capillary force acting on a (second/third) particle can be decomposed into the y component that pushes the particle downward in the direction of gravity $F_{\gamma|y} \sim 2\pi R\gamma \cos\alpha$ and an axial force acting to push the particle sideway just under the above located particle: $F_{\gamma|x} \sim 2\pi R\gamma \sin\alpha$. The angle α comes from the inclination of the air–liquid interface. From the experimental images, we estimated that α changes from nearly 0 to around 75°, indicating that the x component of the capillary force is significant and may indeed play a role in the vertical alignment of particles and the formation of a single particle–thick microstructure. This capillary effect is particularly appreciable for particles with small mass and density for which the gravitational force is too

small to straighten the particle chain (and prevent particle agglomeration).

3.2.2. Type II capillary bridge

When pulling a particle chain out of the liquid, the particle–planar liquid surface capillary bridge (type I) undergoes a transition into the particle–particle liquid bridge (type II).

As described in ref. [51], the capillary bridge transformation can be smooth and continuous or discontinuous (as in Movie S1) depending on the particle diameter. Yet, the character of this transformation does not seem to influence the creation of the 1D particle structure outside the suspension. Remarkably, the presence of the type II capillary bridges makes it possible to reliably hold the formed particle chain even after the electric tension is turned off. This is possible only when the force stemming from the single particle–particle capillary bridge (F_{pp}) is greater than the weight of the chain formed below that bridge. This sets the limit for the maximum number of the particles comprising the particle chain and ultimately defines its maximum length (in the absence of electric force). In Table 1 we present calculations of the maximum number of particles constituting the chain and the chain length for particles with different radii (10–1000 μm) and densities (0.17 and 7.85 g·cm^{-3}). In our calculations, we included the weight of the liquid forming the capillary bridges, assuming the volume of a single bridge is equal to a quarter of the volume of a particle. The liquid density is 1 g·cm^{-3}, and the surface tension $\gamma = 20$ mN·m^{-1}.

From the theoretical calculations, we see that several cm-long 1D particle structures comprising of thousands of particles would remain stable in the absence of the external field. This is, indeed, what we found experimentally. We were able to form a 20-cm long chain made of thousands of Ag-coated hollow silica spheres ($R \sim 30$ μm and $\rho_p = 0.17$ g·cm^{-3}) and a 2-cm chain made of hundreds of steel particles ($R \sim 22$ μm and $\rho_p = 7.85$ g·cm^{-3}).

3.2.3. Pulling rate

As mentioned above, in our calculations we assumed that the volume of a single interparticle bridge is $V_b = V_p/4$. However, the amount of liquid dragged during the particle pulling depends on the pulling speed (v) and liquid's viscosity (η). An example is shown in Fig. 5a, where a chain of particles with a size of ~500 μm is pulled out from a liquid with pulling rates ranging from 0.02 to 1 mm·s^{-1} (gray circles with a yellow rim are added to mark the position of the particles; the black part is the photographed liquid capillary bridge). From an investigation employing particles with radii in the range of 20–500 μm dispersed in silicone oil with viscosities in the range of 10–1000 mPa·s, we find that $V_b \to 0.05\ V_p$ for $(v \cdot \eta)/R < 0.01$ Pa and $V_b > V_p$ for $(v \cdot \eta)/R > 1$ Pa. As presented in Fig. 5b, the magnitude of F_{pp} (stemming from the particle–particle capillary bridge) decreases when V_b increases. Therefore, the maximum length of a freestanding particle chain (attached to the electrode) is determined by the pulling rate.

Moreover, we observe that the liquid bridges stabilize the 1D particle structure when $(v \cdot \eta)/R < 1$ Pa, that is, when $V_b > V_p$. Otherwise, surface tension may cause the particle chain to curl up after removing the electric force (see Fig. 5c). This principle provides a rough estimation of the maximum pulling speed, at which the particle chain can be formed outside the bulk liquid and remains stable in absence of the external force. For instance, for spheres with a radius of $R = 50$ μm dispersed in silicone oil of viscosity $\eta = 50$ mPa·s^{-1}, the maximum pulling speed is approximately 1 mm·s^{-1}; a 1D particle structure with a length of ~1 cm can be formed in just a few seconds. The maximum pulling speed needs to be considered if the electric tension needs to be turned off for any postprocessing work on the assembled structure, unless it is permanently locked (*e.g.*, by hardening of the liquid constituting the capillary bridges) before switching off the electric tension.

3.2.4. Electric effects

As sketched in Fig. 1a,b, the substrate is ungrounded and the direct-current flow is restricted. Thus, the electric circuit can be simplified to the *RC*-circuit, which has two passive components of a resistor (R) and capacitor (C). In such a case, a frequency dependency on the minimal electric voltage (U_{min}) required to pull a particle out from the liquid interface should be expected. We conducted an experiment in which we used Ag-coated hollow silica microspheres (with a density of 0.17 g·cm^{-3}) and investigated U_{min} as a function of its frequency (f). Additionally, we tested the influence of liquid viscosity (ranging from 10 to 1000 mPa·s) on the value of U_{min}. The experimental results shown in Fig. 6a indicate that for high frequencies (f) of the alternating electric field, U_{min} is both viscosity- and frequency-independent, reaching a constant value of around 100 V.

We accept that the following parameters, namely the surface tension (γ), dielectric constants ($\varepsilon_p, \varepsilon_{oil}$), and electrical conductivities (σ_p, σ_{oil}) of the particle and liquid remain constant within the tested frequency range (10–5000 Hz). Such frequency dependence on the electric tension can be understood by a simple analogy to an RC circuit, with the substrate acting as a capacitor. Assume that we apply an AC voltage drop $U(t) = U \cdot \cos(2\pi \cdot f \cdot t)$ to the system. The voltage drops across the capacitor and the resistor, $U_C(t)$ and $U_R(t)$, obey the relations $U_C(t) + U_R(t) = U(t)$, and since $i(t) = R \cdot U_R(t) = C\frac{d}{dt}U_C(t)$, it gives $U_R(t) = RC\frac{d}{dt}U_C(t)$. A Fourier transform yields $\tilde{U}_R(f) = \mathrm{i}2\pi f \cdot RC \cdot \tilde{U}_C(f)$. Given the RC charging frequency $1/f_c = 2\pi RC$, we can derive the voltage drop on a resistor as follows: $\tilde{U}_R(f) = \frac{\mathrm{i}f/f_c}{1+\mathrm{i}f/f_c}U$. To pull a 1D particle structure out of the silicone oil, we need a sufficiently large electric force between spheres, which is determined by the magnitude of the voltage drop $\left|\tilde{U}_R(f)\right|$. Considering $\tilde{U}_R(f) = U/\sqrt{1+(f_c/f)^2}$, the threshold in the total applied electric tension U should then be: $U_{min} \propto \sqrt{1+(f_c/f)^2}$. This is consistent with the experimental observation, that is, at high frequency, the threshold voltage U is independent of the field frequency; however, at a low frequency, U_{min} is nearly inversely linear with f.

3.2.5. Dispersing liquid viscosity and its ionic conductivity

The results in Fig. 6a also show that for each oil viscosity value, there is a different threshold frequency (f_{th}), below which the value of U_{min} increases. We collapsed the data presented in Fig. 6a by multiplying each curve by its corresponding viscosity value (see Fig. 6b). The data collapsed reasonably well, indicating

Table 1
Calculated maximum number of particles making up the chain and the chain's length for particles of different radii (R) and densities (ρ_p).

R[μm]	10	20	50	100	200	500	1000
no. particles ($\rho_p = 7.85$ g·cm^{-3})	~4×10^3	~1×10^3	~150	~40	~10	~1	0
length$_{max}$ [cm]	~4	~2	~0.75	~0.4	~0.2	~0.05	–
no. particles ($\rho_p = 0.17$ g·cm^{-3})	~7×10^4	~2×10^4	~3×10^3	~700	~200	~30	7
length$_{max}$ [cm]	~70	~40	~15	~7	~4	~1.5	0.7

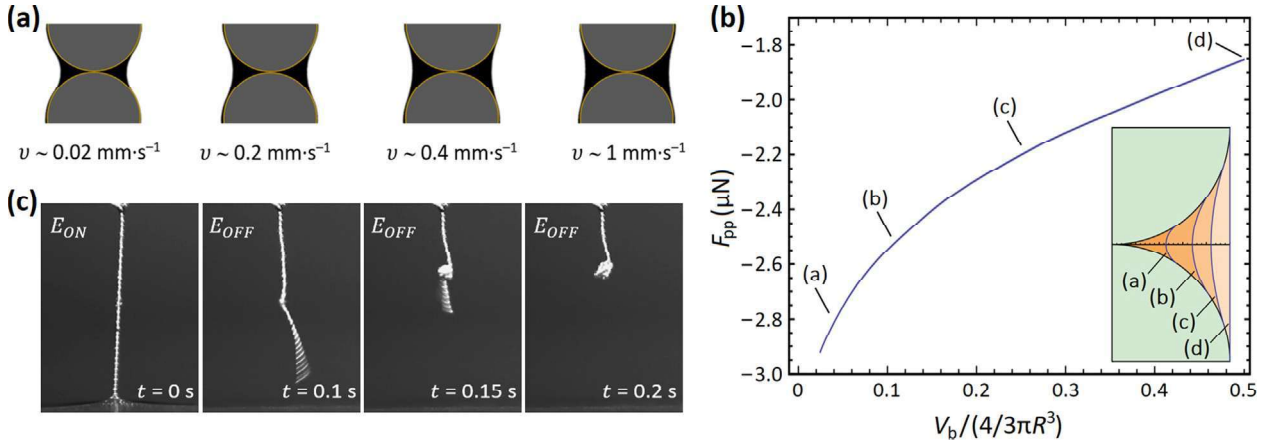

Fig. 5. (a) Stainless steel particles (size of ~500 μm) pulled out from silicone oil (~100 cSt) with different pulling rates 0.02–1 mm·s^{-1}. The amount of liquid dragged during the particle pulling depends on the pulling speed (and the liquid's viscosity). (b) The magnitude of the force F_{pp} plotted against the dimensionless volume of the particle–particle capillary liquid bridge. The calculations were performed for particles with $R = 25$ μm and $\gamma = 20$ mN·m^{-1}. Note that the plot starts from $V_b/V_p = 0.02$, as the lower values would not be physical, *i.e.*, for the given surface tension and the atmospheric pressure, it is not possible to form a bridge with $V_b/V_p < 0.02$ even if the pulling rate would go to zero. The inset image shows schematically-four examples of different shapes of the capillary liquid bridge with their corresponding dimensionless volumes V_b/V_p. (c) A particle chain made of Ag-coated silica microspheres (~60 μm) pulled out from silicone oil at 1 mm·s^{-1}. Due to the surface tension of the liquid (with $V_b > V_p$), the chain curls up after the electric tension is turned off.

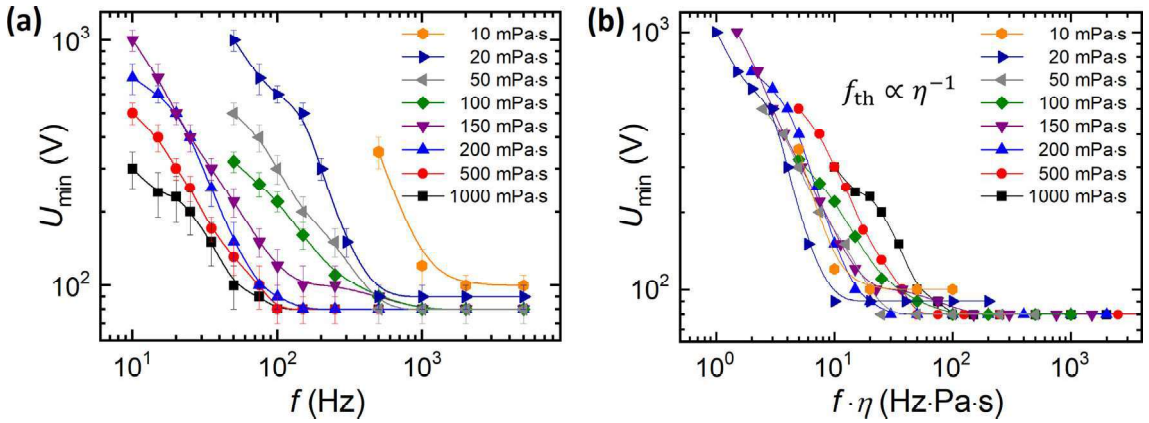

Fig. 6. Minimum electric tension required for pulling a particle out from the interface. (a) Below a threshold frequency, U_{min} is f-dependent, whereas at high frequencies, U_{min} reaches a constant value of around 100 V. (b) The collapsed data reveal scaling of the threshold frequency (*i.e.*, $f_{th} \propto \eta^{-1}$).

that $f_{th} \propto \eta^{-1}$ (see also Fig. S2, where we plot f_{th} vs η). This transition frequency f_c can be associated with the electrostatic screening of the electric field by ions (impurities) present in the oils. For the oils in the viscosity range studied here (*i.e.*, 10–1000 mPa·s), the ionic diffusivity is inversely proportional to viscosity [52]. This may explain the shift of the threshold frequency toward higher frequency values for the oils with smaller viscosities featuring greater ionic diffusivity.

Furthermore, to investigate the influence of ions, we conducted an experiment using both pure and modified silicone oils (with viscosity $\eta = 350$ mPa·s). The latter possesses an increased concentration of mobile ions, increasing the ionic conductivity, provided from a dissolved quaternary ammonium salt. As shown in Fig. S3, the addition of ions affects the $U_{min}(f)$ curve by shifting it toward higher frequency values, which is consistent with the abovementioned results.

Generally, we observed that the proposed electric method for fabricating 1D particle structures outside the bulk liquid works better for dispersing liquids with viscosities much larger than that of water and with ionic conductivity lower than around 10^{-9} S·m^{-1}. Otherwise, a frequency greater than 10 kHz must be used to suppress the unfavorable effect of electrostatic screening. Increasing the magnitude of electric tension may also help by generating stronger electric force between particles. However, it leads to increased electric current flowing through the particle chain, which could be ultimately destructive. We noted that the heat generated by the high current flow caused the degradation of the fluid and/or damaged the hollow particles with thin shells, thus preventing the formation of a long and stable particle chain.

3.3. Toward applications

The assembly method we describe here is simple, efficient, and easy to implement. As mentioned in the Introduction, the experimental setup can be assembled within hours and is inexpensive (starting from around $1000). The formation of 1D particle structures can be parallelized if needed, enabling simultaneous assembly of dozens of chains. As demonstrated in the previous section (see Fig. 3), the particle structures can be designed to be several centimeters long and composed of thousands of particles. Such a low-cost and relatively efficient method should find use in different applications. Therefore, our method could lead to new approaches of organizing particles that could be utilized in both fundamental studies and applied research. In this section, we

demonstrate two application examples of the method. We will begin with presenting the formation of particle chains for studying their intrinsic mechanical and electric properties.

3.3.1. Fabricating particle chains to study their mechanical properties

There are several research studies on the mechanical properties of locked/fused granular and colloidal chains in the absence of external fields, where researchers investigated their elasticity, flexibility, or stretchability [16,53]. These mechanical properties are often attributed to the intrinsic properties of the locking material, such as grafted DNA [54,55] or polymer crosslinkers [56], that forms flexible joints connecting rigid micro or nanoparticles. Unfortunately, very little is known about the mechanical properties of capillary bridges–joint particle assemblies forming 1D particle structures. In particular, the literature lacks studies on the mechanical properties of such systems produced outside a bulk liquid and subjected to electric tension. The reason for this could be the difficulty in producing such single particle–resolution structures.

Here, we present the preliminary results of our ongoing project, in which we investigate the mechanics of a freestanding particle structure and study in detail the role of particle size, liquid viscosity, and dielectric properties, as well as the magnitude of the electric tension on the mechanical parameters of a particle chain. In the first example, we fabricated a short (~3 mm) particle chain made of stainless steel particles (~100 μm). One of its ends was attached to a pointy piece of a nonconductive substrate. The substrate was placed on a mechanical stage that moved vertically. By moving the substrate up and down we could change the mechanical compressive force acting on the chain. We varied the strength of the electric tension (100–450 V) applied to the electrode and studied qualitatively how the compressive mechanical stress is absorbed by the particle chain. As presented in Fig. 7a–e, the bending stiffness increases as the electric tension increases. It is interesting to see that at low electric tensions, the mechanical stress absorption is through particle structure buckling (see panels a,b). In contrast, at high electric tensions, the particle chain bends (see panels d,e).

To gain a deeper insight into the particle chain stability, we performed additional experiments on its mechanical properties. We formed a chain that spanned between a static electrode and an electrode that could rapidly translate in the vertical direction, normal to the gravity direction (see Fig. 7f). By moving the electrode by ~ 0.25 mm (the initial position of the electrode is indicated by the shaded image in the top panel of Fig. 7f), we created a downward motion to form a transverse wave propagating along the particle chain. The propagation velocity of the wave was recorded using a high-speed camera replacing the digital microscope (shown in Fig. 1c). We extracted four images (see Fig. 7f) from the movies to estimate the magnitudes of wave propagation velocities. We repeated the experiment for different magnitudes of electric voltage (between around 20 and 400 V) and estimated the wave propagation velocity. The results are plotted in the Fig. 7g. The velocity of the wave propagation v, the tension $F_T \propto v^2$ along the particle chain, and the bending stiffness $K \propto F_T$, all sharply increase with the magnitude of the electric tension above 100 V, making the 1D particle structure less flexible. The experimental data points were fitted to the formula $v = C_1 + C_2 \cdot U^2$, where the first term is the contribution from the capillary interactions and the second term describes the electric relationship. The fitting curve captures the trend relatively well, although more quantitative data is needed to be conclusive on the role of the electric tension on the mechanics of the particle chain. Nevertheless, we demonstrated that the electric method can easily produce a particle chain outside the bulk liquid and that the chain's mechanical properties could be studied to enhance the fundamental knowledge.

3.3.2. Formation of conductive micropaths and studies of their electric properties

Regarding the electronic properties of 1D particle microstructures, if the neighboring particles in the 1D particle structures are physically connected and the electrical resistivity is kept as low as in the bulk particle material, it should make them excellent candidates for conductive paths that are far cheaper than the

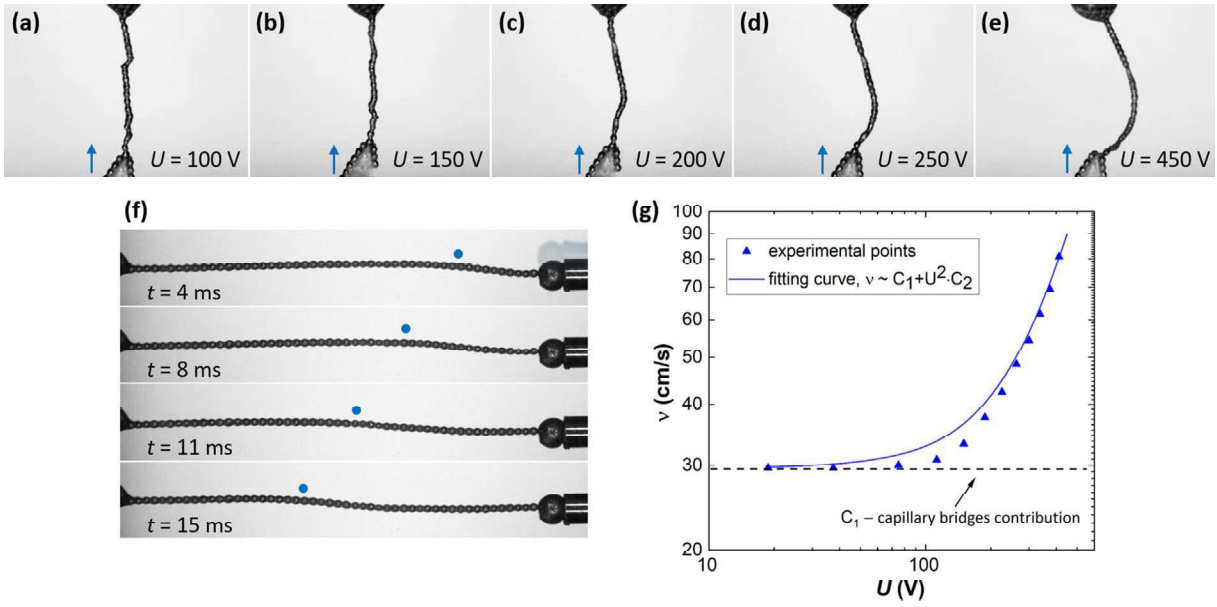

Fig. 7. Mechanical properties of a particle chain under electric tension. (a–e) Buckling to bending transition of the 1D particle structures under mechanical compression observed at increased electric tension. A pointy piece of a nonconductive substrate (to which a bottom end of the chain was attached) was moved up and down to change the mechanical compressive force acting on the chain. (f) Images of a particle chain made of stainless steel particles (~100 μm) captured at different times show the propagation of a transverse wave. The front of the wave is marked with a dot. (g) The velocity of wave propagation (v) plotted against the applied electric tension (U). See also corresponding Movie S7 and Movie S8.

conventionally used materials (nanoparticles or liquid metals). As a result, such particle structures could be used for various electronic applications. In the following example, we show how to deposit particles on a substrate to form conductive micropaths.

First, we produced a long particle chain composed of hundreds of solder balls (~200 μm) initially dispersed in a liquid flux. Then, the particles were deposited on a glass substrate by simultaneously translating the substrate and lowering the electrode to which the particle chain was attached (see Fig. 8a). The final shape of the deposited particle structure is governed by the motion of the substrate. As presented in Fig. 8a, a simple linear pattern was made in around 10 s.

The as-deposited micropath was poorly conductive owing to the small contact area between particles. Therefore, a postprocessing step is required to improve the electrical conductance. The conductance can be increased through heat or pressure sintering leading to the formation of a solid mass of material or by other means. Here, we demonstrate that mechanical compression can be used to increase the contact area, and thus the conductance of the particle chain. In Fig. 8b, we show three images (taken from above in direction along the compressive force) of 250-μm solder particles compressed by 6 %, 21 %, and 45 %. The particle chain was deposited on a carrier with two gold pads designed for impedance measurements (see Fig. S4) so that we could simultaneously measure the resistance of the chain and study the shape of the compressed particles. In Fig. 8c, we present COMSOL results of the simulated shape changes of the compressed solder balls, with the blue area denoting the contact area between neighboring balls. In Fig. 8d, we plot (dashed curve) the theoretically estimated (based on COMSOL results) values of resistance of 250-μm solder balls forming a conductive path between 1.6-mm distanced electrical contacts and compare them with the experimental results (red circles). The results show that the theoretical and experimental data match qualitatively although the experimental values are consistently smaller. With our ongoing research project, we hope to find out the reason for this discrepancy. Nevertheless, it is interesting to note that even a small deformation of a few % leads to a reduction in resistance by several order of magnitudes. Eventually, with a further compression, the resistance becomes very low, reaching a range of mΩ.

4. Discussion and conclusions

Within this work, we developed and explored the electric method for efficient formation of 1D particle structures. We studied in detail the influence of different parameters (such as electric field tension, size and shape of particles, viscosity, and ionic conductivity of the medium liquid) on the assembly process and the stability of the final particle chain.

Particles: Our results reveal that different types of microparticles (solid, core–shell, and soft particles) of any density can be assembled within seconds to form long chains. The particles should preferably be highly conductive to make a long chain, otherwise the voltage drop along the particle chain results in fast weakening of the electric force along the particle structure. Although, it was possible to form 1D structures using disc- or rod-shaped particles, the preferred shape is spherical. This is because the electric and capillary interactions between particles are much stronger for spherical particles. The spherical particles studied here had radii in the range of 20–500 μm. We failed to form long particle chains using particles larger than 500 μm. This is due to the increased significance of the gravitational force (see Table 1). In regard to the smallest particle size, in principle, it should be possible to go down

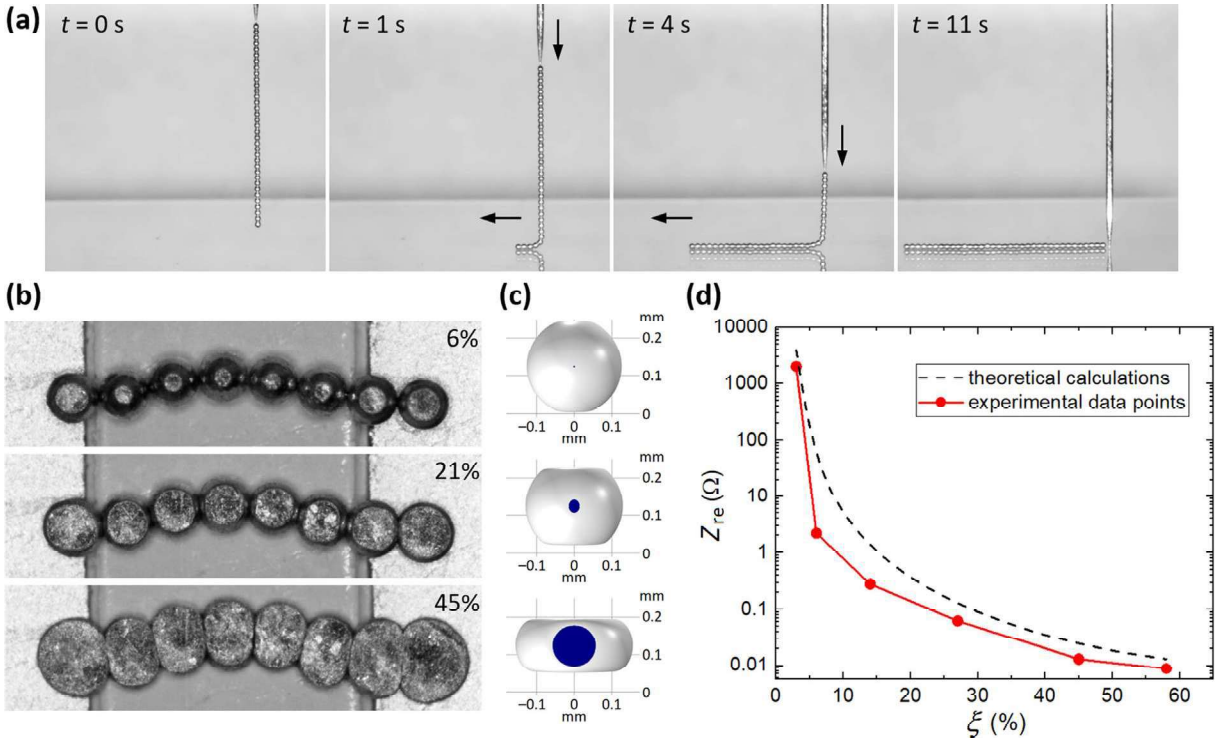

Fig. 8. (a) Solder particle chain (length of 0.74 mm) formed in air is deposited on a glass substrate by simultaneously translating the substrate and lowering the electrode. (b) Solder particles (size of 250-μm) deposited on a holder with two gold pads for impedance measurements. The chain was compressed by 6 %, 21 % and 45 % in direction along the viewing direction. (c) COMSOL simulated shapes of compressed solder balls with blue area denoting the contact area between neighboring balls. The degrees of the compression correspond to those from the experiment shown in panel b. (d) Experimental data and theoretically estimated values of the resistance (Z_{re}) plotted against the degree of compression (ξ). (For interpretation of the references to colour in this figure legend, the reader is referred to the web version of this article.)

below 1 μm. We attempted to form chains using spherical particles with radii of around 8 μm. However, the success rate was low and only short (several particle long) chains could be formed. Those small particles agglomerated more readily than larger particles of the same material, preventing successful formation of 1D structures outside liquid. Thin 1D particle structures (below 20 μm) are fragile and more prone to breaking. Therefore, stable experimental conditions are required, *i.e.*, eliminating micro vibrations of the experimental setup, wind draft in the lab, etc. It is worth mentioning that unlike in the methods described in ref. [54–58], the particles need no special pretreatment (functionalization) to form a stable 1D structure after the process of their formation is finished. The stability of the structure is attributed to the attractive interactions of capillary liquid bridges formed between neighboring particles.

Liquids: We showed that different types of dispersing liquids can be used. This ability to combine different particles with different liquids has practical relevance. For example, the liquid flux coats solder particles preventing the formation of an undesired passivation layer on the particle's surface and may promote particle sintering (if the 1D solder particle structure is to be used, for example, for electronic applications). On the other hand, the UV-hardened epoxy or paraffin wax may influence the particle chain flexibility. It can be also used to permanently lock particles (see Fig. S5) and form 1D, out-of-plane structures to be used, for example, as simple artificial cilia or cantilever arrays for robotics or sensors. Our experimental results reveal that liquids with large viscosity and low ionic conductivity are preferred as they reduce the negative effect of ionic screening, affecting the strength and frequency of the applied electric tension.

1D structure: We found that capillary forces help aligning particles and create one particle–thick structures preventing agglomerate formation. Additionally, we estimated the optimal pulling conditions to form a 1D particle structure that remains stable after turning off the electric tension. The maximum pulling velocity is primarily determined by the particle size and liquid viscosity. Interestingly, as shown in Fig. 3d, a binary microstructure can be formed using a dispersion of two types of particles having different size. Such structures may be desired, for example, for creating particle-based superstructures [59]. We also took advantage of the possibility of creating freestanding 1D structures to investigate their mechanical properties. The results indicate that the mechanical properties, including the stiffness of the primary 1D structure, are greatly affected by the strength of electric tension in a nontrivial fashion. This has not been studied before. Therefore, we are now running a follow-up project to understand in detail the influence of electric potential on the mechanics of one particle–thick assemblies aiming to generate new knowledge in this research area. Another thing to note is that high electric tensions may lead to formation of agglomerated rather than one particle–thick structures (see ref. [50]).

Example of applications: We also investigated possibilities of future application of beaded chains, including formation of conductive pathways on substrates for use in a variety of electronic applications. We are aware that the scheme presented in Fig. 8a–c may be impractical, especially in the industry settings. Still, the experimental results show the feasibility of the concept of using electric and capillary interactions for creating one particle–thick micropaths. This, in turn, stimulated us to explore the possibility of simultaneous formation of particle chains and their alignment on a substrate, which will ultimately enable the deposition of thousands of microparticles per second in a continuous manner [60]. We, therefore, foresee the method (which relies on the interplay between electric force, gravitational force, and the force stemming from capillary interactions) to be potentially useful in the display sector (open defect repair technology, fabrication of transparent conductive films), smart glass industry, security printing, and more.

Author contributions

Z. Rozynek initiated the project, formulated the scientific hypotheses, co-designed all experiments, and performed the experiments with results presented in Figs. 3a,d,e,h, Figs. 4a,c, Fig. 5, Fig. 6, Figs. 7a–e,g, Fig. S1a, Fig. S1b, Fig. S2, Fig. S3 and Fig. S5. Y. Harkavyi co-designed and performed experiments with results shown in Fig. 2, Fig. 3b,c,f,g, Fig. 4b, Fig. 8a,b, Fig. S1c, and Fig. S4. K. Giżyński co-designed and performed the experiments with results presented in Fig. 8c,d. Z. Rozynek wrote the first version of the manuscript. All authors took part in discussions toward the finalization of the manuscript. Z. Rozynek administered the submission and the review process.

Data availability

No data was used for the research described in the article.

Declaration of Competing Interest

The authors declare that they have no known competing financial interests or personal relationships that could have appeared to influence the work reported in this paper.

Acknowledgements

This research was funded by the Polish National Science Centre through OPUS (Grant No. 2019/33/B/ST5/00935) and SONATA (Grant No. 2019/35/D/ST5/03613) programs. We wish to thank Dr. A. Magdziarz, the owner of the company CADENAS in Poland, for giving us access to the company's research infrastructure and for providing materials. We also thank K. Kacprzak who performed some of the preliminary experiments that led to creation of Fig. 6, T. Kubiak who performed some of the preliminary experiments that led to creation of Fig. 7f, and Dr. F. Dutka for his help in calculating the capillary interactions (results presented in Fig. 4a and Fig. 5b).

Appendix A. Supplementary material

Supplementary data to this article can be found online at https://doi.org/10.1016/j.matdes.2022.111233.

References

[1] O.D. Velev, S. Gupta, Materials Fabricated by Micro- and Nanoparticle Assembly – The Challenging Path from Science to Engineering, Adv. Mater. 21 (19) (2009) 1897–1905.
[2] K.W. Allen, A. Darafsheh, F. Abolmaali, N. Mojaverian, N.I. Limberopoulos, A. Lupu, V.N. Astratov, Microsphere-chain waveguides: Focusing and transport properties, Appl. Phys. Lett. 105 (2) (2014) 021112.
[3] T. Mitsui, T. Onodera, Y. Wakayama, T. Hayashi, N. Ikeda, Y. Sugimoto, T. Takamasu, H. Oikawa, Influence of micro-joints formed between spheres in coupled-resonator optical waveguide, Opt. Express 19 (22) (2011) 22258–22267.
[4] W. Ahn, X. Zhao, Y. Hong, B.M. Reinhard, Low-Power Light Guiding and Localization in Optoplasmonic Chains Obtained by Directed Self-Assembly, Sci. Rep. 6 (1) (2016).
[5] M. Gao, M. Kuang, L. Li, M. Liu, L. Wang, Y. Song, Printing 1D Assembly Array of Single Particle Resolution for Magnetosensing, Small 14 (19) (2018) 1800117.
[6] K. Xu, L. Qin, J.R. Heath, The crossover from two dimensions to one dimension in granular electronic materials, Nat. Nanotechnol. 4 (6) (2009) 368–372.
[7] T. Ludtke, P. Mirovsky, R. Huther, L. Gover, G.H. Bauer, J. Parisi, R.J. Haug, Transport in nanoparticle chains influenced by reordering, Phys. Lett. A 375 (20) (2011) 2079–2081.
[8] M. Su, F. Li, S. Chen, Z. Huang, M. Qin, W. Li, X. Zhang, Y. Song, Nanoparticle Based Curve Arrays for Multirecognition Flexible Electronics, Adv. Matter. 28 (7) (2016) 1369–1374.
[9] A. Hubler, C. Stephenson, D. Lyon, R. Swindeman, Fabrication and Programming of Large Physically Evolving Networks, Complexity 16 (5) (2011) 7–8.

[10] X.Y. Jiang, J.G. Feng, L. Huang, Y.C. Wu, B. Su, W.S. Yang, L.Q. Mai, L. Jiang, Bioinspired 1D Superparamagnetic Magnetite Arrays with Magnetic Field Perception, Adv. Matter. 28 (32) (2016) 6952–6958.
[11] A. Spatafora-Salazar, L.H.P. Cunha, S.L. Biswal, Periodic deformation of semiflexible colloidal chains in eccentric time-varying magnetic fields, J. Phys.: Condensed Matter. 34 (18) (2022) 184005.
[12] D. Nishiguchi, J. Iwasawa, H.R. Jiang, M. Sano, Flagellar dynamics of chains of active Janus particles fueled by an AC electric field, New J. Phys. 20 (2018) 015002.
[13] S. Gangwal, A. Pawar, I. Kretzschmar, O.D. Velev, Programmed assembly of metallodielectric patchy particles in external AC electric fields, Soft Matter 6 (7) (2010) 1413–1418.
[14] S. Gupta, R.G. Alargova, P.K. Kilpatrick, O.D. Velev, On-chip electric field driven assembly of biocomposites from live cells and functionalized particles, Soft Matter 4 (4) (2008) 726–730.
[15] B. Bharti, G.H. Findenegg, O.D. Velev, Co-Assembly of Oppositely Charged Particles into Linear Clusters and Chains of Controllable Length, Sci. Rep. 2 (1004) (2012) 1–5.
[16] H.R. Vutukuri, A.F. Demirors, B. Peng, P.D.J. van Oostrum, A. Imhof, A. van Blaaderen, Colloidal Analogues of Charged and Uncharged Polymer Chains with Tunable Stiffness, Angew. Chem. Int. 51 (45) (2012) 11249–11253.
[17] Z. Wang, Z. Wang, J. Li, Y. Wang, Directional and Reconfigurable Assembly of Metallodielectric Patchy Particles, ACS Nano 15 (3) (2021) 5439–5448.
[18] D. Guo, C. Li, Y. Wang, Y.N. Li, Y.L. Song, Precise Assembly of Particles for Zigzag or Linear Patterns, Angew. Chem. Int. 56 (48) (2017) 15348–15352.
[19] T. Mitsui, Y. Wakayama, T. Onodera, Y. Takaya, H. Oikawa, Observation of light propagation across a 90 degrees corner in chains of microspheres on a patterned substrate, Opt. Lett. 33 (11) (2008) 1189–1191.
[20] Y.D. Yin, Y. Lu, B. Gates, Y.N. Xia, Template-assisted self-assembly: A practical route to complex aggregates of monodispersed colloids with well-defined sizes, shapes, and structures, JACS 123 (36) (2001) 8718–8729.
[21] K. Brassat, F. Assion, U. Hilleringmann, J.K.N. Lindner, Self-organization of nanospheres in trenches on silicon surfaces, Phys. Status Solidi A 210 (8) (2013) 1485–1489.
[22] O. Lecarme, T.P. Rivera, L. Arbez, T. Honegger, K. Berton, D. Peyrade, Colloidal optical waveguides with integrated local light sources built by capillary force assembly, J. Vacuum Sci. Tech. B 28 (6) (2010) C6011–C6015.
[23] Y. Hong, W. Ahn, S.V. Boriskina, X. Zhao, B.M. Reinhard, Directed Assembly of Optoplasmonic Hybrid Materials with Tunable Photonic-Plasmonic Properties, J. Phys. Chem. Lett. 6 (11) (2015) 2056–2064.
[24] S.R. Chen, M. Su, C. Zhang, M. Gao, B. Bao, Q. Yang, B. Su, Y.L. Song, Fabrication of Nanoscale Circuits on Inkjet-Printing Patterned Substrates, Adv. Mater. 27 (26) (2015) 3928–3933.
[25] S. Vyawahare, K.M. Craig, A. Scherer, Patterning lines by capillary flows, Nano Lett. 6 (2) (2006) 271–276.
[26] K.Y. Suh, Surface-tension-driven patterning: Combining tailored physical self-organization with microfabrication methods, Small 2 (7) (2006) 832–834.
[27] T. Mitsui, Y. Wakayama, T. Onodera, Y. Takaya, H. Oikawa, Light propagation within colloidal crystal wire fabricated by a dewetting process, Nano Lett. 8 (3) (2008) 853–858.
[28] A.R. Tao, J. Huang, P. Yang, Langmuir–Blodgettry of Nanocrystals and Nanowires, Acc. Chem. Res. 41 (12) (2008) 1662–1673.
[29] R.R. Collino, T.R. Ray, R.C. Fleming, C.H. Sasaki, H. Haj-Hariri, M.R. Begley, Acoustic field controlled patterning and assembly of anisotropic particles, Extreme Mech. Lett. 5 (2015) 37–46.
[30] X.Y. Ling, I.Y. Phang, H. Schönherr, D.N. Reinhoudt, G.J. Vancso, J. Huskens, Freestanding 3D supramolecular particle bridges: fabrication and mechanical behavior, Small 5 (12) (2009) 1428–1435.
[31] T. Kraus, L. Malaquin, E. Delamarche, H. Schmid, N.D. Spencer, H. Wolf, Closing the gap between self-assembly and microsystems using self-assembly, transfer, and integration of particles, Adv. Mater. 17 (20) (2005) 2438–2442.
[32] C. Ladd, J.H. So, J. Muth, M.D. Dickey, 3D Printing of Free Standing Liquid Metal Microstructures, Adv. Mater. 25 (36) (2013) 5081–5085.
[33] F. Garcia-Santamaria, H.T. Miyazaki, A. Urquia, M. Ibisate, M. Belmonte, N. Shinya, F. Meseguer, C. Lopez, Nanorobotic manipulation of microspheres for on-chip diamond architectures, Adv. Matter. 14 (16) (2002) 1144–1147.
[34] S. Zimmermann, T. Tiemerding, S. Fatikow, Automated Robotic Manipulation of Individual Colloidal Particles Using Vision-Based Control, IEEE ASME Trans. Mechatron. 20 (5) (2015) 2031–2038.
[35] S. Yang, V.N. Astratov, Spectroscopy of coherently coupled whispering-gallery modes in size-matched bispheres assembled on a substrate, Opt. Lett. 34 (13) (2009) 2057–2059.
[36] V.N. Astratov, J.P. Franchak, S.P. Ashili, Optical coupling and transport phenomena in chains of spherical dielectric microresonators with size disorder, Appl. Phys. Lett. 85 (23) (2004) 5508–5510.
[37] N. Kang, J. Zhu, et al., Reconfiguring Self-Assembly of Photoresponsive Hybrid Colloids, J. Am. Chem. Soc. 144 (11) (2022) 4754–4758.
[38] Z. Rozynek, M. Han, F. Dutka, P. Garstecki, A. Józefczak, E. Luijten, Formation of printable granular and colloidal chains through capillary effects and dielectrophoresis, Nat. Commun. 8 (2017) 15255.
[39] W.H. Yeo, J.H. Chung, Y.L. Liu, K.H. Lee, Direct concentration of circulating DNA by using a nanostructured tip, in: M. Razeghi, H. Mohseni (Eds.), Biosensing, 7035, SPIE, 2008, p. 70350N.
[40] J. Tang, B. Gao, H.Z. Geng, O.D. Velev, L.C. Qin, O. Zhou, Assembly of 1D nanostructures into sub-micrometer diameter fibrils with controlled and variable length by dielectrophoresis, Adv. Mater. 15 (16) (2003) 1352–1355.
[41] J. Ma, J. Tang, Q. Cheng, H. Zhang, N. Shinya, L.C. Qin, Effects of surfactants on spinning carbon nanotube fibers by an electrophoretic method, Sci. Technol. Adv. Mater. 11 (6) (2010) 1–7.
[42] J.H. Han, G.L.C. Paulus, R. Maruyama, D.A. Heller, W.J. Kim, P.W. Barone, C.Y. Lee, J.H. Choi, M.H. Ham, C. Song, C. Fantini, M.S. Strano, Exciton antennas and concentrators from core–shell and corrugated carbon nanotube filaments of homogeneous composition, Nat. Mater. 9 (10) (2010) 833–839.
[43] R. Maruyama, Y.W. Nam, J.H. Han, M.S. Strano, Well-defined single-walled carbon nanotube fibers as quantum wires: Ballistic conduction over micrometer-length scales, Curr. Appl. Phys. 11 (6) (2011) 1414–1418.
[44] J.H. Shin, K. Kim, T. An, W. Choi, G. Lim, Reliable Diameter Control of Carbon Nanotube Nanobundles Using Withdrawal Velocity, Nanoscale Res. Lett. 11 (2016) 1–6.
[45] S.J. Kahng, J.H. Kim, J.H. Chung, Nanostructured Tip-Shaped Biosensors: Application of Six Sigma Approach for Enhanced Manufacturing, Sensors 17 (1) (2017) 1–17.
[46] W.H. Yeo, F.L. Chou, K. Oh, K.H. Lee, J.H. Chung, Hybrid Nanofibril Assembly Using an Alternating Current Electric Field and Capillary Action, J. Nanosci. Nanotechnol. 9 (12) (2009) 7288–7292.
[47] B. Yuan, L. Cademartiri, Flexible One-Dimensional Nanostructures: A Review, J. Mater. Sci. Technol. 31 (6) (2015) 607–615.
[48] J.L. Breidenich, M.C. Wei, G.V. Clatterbaugh, J.J. Benkoski, P.Y. Keng, J. Pyun, Controlling length and areal density of artificial cilia through the dipolar assembly of ferromagnetic nanoparticles, Soft Matter 8 (19) (2012) 5334–5341.
[49] L.J. Hill, J. Pyun, Colloidal Polymers via Dipolar Assembly of Magnetic Nanoparticle Monomers, ACS Appl. Mater. Interfaces 6 (9) (2014) 6022–6032.
[50] A. Mikkelsen, A. Kertmen, K. Khobaib, M. Rajňák, J. Kurimský, Z. Rozynek, Assembly of 1D Granular Structures from Sulfonated Polystyrene Microparticles, Materials 10 (10) (2017) 1212.
[51] F. Dutka, Z. Rozynek, M. Napiórkowski, Continuous and discontinuous transitions between two types of capillary bridges on a beaded chain pulled out from a liquid, Soft Matter 13 (27) (2017) 4698–4708.
[52] I. Sriram, R. Walder, D.K. Schwartz, Stokes-Einstein and desorption-mediated diffusion of protein molecules at the oil–water interface, Soft Matter 8 (22) (2012) 6000–6003.
[53] B. Bharti, A.L. Fameau, M. Rubinstein, O.D. Velev, Nanocapillarity-mediated magnetic assembly of nanoparticles into ultraflexible filaments and reconfigurable networks, Nat. Mater. 14 (11) (2015) 1104.
[54] D.C. Li, J. Rogers, S.L. Biswal, Probing the Stability of Magnetically Assembled DNA-Linked Colloidal Chains, Langmuir 25 (16) (2009) 8944–8950.
[55] V.T. Mukundan, M.N.T. Quang, Y.H. Miao, A.T. Phan, Connecting magnetic micro-particles with DNA G-quadruplexes, Soft Matter 9 (1) (2013) 216–223.
[56] A. Demortiere, A. Snezhko, M.V. Sapozhnikov, N. Becker, T. Proslier, I.S. Aranson, Self-assembled tunable networks of sticky colloidal particles, Nat. Commun. 5 (2014) 3117.
[57] M. Motornov, S.Z. Malynych, D.S. Pippalla, B. Zdyrko, H. Royter, Y. Roiter, M. Kahabka, A. Tokarev, I. Tokarev, E. Zhulina, K.G. Kornev, I. Luzinov, S. Minko, Field-Directed Self-Assembly with Locking Nanoparticles, Nano Letters 12 (7) (2012) 3814–3820.
[58] J. Byrom, P. Han, M. Savory, S.L. Biswal, Directing Assembly of DNA-Coated Colloids with Magnetic Fields To Generate Rigid, Semiflexible, and Flexible Chains, Langmuir 30 (30) (2014) 9045–9052.
[59] D. Guo, Y.N. Li, X. Zheng, F.Y. Li, S.R. Chen, M.Z. Li, Q. Yang, H.Z. Li, Y.L. Song, Programmed Coassembly of One-Dimensional Binary Superstructures by Liquid Soft Confinement, JACS 140 (1) (2018) 18–21.
[60] Z. Rozynek, V.N. Manoharan, et al. Efficient formation of one particle–thick microstructures on a substrate by direct writing (in preparation 2022).

Fabrication of 1D particle structures outside a liquid environment using electric and capillary interactions: From fundamentals to applications

Z. Rozynek,[1,2*] Y. Harkavyi[1] and K. Giżyński[3]

[1] *Faculty of Physics, Adam Mickiewicz University, Uniwersytetu Poznańskiego 2, 61-614 Poznań, Poland*
[2] *Department of Battery Technology, Institute for Energy Technology (IFE), Instituttveien 18, NO-2007 Kjeller, Norway*
[3] *Institute of Physical Chemistry, Polish Academy of Sciences, Kasprzaka 44/52, 01-224 Warsaw, Poland*

*Corresponding author: zbiroz@amu.edu.pl

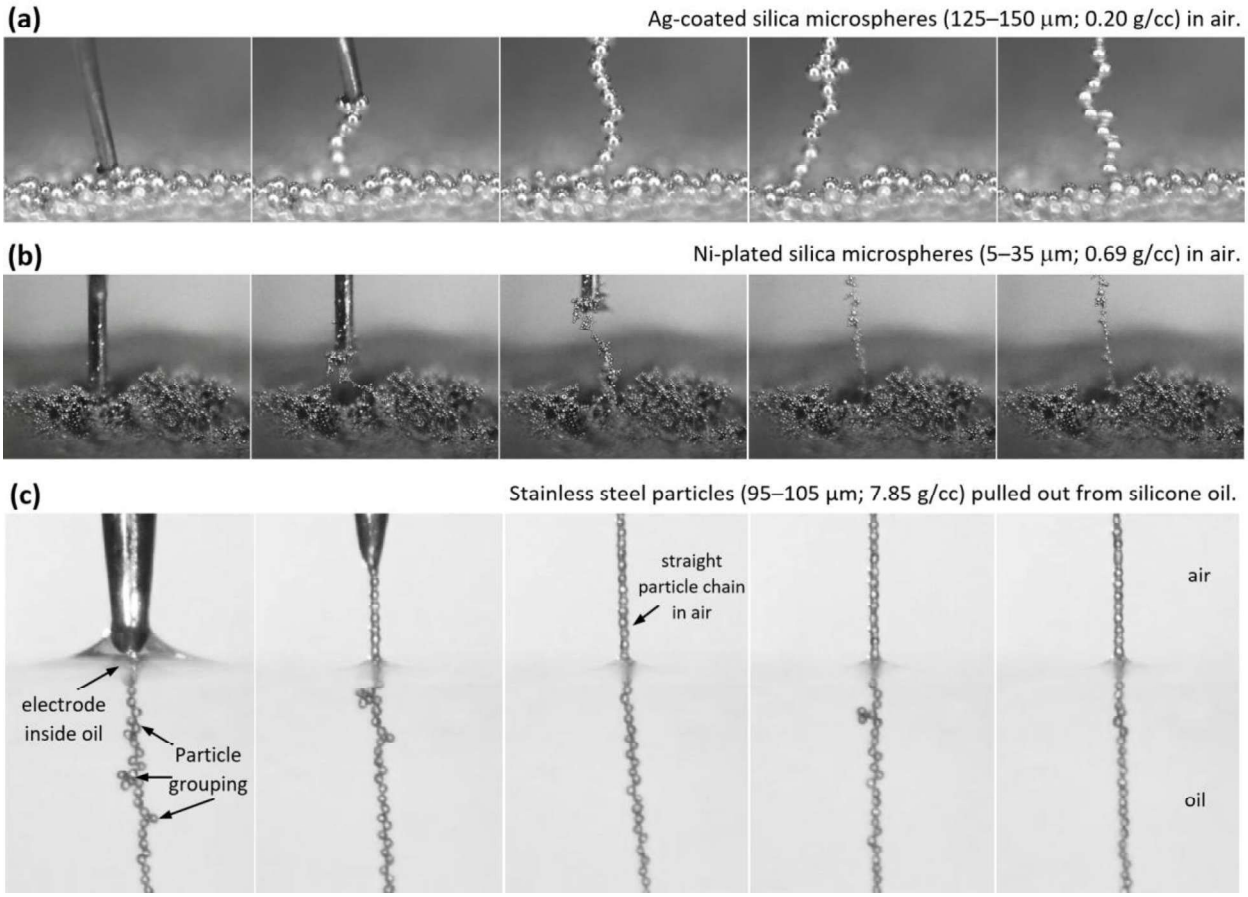

Figure S1. (**a**) Ag-coated and (**b**) Ni-coated hollow silica microspheres (sprinkled on a dry substrate) assemble irregularly and form agglomerates when the signal electrode is lifted up. (**c**) Similarly, stainless steel particles—sedimented on the bottom of a container filled up with silicone oil—form irregular structures and agglomerates when in the oil. However, when the particle assembly is transited through the air–oil interface, a straight single-particle-thick chain is formed in air due to the action of the surface tension as explained in section 3.2. See also corresponding **Movie S5** and **Movie S6**.

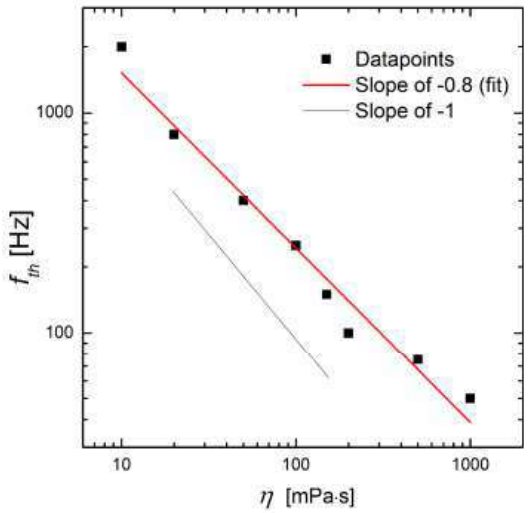

Figure S2. Cut-off frequency plotted against silicone oil viscosity. Data points taken from Figure 6.

Tetrabutylammonium chloride (TBACl) was dissolved in silicone oil and hence increased its ionic conductivity. **Figure S3** shows the consequences of the addition of mobile ions to the oil. Addition of the TBACl salt affects the $U_{\min}(f)$ curve by shifting it towards higher frequency values. If ions are added to the solution, the screening length is shortened. Thus, for the same ion mobility, one needs to change the polarity of the electric tension faster in order to prevent the ions to re-locate and sit at their screening positions.

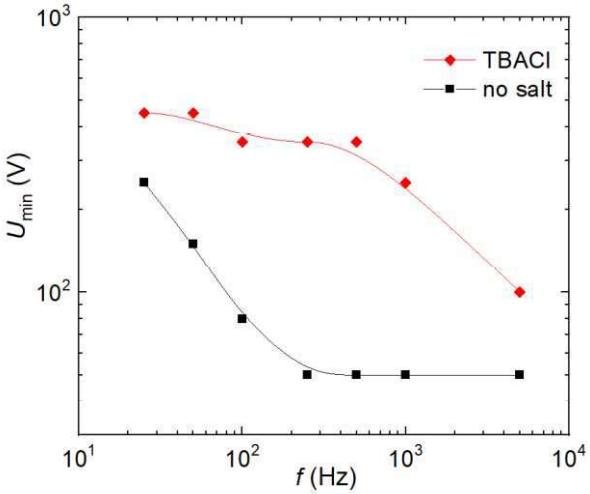

Figure S3. The addition of ions to the dispersion (TBACl salt dissolved in silicone oil) affects the $U_{\min}(f)$ curve by shifting it towards higher frequency values.

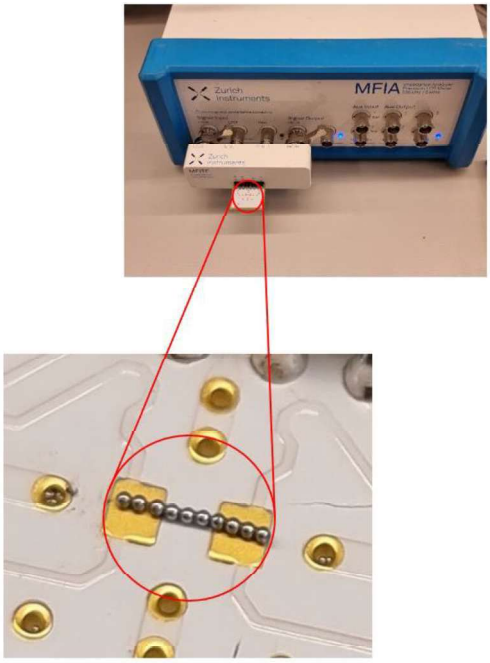

Figure S4. We used impedance spectrometer from Zurich Instruments (MFIA) to measure the real part of impedance. The particle chain was deposited on a 2T DUT (device-under-test) carrier with two copper pads (thickness of ~10 µm, and the gap between the pads ~16 mm) plugged into an MFITF Impedance Test Fixture, which ensured very accurate measurements of impedance, especially at low values close to the limit of the instrument (~0.1 mΩ). The experimental setup enabled in-situ monitoring of electrical impedance during particle chain compression.

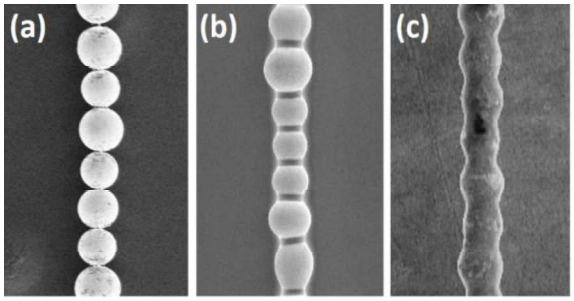

Figure S5. SEM images of (**a**) Ag-coated glass particles, (**b**) Stainless steel particles with castor oil particle bridges, and (**c**) Cu particles coated by liquid paraffin. The solidified paraffin caused the particles to be permanently locked.

Movie S1. Demonstration of transition between two types of capillary liquid bridges: As a particle is lifted up above air–liquid interface, a particle–planar liquid surface capillary bridge (Type I) extends and eventually undergoes a transition into the particle–particle liquid bridge (Type II). Meanwhile, a new particle–planar liquid surface capillary bridge is formed at the particle below. Simulation for particle size 50 mm.

Movie S2. Example of experimental realization of the electric route for fabricating 1D particle structures: Ag-coated hollow silica microspheres ($\rho \sim 0.17$ g·cm^{-3}, size ~60 μm) dispersed at the air–silicone oil interface. Electric voltage (U = 500 V, f = 10 kHz, square wave) is applied to the electrode. As the electrode is elevated (~ 0.1 mm·s^{-1}), particles—one after another—are successfully pulled out of the interface forming a structure resembling a beaded necklace by appearance.

Movie S3. Example of experimental realizations of the electric route for fabricating 1D particle structures: Stainless steel particles ($\rho \sim 7.8$ g·cm^{-3}, size ~100 μm) suspended in silicone oil. To form 1D particle structure electric voltage (U = 500 V, f = 10 kHz) is applied to the electrode. The particle chain is initially formed in a liquid phase. When the electrode is lifted up, the particle chain became longer, as the sedimented particles kept-on attracting to the chain's bottom end. Eventually, the structure transited through the air–liquid interface and continued growing forming a 1D particle structure outside bulk liquid.

Movie S4. Stability and flexibility of a beaded chain: Particle structure remains stable after turning of the electric potential. The 1D particle structure flutters and bends due to small wind drafts existing in our laboratory. A long particle chain is composed of 50-μm conductive particles held together by the action of liquid capillary bridges formed between neighboring particles.

Movie S5. Demonstration of particle agglomerate formation: Conductive microparticles (sprinkled on a dry substrate) assemble irregularly and form agglomerates when the electrode is lifted up. Ag-coated silica microparticles ($\rho \sim 0.2$ g·cm^{-3}, size of 125–150 μm) are used in the first part of the movie, and Ni-plated silica microparticles ($\rho \sim 0.69$ g·cm^{-3}, size of 5–35 μm) are used in the second part of the movie.

Movie S6. The role of Type I capillary liquid bridge in particle aligning: Stainless steel particles ($\rho \sim 7.8$ g·cm^{-3}, size ~100 μm) sedimented on the bottom of a container filled up with silicone oil. The particles form agglomerates in a liquid phase. These unwanted features are eliminated by the action of the surface tension force which promotes particle alignment in vertical direction. Eventually, a single-particle-thick microstructure is created outside the bulk liquid.

Movie S7. Buckling to bending transition of particle chain under mechanical compression observed at increased electric tension. A pointy piece of a non-conductive substrate (to which a bottom end of the chain was attached) moves up and down to change the mechanical compressive force acting on the chain. Stainless-steel particles with size around ~100 μm.

Movie S8. A chain made of stainless-steel particles (size ~200 μm) was spanned between a static electrode and an electrode that could rapidly translate in the vertical direction. A transverse wave propagating along the particle chain was created and the propagation velocity of the wave was recorded using a high-speed camera (3000 fps). The estimated velocity was around 35 cm/s.

——Scientific Paper II——

Single-particle-thick microstructures fabricated through controlled withdrawal of particles from a dispersion meniscus

Harkavyi Y., Tiwari G. And Rozynek Z.

Materials & Design, Volume 255, July 2025, 114160

Materials & Design 255 (2025) 114160

Contents lists available at ScienceDirect

Materials & Design

journal homepage: www.elsevier.com/locate/matdes

Single-particle-thick microstructures fabricated through controlled withdrawal of particles from a dispersion meniscus

Y. Harkavyi [a], G. Tiwari [b], Z. Rozynek [a,c,*]

[a] Faculty of Physics and Astronomy, Adam Mickiewicz University, Uniwersytetu Poznańskiego 2, 61-614 Poznań, Poland
[b] Institute of Physical Chemistry, Polish Academy of Sciences, Kasprzaka 44/52, 01-224 Warsaw, Poland
[c] CADENAS P.S.A., Prof. Sylwestra Kaliskiego 24, 85-796 Bydgoszcz, Poland

ARTICLE INFO

Keywords:
1D particle crystals
Single-particle-thick structures
Guided assembly
Fundamental research
Demonstration of application-driven insights

ABSTRACT

Beaded chains of conductive microparticles formed in air represent one of the most intriguing classes of particle-based microstructures. These 1D particle crystals offer high added value due to their unique physical properties. However, their fabrication remains challenging, and no scalable or industrially viable methods currently exist. This work presents a straightforward approach for forming such structures. The process utilizes a dispersion meniscus formed at the outlet of a conduit that also serves as an electrode. Microparticles are electrically extracted from the meniscus to form a single-particle-thick assembly with controllable length. The physical mechanisms governing structure formation are examined, and key sources of instability are identified to support process optimization. The effects of particle size, density, dispersing liquid viscosity, voltage magnitude, substrate geometry and conductivity, extraction direction, and pulling velocity are systematically investigated. The knowledge obtained through our basic research enables the reliable fabrication of freestanding particle structures and serves as a direct foundation for applied studies. To illustrate the practical potential of the method, several application-oriented demonstrations are presented. The impact of the work spans multiple fields, including materials science, soft matter physics, and microfabrication, and opens pathways for industrial applications in electronics, soft robotics, and additive manufacturing.

1. Introduction

Particle chains—structures with a thickness of a single particle—are among the most intriguing and valuable material configurations. Sometimes referred to as beaded assemblies, these structures possess distinctive characteristics that make it highly attractive for functional materials. If the chains are formed from uniformly sized microparticles, they exhibit properties such as periodicity on the mesoscale, which leads to effects like enhanced light scattering, distinct optical diffraction patterns, and photonic band gaps, which for chains made of microparticles are most evident in the infrared or terahertz range [1–3]. In addition, such chains are effective in applications requiring precise resonance control, such as antennas, emitters, or electromagnetic wave receivers [4,5]. In these cases, periodicity enables well-defined resonance conditions, improving the efficiency and selectivity of the system.

Particle chains also offer valuable features such as enhanced chemical interactions, improved catalytic performance, and better adsorption capabilities, particularly due to their increased surface area compared to, for example, cylindrical wires. They may also show non-linear conductivity affected by electro-thermal effects or by external electric fields [6–8]. Moreover, beaded structures demonstrate additional valuable features, including localized electric field enhancement, improved mechanical flexibility, and controlled phonon propagation [9–11]. Beyond functional applications, particle chains also hold promise for fundamental research. Short chains can serve as synthetic flagella or model systems for studying collective dynamics, microscale interactions, or bioinspired motion [12,13].

In **Fig. S1**, we present a materials landscape diagram (adapted from [14]) that categorizes materials into distinct groups, such as 3D and 2D disordered assemblies, as well as 3D, 2D, and 1D particle crystals. The diagram organizes these configurations in a simplified manner, with the x-axis representing the increasing cost of material fabrication and the y-axis indicating the expected value added by the materials after assembly. 1D particle crystals are positioned in the upper-right corner of the diagram, indicating that although their fabrication cost is relatively high — often exceeding the costs of 2D and 3D materials — their functional

* Corresponding author at: Faculty of Physics and Astronomy, Adam Mickiewicz University, Uniwersytetu Poznańskiego 2, 61-614 Poznań, Poland.
E-mail address: zbiroz@amu.edu.pl (Z. Rozynek).

https://doi.org/10.1016/j.matdes.2025.114160
Received 8 April 2025; Received in revised form 24 May 2025; Accepted 26 May 2025
Available online 27 May 2025

potential is exceptional. By improving the fabrication process and reducing associated costs, the impact potential of particle chains in scientific and industrial applications can be significantly expanded.

Through the work presented in this paper, we hope to contribute to the reduction of costs associated with the fabrication of particle chains by proposing a straightforward method for forming such structures. This study builds upon our previous work published in [15–20], where we described the formation of 1D particle crystals using a method that involved immersing a needle-shaped electrode into a dispersion of microparticles to initiate chain formation. As the electrode (held under voltage) was gradually lifted, single-particle-thick structures were formed aided by the capillary interactions. While effective, this method proved impractical for broader applications due to its limited scalability — much like writing with a quill pen that requires frequent dipping in ink, whereas a ballpoint pen offers greater efficiency. Inspired by this analogy, we hypothesized that modifying the system setup could provide a more practical and scalable alternative, akin to the continuous ink flow of a ballpoint pen. Instead of pulling a chain using a needle immersed in the dispersion, we generate a meniscus at the outlet of a conduit that serves as an electrode, forming the chain between the meniscus and a chosen substrate. This design ensures a continuous supply of microparticles to the meniscus, enabling more efficient chain formation — a process resembling 2D or 3D printing, where a reservoir and nozzle ensure a steady material flow, and a printhead or table can move to precisely control the chain's position relative to the substrate.

Although this method may seem like an inverted version of the previous setup, the physical mechanisms and instabilities governing chain formation are distinctly different. Consequently, we investigated these new effects in greater detail. In this work, we examine the physical principles underlying chain formation, identify key parameters influencing chain stability, and demonstrate potential applications.

The literature on the formation of 1D particle crystals (ordered chains) and disordered chains (characterized by irregular particle sizes and, consequently, non-uniform interparticle distances) from microparticles outside of bulk liquid remains relatively scarce. Most studies focus on the formation of such structures in liquids, often utilizing electric fields [21–23], magnetic fields [24–27], or acoustic fields [28,29]. Regarding the formation of 1D particle crystals in air, only a few examples are reported in the literature. These typically describe the formation of free-standing, short structures or structures that are not single-particle-thick along their entire length [30–39].

In this work, we employ the synergistic action of an electric voltage, which induces cohesion between particles, and capillary interactions, which promote the formation of single-particle-thick structures. The concept of simultaneously using electric fields and surface tension is not new. This method has previously been applied to guide and concentrate molecules, nanoparticles, or microparticles onto electrode tips, resulting in fibril-like structures for various applications [30–37]. Our approach, while also involving electrical phenomena and capillary interactions, is conceptually different from the methods described in the literature. Unlike previous studies, where particles were dielectrophoretically assembled at the tip of an electrode (typically in the form of agglomerates) and gradually formed fibril-like structures, our method relies on controlled particle delivery to a meniscus formed at the outlet of a conductive conduit. In this process, the meniscus acts as a dynamic forming medium, enabling continuous chain formation in air between the meniscus and any substrate of any shape (*e.g.*, a flat plate or a narrow cylinder-like). This approach simplifies the chain formation that is truly a single-particle-thick structure and, in addition, improves scalability, allowing the production of microstructures with potentially broader practical applications.

The manuscript opens with studies aimed at optimizing meniscus preparation conditions. We began by examining how the preparation conditions of the particle dispersion at the conduit outlet influenced the repeatability of the extraction process. In particular, we tested different liquid content levels and meniscus shapes. These initial investigations were followed by numerical simulations of electrostatic interactions between a charged spherical particle and a flat dielectric surface, aimed at understanding the conditions present during the early stage of chain formation, when contact is established between the meniscus and the substrate. Additionally, we carried out experiments under controlled humidity to assess the influence of ambient moisture levels on chain formation feasibility.

Following this, we identify and analyse the parameters affecting the stability of the formed structures and describe the physical mechanisms governing this process. We investigate the influence of particle size, applied voltage, and substrate conditions on the stability and maximum achievable chain length. Next, we examine the influence of gravity and system configuration (downward vs. upward extraction) as well as the electrical properties of the substrate on microstructure formation. In the following section, we investigate the effect of pulling velocity, voltage, and liquid viscosity.

Knowledge gained from these studies has been useful in demonstrating applications of the method and the utilization of 1D particle crystals, which we present in the final section of the manuscript. These applications include continuous formation of complex three-dimensional structures around curved surfaces, creation of suspended interconnects that bridge conductive elements on separate substrates, development of mechanically resilient microstructures that can withstand hundreds of axial deformation cycles without failure, and voltage-controlled retraction and extension of suspended particle chains.

2. Methods

2.1. System configurations and experimental setup

The experimental setup in this study consisted of several precision components designed to ensure accurate control and monitoring throughout the experiment. A syringe pump (neMESYS Low Pressure module V2, CETONI GmbH) enabled the controlled delivery of the particle dispersion through a 1 mm polymeric microfluidic tube, providing precise and reproducible dosing into the dispersion conduit. This conduit, which served as an electrode in most experimental conditions, was mounted on a motorized stage (linear guide module L2/300 mm with a stepper motor LDO-57STH56) that allowed vertical translation (along the Z axis) and was secured within an electrically insulating holder to ensure both stability and insulation. To achieve precise positioning of the substrate in the XY directions and accurate alignment relative to the dispersion conduit, a manual stage (Thorlabs, LT3) was employed.

A signal generator (SDG1025, Siglent) produced a low-voltage input (0–10 V peak-to-peak, square wave), which was fed into a high-voltage bipolar amplifier (10HVA24-BP1, HVP). This amplifier increased the input signal by a factor of 500. The amplified output signal could be directed to either the conductive substrate or the conductive conduit, depending on the experimental configuration. In the setup shown in Fig. 1, the dispersion conduit serves as the electrode. The voltage U used to describe the results is reported as root mean square (RMS) values. For a square wave input, the RMS voltage corresponds to half of the peak-to-peak voltage.

For optical monitoring and capturing critical moments of particle assembly and chain formation, digital microscopes (AM7115, Dino-Lite) were used to provide real-time front and side views of the experimental area. A desktop computer collected and stored videos from the digital microscopes. For clarity, Fig. 1 does not depict these microscopes, the computer, or the signal generator. In some experiments designed to test the role of gravity, the system was inverted by 180°, positioning the substrate above the conduit, with the meniscus oriented toward the substrate.